ADVANCED STEEL CONSTRUCTION

An International Journal

Volume 4 Number 3

September 2008

CONTENTS

Editors-in-Chief

S.L. Chan, *The Hong Kong Polytechnic University, Hong Kong*

W.F. Chen, *University of Hawaii at Manoa, USA*

R. Zandonini, *Trento University, Italy*

Cover: International Commercial Centre in West Kowloon, Hong Kong, China. Courtesy of Sun Hung Kai Properties Limited.

General Information
Advanced Steel Construction, an international journal

Aims and scope

The International Journal of Advanced Steel Construction provides a platform for the publication and rapid dissemination of original and up-to-date research and technological developments in steel construction, design and analysis. Scope of research papers published in this journal includes but is not limited to theoretical and experimental research on elements, assemblages, systems, material, design philosophy and codification, standards, fabrication, projects of innovative nature and computer techniques. The journal is specifically tailored to channel the exchange of technological know-how between researchers and practitioners. Contributions from all aspects related to the recent developments of advanced steel construction are welcome.

Instructions to authors

Submission of the manuscript. Authors may submit three double-spaced hard copies of manuscripts together with an electronic copy on a diskette or cd-rom in an editable format (MS Word is preferred). Manuscripts should be submitted to the regional editors as follows for arrangement of review.

Asian Pacific , African and organizing editor :	Professor S.L. Chan
American editor :	Professor W.F. Chen
European editor :	Professor R. Zandonini

All manuscripts submitted to the journal are highly recommended to accompany with a list of four potential reviewers suggested by the author(s). This list should include the complete name, address, telephone and fax numbers, email address, and at least five keywords that identify the expertise of each reviewer. This scheme will improve the process of review.

Style of manuscript

General. Author(s) should provide full postal and email addresses and fax number for correspondence. The manuscript including abstract, keywords, references, figures and tables should be in English with pages numbered and typed with double line spacing on single side of A4 or letter-sized paper. The front page of the article should contain:

a) a short title (reflecting the content of the paper);
b) all the name(s) and postal and email addresses of author(s) specifying the author to whom correspondence and proofs should be sent;
c) an abstract of 100-200 words; and
d) 5 to 8 keywords.

The paper must contain an introduction and a conclusion. The length of paper should not exceed 25 journal pages (approximately 15,000 words equivalents).

Tables and figures. Tables and figures including photographs should be typed, numbered consecutively in Arabic numerals and with short titles. They should be referred in the text as Figure 1, Table 2, etc. Originally drawn figures and photographs should be provided in a form suitable for photographic reproduction and reduction in the journal.

Mathematical expressions and units. The Systeme Internationale (SI) should be followed whenever possible. The numbers identifying the displayed mathematical expression should be referred to in the text as Eq. (1), Eq. (2).

References. References to published literature should be referred in the text, in the order of citation with Arabic numerals, by the last name(s) of the author(s) (e.g. Zandonini and Zanon [3]) or if more than three authors (e.g. Zandonini et al. [4]). References should be in English with occasional allowance of 1-2 exceptional references in local languages and reflect the current state-of-technology. Journal titles should be abbreviated in the style of the Word List of Scientific Periodicals. References should be cited in the following style [1, 2, 3].

Journal: [1] Chen, W.F. and Kishi, N., "Semi-rigid Steel Beam-to-column Connections, Data Base and Modelling", Journal of Structural Engineering, ASCE, 1989, Vol. 115, No. 1, pp. 105-119.

Book: [2] Chan, S.L. and Chui, P.P.T., "Non-linear Static and Cyclic Analysis of Semi-rigid Steel Frames", Elsevier Science, 2000.

Proceedings: [3] Zandonini, R. and Zanon, P., "Experimental Analysis of Steel Beams with Semi-rigid Joints", Proceedings of International Conference on Advances in Steel Structures, Hong Kong, 1996, Vol. 1, pp. 356-364.

Proofs. Proof will be sent to the corresponding author to correct any typesetting errors. Alternations to the original manuscript at this stage will not be accepted. Proofs should be returned within 48 hours of receipt by Express Mail, Fax or Email.

Copyright. Submission of an article to "Advanced Steel Construction" implies that it presents the original and unpublished work, and not under consideration for publication nor published elsewhere. On acceptance of a manuscript submitted, the copyright thereof is transferred to the publisher by the Transfer of Copyright Agreement and upon the acceptance of publication for the papers, the corresponding author must sign the form for Transfer of Copyright.

Permission. Quoting from this journal is granted provided that the customary acknowledgement is given to the source.

Page charge and Reprints. There will be no page charges if the length of paper is within the limit of 25 journal pages. A total of 30 free offprints will be supplied free of charge to the corresponding author. Purchasing orders for additional offprints can be made on order forms which will be sent to the authors. These instructions can be obtained at the Hong Kong Institute of Steel Construction, Journal website: http://www.hkisc.org

The International Journal of Advanced Steel Construction is published quarterly by non-profit making learnt society, The Hong Kong Institute of Steel Construction, c/o Department of Civil & Structural Engineering, The Hong Kong Polytechnic University, Hung Hom, Kowloon, Hong Kong.

VOLUME 4   NUMBER 3   SEPTEMBER 2008

Technical Papers

Conference Announcements

ANALYSIS AND DESIGN OF STEEL BRIDGE STRUCTURES WITH ENERGY ABSORPTION MEMBERS

Zhiyi Chen[1], Hanbin Ge[2,*], and Tsutomu Usami[3]

[1]Lecturer, Department of Geotechnical Engineering, Tongji University, Shanghai 200092, China
[2]Professor, Department of Civil Engineering, Meijo University, 1-501,
Shiogamaguchi Tenpaku-ku, Nagoya, 468-8502, Japan
[3]Professor, Department of Civil Engineering, Meijo University, 1-501,
Shiogamaguchi Tenpaku-ku, Nagoya, 468-8502, Japan
*(Corresponding author: E-mail: gehanbin@ccmfs.meijo-u.ac.jp)

ABSTRACT: This paper aims to investigate the efficiency of energy absorption members incorporated in thin-walled steel bridge structures against major earthquakes. Energy absorption members concerned here is buckling-restrained brace (BRB), which dissipates earthquake-induced energy through metallic yielding through axial tension and compression. Dynamic nonlinear time-history analysis has been performed. It is found that such an energy absorption member is effective in mitigating earthquake hazard.

Keywords: Energy absorption member; steel bridge structures; seismic design; time-history analysis

1. INTRODUCTION

In recent years, various energy absorption members have been developed and used successfully into building structures to suppress structural vibrations induced by earthquakes. Of these, the hysteretic damper, whose mechanism is through material yielding to absorb earthquake-induced energy as well as increase effective damping, is the most popular one to be employed due to its reliability and low cost. Although extensive experimental and analytical researches have been conducted on building structures with such hysteretic dampers, the researches on bridge structures remain infancy [1, 2]. Furthermore, efficiency of hysteretic dampers on seismic response reduction has been validated in comparison with the moment resisting steel structures [3] or structures with conventional steel braces [4], however, few works have addressed the efficiency between various hysteretic dampers especially when they are incorporated in bridge structures.

Three bridge forms are employed as illustrative examples. They are simple structural forms of single-deck and multi-deck bridge piers and, additionally, one complicated structural form of an arch bridge. Figure 1 shows an example of single-deck bridge piers installed with a type of hysteretic dampers, i.e., buckling-restrained brace (BRB). In the paper, the fundamental principles of structures with BRB members are introduced first. Followed is the description of design and modeling method for the BRB member. Emphases are put on the comparison of BRB efficiency in aforementioned bridge structures through times-history analyses. This investigation may provide useful messages for design of hysteretic dampers and their further laboratory experimental research.
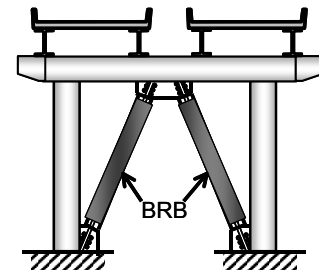
Figure 1. Single-deck Bridge Pier with Hysteretic Damping Device

2.   FUNDAMENTAL PRINCIPLES

Sketches of physical models for the damped structure installed with BRB are shown in Figure 2. As is seen from Figure 2, it is assumed that the BRB member itself is an entire damping device. Consequently, basic properties of the damping device have the same meaning with those of the BRB member (i.e., $F_{y,d}=F_{y,BRB}$, $K_d=K_{BRB}$). The BRB member is then connected as a whole with the main structure in the parallel manner. It is clear that the yield displacement of the BRB member must be smaller than that of the main structure to ensure the BRB member yields prior to the main structure during an earthquake. Namely, the design conditions of $\delta_{y,d} < \delta_{y,f}$ and $\delta_{y,d} = \delta_{y,fd}$ must be satisfied.

To compare seismic demands quantitatively, the ratio of the damper's yield strength to the main structure's lateral yield resistance, referred to as the strength ratio α_F, and the ratio of the damper's initial stiffness to the main structure's lateral stiffness, referred to as the stiffness ratio α_K, are generally used as design criteria [5, 6, 7].
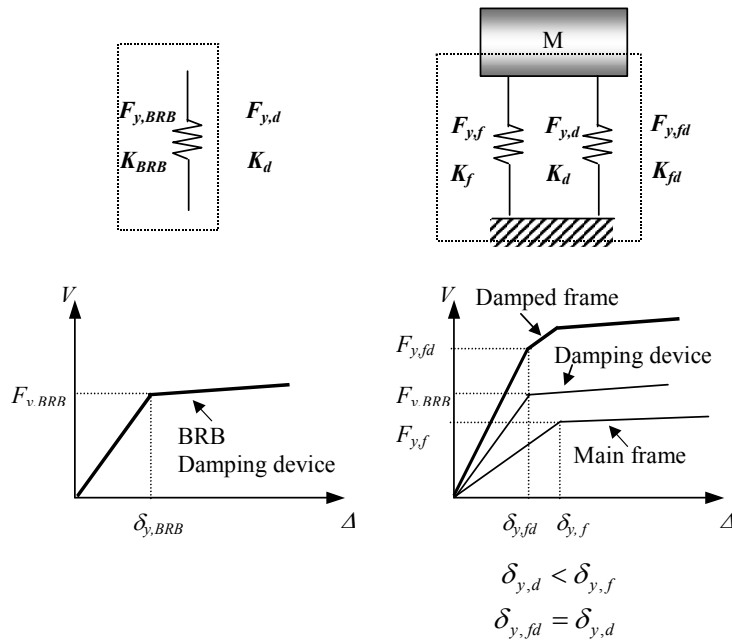
(a) BRB Damping Device   (b) Damped Frame
Figure 2. Idealized SDOF System Installed with BRB

3.   DESIGN AND MODELING OF DAMPING DEVICES

3.1   Basic Properties of Buckling-restrained Braces

To date, many types of BRB sections are used. The BRB used in this study is one with a flat core plate developed by Nagoya University [8, 9], whose cross section is shown in Figure 3. Similar to the other BRBs, axial deformation of this BRB is allowed only at the core plate, whose severe buckling is eliminated by the exterior restraining members. The axial yield strength of the BRB, $P_{y,BRB}$, is given by

$$P_{y,BRB} = \sigma_{y,BRB} \times A_{BRB} \tag{1}$$

where $\sigma_{y,BRB}$ = tensile yield stress of steel material and A_{BRB} = section area of the core plate.

The geometric parameters and basic properties of the BRB are illustrated in Figure 4. Relationship between these parameters can be expressed as follows,

$$F_{y,BRB} = K_{BRB} \cdot \delta_{y,BRB}, \quad \delta_{y,BRB} = \sigma_{y,BRB} \cdot \frac{2l_{BRB}^2}{EL}, \quad K_{BRB} = A_{BRB} \cdot \frac{EL^2}{2l_{BRB}^3} \tag{2}$$

where $F_{y,BRB}$, $\delta_{y,BRB}$, and K_{BRB} = the lateral yield strength, displacement, and elastic stiffness of a pair of BRBs, respectively; l_{BRB} = length of a BRB; L = the structure span.
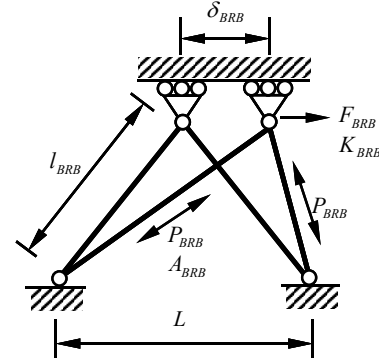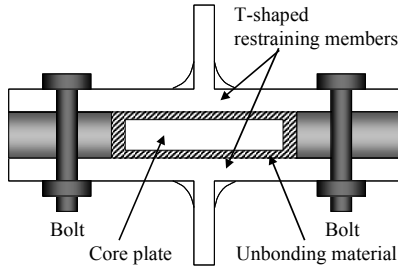
Figure 3. Buckling-restrained Brace (BRB)   Figure 4. Schematic Diagram for BRB Deformation

3.2   Hysteretic Model and FE Modeling of BRB

Figure 5 shows a finite element model of the single-deck bridge pier with BRB, referred to as BRB model later. BRB is directly modeled by the truss element, only carrying axial tension and compression without local bucking. In this study, the core plates of the BRB employed are made of SS400 steel. For such a BRB member, a bilinear stress-strain relationship with kinematic hardening rule, as shown in Figure 6, is suggested [8, 9].
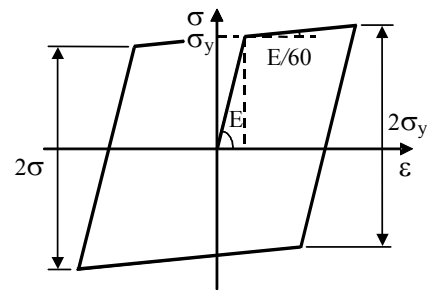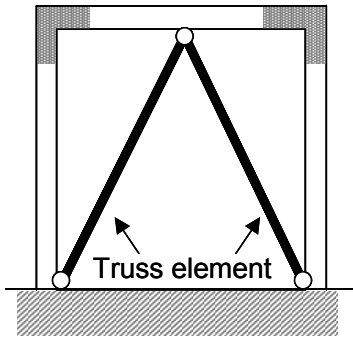
Figure 5. BRB Model   Figure 6. Hysteretic Model with Kinematic Hardening Rule

3.3   Design Order and Commentary for BRB in Seismic Design Process

Knowing the predefined strength ratio α_F and the stiffness ratio α_K as well as corresponding strength and stiffness of the main structure, $F_{y,BRB}$ and K_{BRB} can easily be determined. Then, the basic properties of BRB such as $\sigma_{y,BRB}$ and A_{BRB} can be easily established from Eq. 2. Note that such design process will cause variation of $\sigma_{y,BRB}$. In practical design, steel material is usually determined at the beginning, followed by the establishment of $\delta_{y,BRB}$. In other words, A_{BRB} becomes the single adjustable parameter in design of BRB damping devices.

4.   DESIGN AND ANALYTICAL MODELING OF STEEL BRIDGE STRUCTURES

4.1   Design and Analytical Modeling of Single-deck Bridge Piers
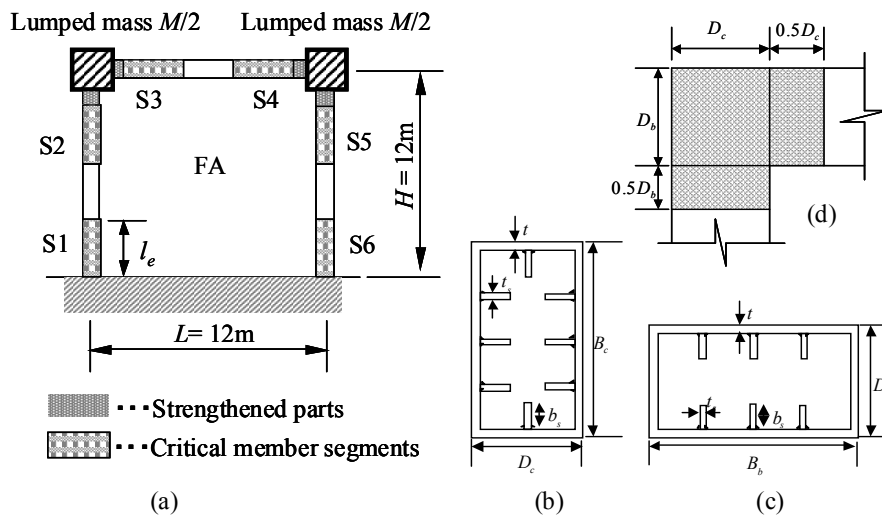
Figure 7. Single-deck Bridge Pier: (a) Layout; (b) Pier Section;
(c) Girder Section; and (d) Details at Strengthened Corner

The analytical model to be investigated is single-deck steel bridge piers of portal frame type, which are widely used in Japan to support elevated expressways. The general layout and finite element model are illustrated in Figure 7(a). The piers and girders have uniform stiffened box cross-sections, as shown in Figures 7(b) and (c). Since this type of portal frames is commonly heavy burdened, the plates at the pier-girder connection parts should be strengthened by doubling the plate thickness in order to avoid shear failure. The detailed size of strengthened parts is shown in Figure 7(d). The portal frame is designed in accordance with the Seismic Coefficient Method [10, 11], assuming regional class A and ground class II. Detailed information about the frame is summarized in the column titled by F1 in Table 1. In Table 1, the basic properties of the main frame (such as the initial yield displacement and strength, the ultimate displacement and strength) are determined with a pushover analysis as presented in a previous study [12], being somewhat analogous to those provided by Eurocode 8 [13], FEMA 356 [14], and Chopra and Goel [15].

Two-dimensional Timoshenko beam element of type B21 provided in the *ABAQUS* element library [16] is used to model the piers and girder, accounting for shear deformation. Each pier and girder of the main frame is divided into 20 elements: 5 elements for each critical member segment, 2 elements for strengthened parts, and the remains for the other parts. Here, critical member segments are denoted by the dotted sections at the pier bases and adjacent to the rigid corners, as shown in Figure 7(a).

4.2   Design and Analytical Modeling of Multi-deck Bridge Piers

Since a highway bridge system is commonly composed of thin-walled members and a popular format is low-rise (1~3 decks) framing type, double-deck and tri-deck bridge piers of portal frame types are considered here, as shown in Figure 8. It is assumed that the double-deck and tri-deck portal frames considered here have girders and piers of the same section as the preceding single-deck portal frame. Thus, each deck has the same yield inter-deck force and stiffness. The basic properties of multi-deck portal frames, denoted by F2 and F3, are listed in Table 1. The masses subjected on the top of columns are the same in each level.
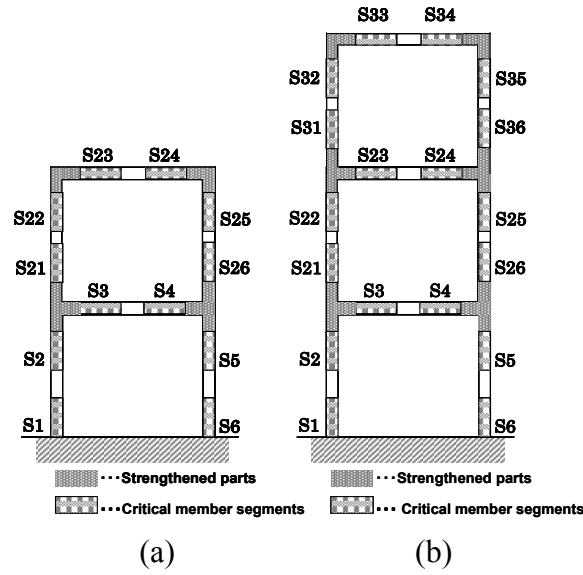
Figure 8. Multi-deck Steel Bridge Piers: (a) Double-deck; (b) Tri-deck

Table 1. Structural Parameters and Basic Properties of the Main Frames

Main Frame

Items	F1	F2	F3
Steel grade	SM490	SM490	SM490
Height, H (m)	12	12×2	12×3
Length, L (m)	12	12	12
Total deck mass, M (ton)	2042	2034	2895
Initial yield displacement, $\delta^{in}_{y,f}$ (m)	0.078	0.137	0.178
Initial yield strength, $V^{in}_{y,f}$ (kN)	6758	5939	5129
Ultimate displacement, $\delta_{u,f}$ (m)	0.418	0.518	0.549
Ultimate strength, $V_{u,f}$ (kN)	11836	10884	9557
Period, T_f (sec)	0.97	1.23	1.77

Pier		Girder	
Items	Value	Items	Value
Width, B_c (mm)	2000	Width, B_b (mm)	2000
Depth, D_c (mm)	1000	Depth, D_b (mm)	1000
Thickness, t (mm)	32	Thickness, t (mm)	32
Flange slenderness, R_{fc}	0.34	Flange slenderness, R_{fb}	0.34
Web slenderness, R_{wc}	0.34	Web slenderness, R_{wc}	0.78
Aspect ratio of flange, α_{fc}	1.0	Aspect ratio of flange, α_{fb}	0.5
Aspect ratio of web, α_{wc}	0.5	Aspect ratio of web, α_{wb}	0.83
No. of flange sub-panels, n_{fc}	2	No. of flange sub-panels, n_{fb}	4
No. of web sub-panels, n_{wc}	4	No. of web sub-panels, n_{wb}	1
Stiffener slenderness, $\bar{\lambda}_{sc}$	0.89	Stiffener slenderness, $\bar{\lambda}_{sb}$	0.72
Stiffener width, b_s (mm)	140	Stiffener width, b_s (mm)	140
Stiffener thickness, t_s (mm)	32	Stiffener thickness, t_s (mm)	32

4.3   Design and FE Modeling of Arch Bridge

An upper-deck arch bridge mainly composed of reinforced concrete (RC) deck slab, steel girders and single span steel arch ribs is modeled. A total length of the bridge is 173.0 m, and a two end-hinged steel arch has a span of 114.0 m with a rise at the crown of 16.87 m, giving a rise-span ratio of 1/6.76. Figure 9 shows the established FE model, where 3D Timoshenko beam elements of type B31 provided in the *ABAQUS* program [16] are employed to model the deck slab, girders, columns (vertical members), arch ribs and transverse bracings while 3D truss elements of type T3D2 for diagonals. In this analytical model, there are totally 884 elements with 462 nodes. More information of this bridge is referred to the literatures [2, 17].

4.4   Input Earthquakes

Three strong ground motions are adopted in the time-history analyses. They are ground motions recorded from the 1995 Hyogoken-Nanbu Earthquake at JR West Japan Takatori and at Fukiai supply station of Osaka Gas Corporation. Their accelerograms are shown in Figure 10, with the peak accelerations of 6.73m/sec^2 (JRT-EW-M), 6.87m/sec^2 (JRT-NS-M), and 7.36 m/sec^2 (FUKIAI-M), respectively.
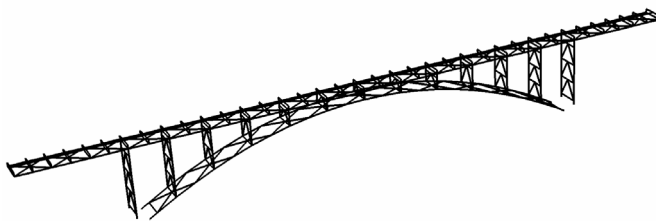
Figure 9. FE Model of Arch Bridge
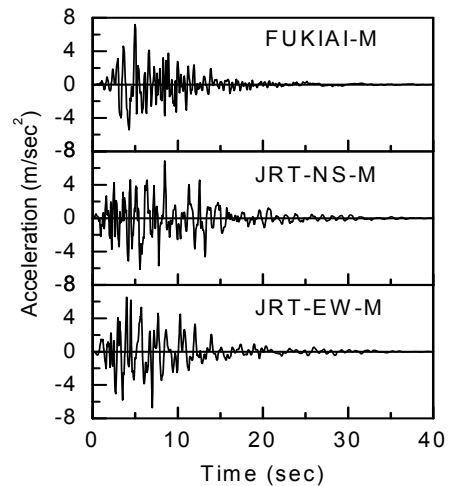
Figure 10. Input Earthquakes

5.   EFFICIENCY OF DAMPERS INSTALLED IN BRIDGE STRUCTURES

Dynamic time-history analyses are performed using the general-purpose finite element program ABAQUS [16]. In order to trace the material cyclic behavior accurately, the modified two-surface model [18] is employed. Rayleigh damping, which is usually utilized in dynamic analysis, consists of mass proportional damping and stiffness proportional damping. Here, mass proportional damping of 5 percent is used whereas inherent stiffness proportional damping is set as zero since it is neglectable if compared to the significant equivalent viscous damping due to yielding of hysteretic dampers.

5.1   Efficiency of Dampers Installed in Single-deck Bridge Piers

In this section, the efficiency of dampers installed in single-deck bridge piers is investigated according to the strength ratio, α_F and various strong ground motions.

The time-history analysis results for single-deck bridge piers subjected to JRT-EW-M accelerogram are illustrated in Figure 11, according to α_F. Seen from Figure 11(a), the maximum top

displacement, is sharply decreased from 260mm in Bare model (a portal frame without damping devices) to 131mm ($\alpha_F = 0.5$), 77mm ($\alpha_F = 1.0$), and 74mm ($\alpha_F = 1.5$) in BRB models. These values are below $1.7\delta_y$ (about 133mm for the example piers), which denotes light damage to the steel bridge piers of portal frame type [17]. Referring to Figure 11(b), in the case of $\alpha_F = 0.5$, the normalized axial deformation of BRB, $\varepsilon_{max} / \varepsilon_y)_{BRB}$, is 28.2. As α_F is increased from 0.5 to 1.0, a rapid decrease of deformation of dampers is observed, indicating a decrease in damage to the dampers. Meanwhile, increasing α_F from 1.0 to 1.5, the peak responses are improved a little. When α_F equals 1.5, the main frame remains in elastic range. This fact indicates that the main frames can remain intact even under major earthquake. Energies dissipated by the dampers are shown in Figure 11(c), and the stable energy dissipating capacity of the dampers is confirmed in all the cases.

Comparison of the efficiency of dampers under various strong ground motions are shown in Figure 12. The square-shaped frame with $\alpha_F = 1.0$ is adopted. Clearly, top displacement demands of BRB models have sharply decreased compared with those of the Bare model as shown in Figure 12(a). Meanwhile, the average compression strains as shown in Figure 12(c) have decreased within $2\varepsilon_y$, which denotes light damage to the steel bridge piers of portal frame type [17]. Figure 12(b) indicates that the total base shear resulting from the added stiffness is no more than twice of the original one. Thus, the shear force to be transmitted to foundations is still in the range of the original design force. No additional foundation retrofit is required.

5.2   Efficiency of Dampers Installed in Multi-deck Bridge Piers

Dynamic analysis results of multi-deck bridge piers are summarized in Table 2. Major findings obtained from single-deck ones can be extended to multi-deck ones. Distinguished from single-deck ones, multi-deck bridges piers have a particular problem of distribution of damping devices into the levels. Referring to the plastic energy dissipated by the dampers at each level as shown in Table 2, in the case of F2-BRB-03, the energy dissipated averagely by the dampers in the first level and the second level equal to 0.470 and 0.529, respectively. This case has shown suitable distribution of stiffness and strength of damping devices. However, the case of F2-BRB-05 exhibits the highly unequal distribution of plastic energy. The damper in the first level dissipates 0.225 of the total plastic energy while in the second level it is 0.739. Although the strength ratio increases from 0.3 to 0.5, the F2-BRB-05 case produces larger strains and top displacements than the F2-BRB-03 case. Non-uniform distribution of dissipated energy can be found in F3-BRB-03 as well. The optimum distribution of damping devices into bridge structures will be one of the important issues in the future research.

5.3   Efficiency of Dampers Installed in Arch Bridges

As shown in Figure 13, time-history analyses are conducted on the original arch bridge as well as two bridges with some diagonal braces being replaced by BRBs. In Figure 13(a), over-plasticization occurs at the side pier and arch rib bases, which may make the original bridge fail during a major earthquake. Hence two upgrading schemes are performed. In Figure 13(b), lateral braces of the side piers are replaced by six BRBs to reduce the strain demand. In Figure 13(c), additional six BRBs replace the diagonals near two arch rib bases. Differing from the previous direct design, design of BRB members in arch bridges involves iterations due to the structural complexity. The BRB members are expected to behave in the elastic range under moderate earthquakes, while yield prior to other members when subjected to major earthquakes.

Performance upgrading effect of replacing by BRB can easily be found from analysis results. The maximum axial force demand at the side pier base is decreased from about $P_{y,BRB}$ in the Original Model to lower than $0.5P_{y,BRB}$ in the two Upgrading Models. Seen from Figure 13(b) in Upgrading

Model 1, placement of BRB members only at side pier location decreases the strain demand at side pier base sharply from $-29\varepsilon_y$ to $-2.79\varepsilon_y$. However, a decrease of stiffness in this region results in an increase of strain demand at the arch rib base. The strain demand at the arch rib base increases from $-2.51\varepsilon_y$ in the Original Model to $-4.49\varepsilon_y$ in Upgrading Model 1. On the other hand, in Upgrading Model 2 as shown in Figure 13(c), additional placement of BRB members in arch ribs decreases the strain demand at the side pier base to $-1.38\varepsilon_y$ and decreases the strain demand at the arch rib base low to the elastic range. Large plasticity is concentrated at the BRB members, where the strain demand is about $-7.85\varepsilon_y$.
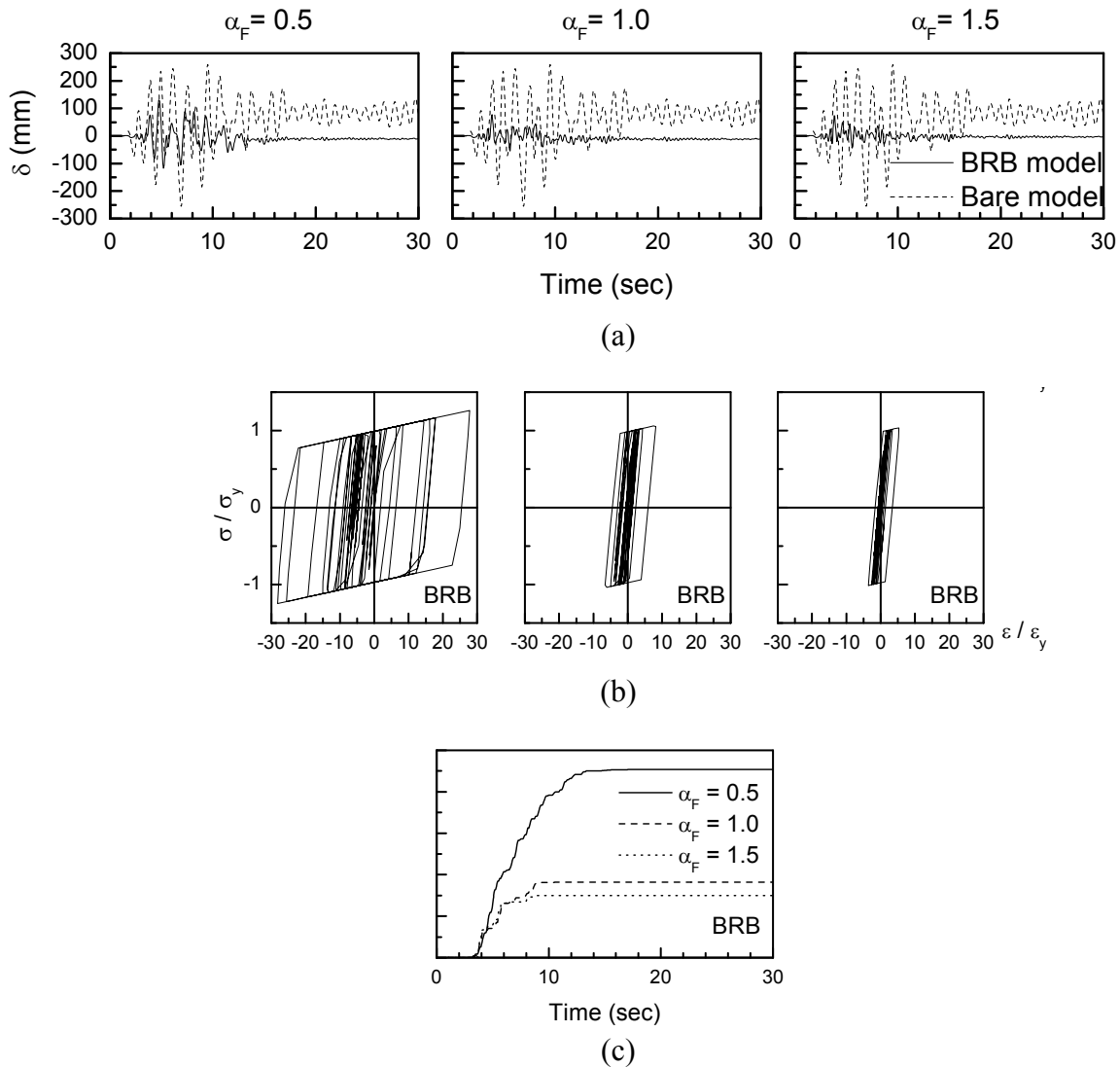
Figure 11. Responses from Time-history Analysis: (a) Top Displacement Responses; (b) Stress-strain Responses of Dampers; and (c) Energy Dissipated by Dampers
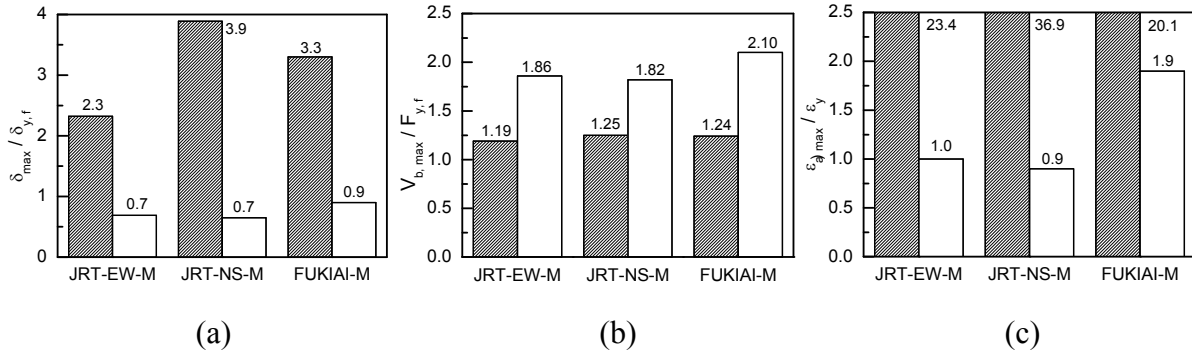
Figure 12. Comparison under Various Strong Earthquakes: (a) Normalized Top Displacement Demands; (b) Normalized Base Shear Demands; and (c) Normalized Average Compression Strain Demands at Pier Bases

Table 2. Summary of Design and Analysis Results for
Multi-deck Bridge Piers with or without Dampers

Model	Time–history analysis results								
	$\dfrac{\varepsilon_{a)max}}{\varepsilon_y}$	δ_{max} (m)	$V_{b,max}$ ($\times 10^3$kN)	$\left.\dfrac{\varepsilon_{max}}{\varepsilon_y}\right)_{BRB}$	$\dfrac{E_f}{E_p}$	$\dfrac{E_{d,1}}{E_p}$	$\dfrac{E_{d,2}}{E_p}$	$\dfrac{E_{d,3}}{E_p}$	E_p ($\times 10^6$J)
F2-Bare	27.8	0.531	11.1	–	1.000	–	–	–	26.7
F2-BRB-03	1.11	0.154	16.3	5.2	0.001	0.470	0.529	–	8.59
F2-BRB-05	1.65	0.169	23.1	4.6	0.006	0.255	0.739	–	6.67
F3-Bare	21.5	0.699	10.7	–	1.000	–	–	–	18.7
F3-BRB-03	1.38	0.289	19.4	9.4	0.002	0.193	0.484	0.321	11.6

Note: F2 and F3 stand for double and tri-deck bridge piers, respectively. Bare and BRB represent piers without and with BRB members, respectively. The numbers (03 and 05) represent the values of the strength ratio α_F at each level. $\varepsilon_{a)max}/\varepsilon_y$ represents the normalized average compression strain measured at critical member segments; δ_{max} is top displacement demand; $V_{b,max}$ is base shear demand; $\varepsilon_{max}/\varepsilon_y)_{BRB}$ represents the normalized axial strain demand of BRB; E_p represents the total plastic energy; E_f and $E_{d,i}$ represent plastic energy in the main structure and in the dampers of each level, respectively, where $i = 1, 2,$ and 3.

(a) Original Model   (b) Upgrading Model 1

Side pier base (-1.38ε_y)

BRB (-7.85ε_y)
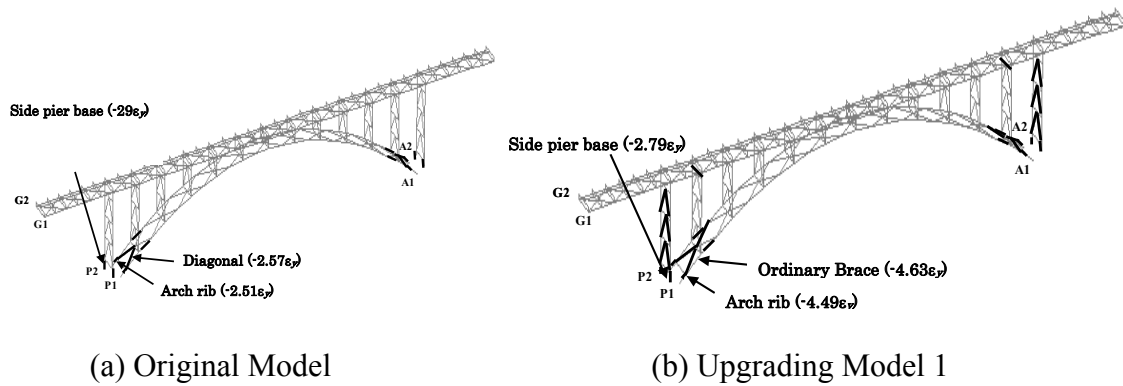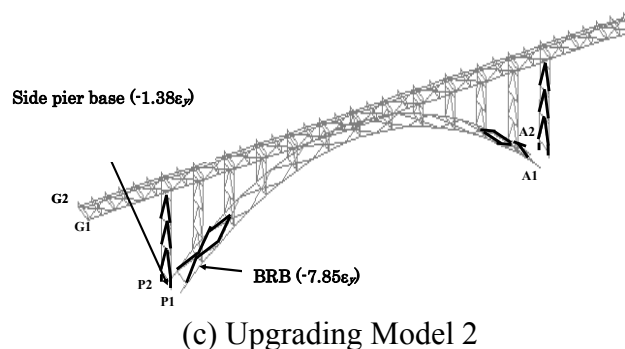
(c) Upgrading Model 2

Figure 13. Yielded Members in the Original and Upgrading Models

6.   SUMMARY AND CONCLUSIONS

This paper presented an investigation on the seismic upgrading efficiency of the buckling-restrained braces (BRB) under major earthquakes. Three types of bridge structures are used as illustrative examples. 2D and 3D finite element models are established and dynamic nonlinear time-history analyses are performed. It has been shown that BRB members are effective in dissipating earthquake-induced energy and eliminating or limiting damage to the main structures.

REFERENCES

[1]   Zahrai, S.M. and Bruneau, M., "Ductile End-diaphragms for the Seismic Retrofit of Slab-on-girder Steel Bridges", Journal of Structural Engineering, ASCE, 1999, Vol. 125, No. 1, pp. 71-80.

[2]   Usami, T., Lu, Z.H. and Ge, H.B., "A Seismic Upgrading Method for Steel Arch Bridges Using Buckling-restrained Braces", Earthquake Engineering and Structural Dynamics, 2005, Vol. 34, pp. 471-496.

[3]   Yamaguchi, M., Yamada, S., Maeda, Y., Ogihara, M., Takeuchi, T., Narikawa, M., Nakashima, M. and Wada, A., "Evaluation of Seismic Performance of Partial Frames using the Shaking Table Test-Seismic Performance of Moment Resisting Steel Frame with Damper: Part 2", Journal of Structural and Construction Engineering, AIJ, 2001, Vol. 547, pp. 153-160.

[4]   Tena-Colunga, A. and Vergara, A., "Comparative Study on the Seismic Retrofit of a Mid-rise Steel Building: Steel Bracing vs Energy Dissipation", Earthquake Engineering and Structural Dynamics, 1997, Vol. 26, pp. 637-655.

[5]   Ye, L.P. and Ouyang, Y.F. "Dual Seismic Structure System and its Parametric Analysis", Engineering Mechanics, 2000, Vol. 17, No. 2, pp. 23-29.

[6]   Inoue, K. and Kuwahara, S., "Optimum Strength Ratio of Hysteretic Damper", Earthquake Engineering and Structural Dynamics, 1998, Vol. 27, pp. 577-588.

[7]   Yamaguchi, H. and Ashraf, E.A., "Effect of Earthquake Energy Input Characteristics on Hysteretic Damper Efficiency", Earthquake Engineering and Structural Dynamics, 2003, Vol. 32, pp. 827-843.

[8]   Kato, M., Usami, T., Kasai, A. and Chusilp, P., "An Experimental Study on Cyclic Elasto-plastic Behavior of Buckling Restrained Brace Members", Proceedings of the 6th Symposium on Ductility Design Method for Bridges, Ductility Design Subcommittee, Earthquake Engineering Committee, JSCE, Tokyo, Japan, 2003, pp. 345-350.

[9]   Usami, T., Kasai, A. and Kato, M., "Behavior of Buckling-restrained Brace Members", Behaviour of Steel Structures in Seismic Areas, STESSA, Naples, Italy, 2003, pp. 211-216.

[10]   JRA, "Design Specifications of Highway Bridges-Part V Seismic Design", Japan Road Association, Tokyo, Japan, 2002a. (in Japanese)

[11]   JRA, "Design Specifications of Highway Bridges-Part II Steel Bridges", Japan Road Association, Tokyo, Japan, 2002b. (in Japanese)

[12]   Usami, T., Zheng, Y. and Ge, H.B., "Seismic Design Method for Thin-walled Steel Frame Structures", Journal of Structural Engineering, ASCE, 2001, Vol. 127, pp. 137-144.

[13]   Eurocode 8, "Design of Structures for Earthquake Resistance. General Rules, Seismic Actions and Rules for Buildings", British Standards Institution, London, 2003.

[14]   FEMA 356, "Prestandard and Commentary for the Seismic Rehabilitation of Buildings", Federal Emergency Management Agency, Washington DC, 2000.

[15]   Chopra, A.K. and Goel, R.K., "A Modal Pushover Analysis Procedure for Estimating Seismic Demands for Buildings", Earthquake Engineering and Structural Dynamic, 2002, Vol. 31, pp. 561-582.

[16]   ABAQUS/Analysis user's Manual—Version 6.4. ABAQUS, Inc., Pawtucket, R.I., 2003.

[17]   Usami, T. ed., "Seismic Performance-based Verification Procedures and Upgrading Measures for Civil Engineering Steel Structures", Subcommittee for Seismic Design of Steel Bridges, Task Committee of Performance-Based Seismic Design Methods for Steel Bridges, Tokyo, 2003.

[18]   Shen, C., Mamaghani, I.H.P., Mizuno, E., and Usami, T., "Cyclic Behavior of Structural Steels. II: Theory", Journal of Engineering Mechanics, ASCE, 1995, Vol. 121, No. 11, pp. 1165-1172.

HYBRID COMPOSITE CABLE WITH STEEL COMPONENT AS A STRUCTURAL ELEMENT

D. Serdjuks [1,*] and K. Rocens[2]

[1] Assistant Professor, Institute of Structural Engineering and Reconstruction,
Riga Technical University, Latvia
[2] Professor, Institute of Structural Engineering and Reconstruction,
Riga Technical University, Latvia
*(Corresponding author: E-mail: dmitrijs@bf.rtu.lv)

ABSTRACT: High strength composite cables with large specific strength and made of base of materials using carbon fiber reinforced plastics (CFRP), glass fiber reinforced plastics (GFRP) and Vectran, are widely used in construction industry. However, the use of a steel component enables the small elongation of the cable to be moderately increased, the brittleness decreased and the scope of application of high strength composite cables expanded respectively. Cable made of steel in combination with other materials such as CFRP, GFRP and Vectran, was studied and reported in this paper. Volumetric fraction of steel was within the limits of 0.1 to 0.7. The inter-dependent relationship of external pressure per unit surface area of the distributed layer (due to the pressure of steel wire strands) of hybrid composite cable on the axial force and angle of steel wire strands twisting was estimated by engineering method of calculations. Tangential and radial stresses of the distributed layer and core of hybrid composite cable were obtained. It was shown that the angle of steel wire strands twisting should not exceed 20º in the case when the distributed layer and core are made of GFRP and CFRP respectively. Relationship between materials and their content in hybrid composite cables with the steel component was considered. Hybrid composite cables with the steel component were considered as materials of several groups of cables in a prestressed saddle-shaped cable roof. Opportunity to decrease the displacements of composite saddle-shaped cable roof by the use of hybrid composite cables with steel component in several groups of cables was investigated and reported.

Keywords: Steel wire strands, fiber reinforced plastics, cable net, vertical displacements

1.   INTRODUCTION

High strength materials such as FRCC and FRP possess potential for their application as construction materials in combination with the steel. Carbon fiber reinforced plastic (CFRP), glass fiber reinforced plastic (GFRP) and Vectran are examples of such materials. As construction materials they have the following advantages:
– high specific strength;
– good durability in aggressive surrounding;
– CFRP is adaptable to be used in structures not allowed to be magnetic or electrically conductive;
– low density.

However, CFRP, GFRP and Vectran have a number of disadvantages, limiting their application as construction materials. Relatively small elongation at break, probability of surface damages and increased cost are most significant imperfections of CFRP, GFRP and Vectran in comparison with the steel cables.

Small elongation at break significantly decreases safety of construction due to the probability of brittle failure during short time growing of the load. This disadvantage could be improved by adding of the steel component, which enables to increase reliability of the cable. Addition of the distributed layer, which could be made of glass fiber reinforced plastic (GFRP), significantly decreases the possibility of surface damages of CFRP in hybrid composite cable.

So, the surface pressure of steel wire strands at the distributed layer and that of distributed layer at the core of hybrid composite cable should be evaluated together with the radial and tangential stresses in the distributed layer and core.

Increased cost of CFRP in comparison with the steel cables could be partially compensated by the application of CFRP in economic, from the point of view of material consumption, constructions. One of CFRP utilization in practice is its application as tendons for the cable bridges. Saddle-shaped cable roof is another potential example of CFRP application as a construction material. Saddle-shaped cable roof is a type of constructions where such high strength construction materials as CFRP could be used on the full scale, because nearly all the load bearing elements are tensioned. However, the most significant disadvantage of the saddle-shaped cable roofs supported by the tensioned cables is the increased compliance. One of the eventual methods to decrease the compliance of the cable roofs is using of the cables with the increased moduli of elasticity. Hybrid composite cable on the base of steel, CFRP, GFRP and Vectran can be considered as an example of such a cable (Figure 1).
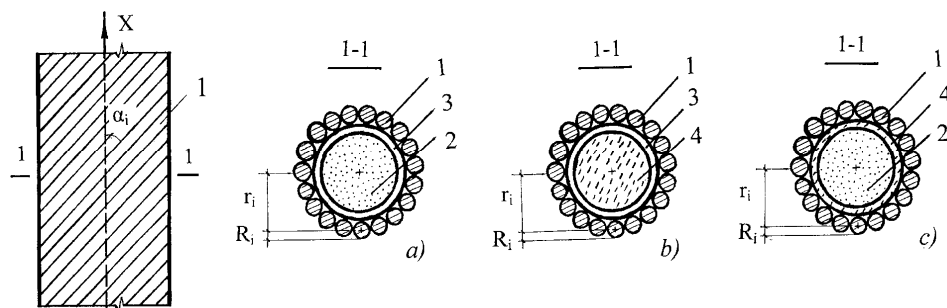
Figure 1. Hybrid Composite Cables on the Base of Steel, CFRP, GFRP and Vectran: 1 – Steel Component; 2 – CFRP Component; 3 – GFRP Component; 4 – Vectran Component; a) – Variant on the Base of Steel, GFRP and CFRP; b) – Variant on the Base of Steel, GFRP and Vectran; c) – Variant on the Base of Steel, Vectran and CFRP; α_i – Angle of Steel Wire Strands Twisting; X – Longitudinal Axis of the Cable; r_i – Distance between the Center of Separate Steel Wire Strand and Whole Cable; R_i – Radius of Separate Steel Wire Strand

Another method is to use the cable trusses made of the materials with the increased moduli of elasticity as structures of the supporting contour of cable roof.

The purpose of this study is to consider behavior of hybrid composite cable on the base of steel, CFRP, GFRP, Vectran. Opportunity to decrease the displacements of the composite saddle-shaped cable roof by using of hybrid composite cables with the steel component for several groups of cables should be investigated.

2. EVENTUAL MATERIALS COMBINATIONS FOR HYBRID COMPOSITE CABLES

The main directions of the considered hybrid composite cables application are prestressed nets of saddle-shaped roofs. Two types of hybrid composite cables have been investigated. First of them is a hybrid composite cable with an increased, in comparison with the CFRP, ultimate elongation and decreased, in comparison with the steel, dead weight. This type of the cables could be used for the tension and suspension cables forming the prestressed nets. Second is a hybrid composite cable with relatively high ultimate elongation for the stressing cables of the prestressed nets.

Combination of high strength and increased ultimate elongation is the main requirement for the first hybrid composite cable type. But the second type, unlike the first, should possess first of all, an increased ultimate elongation.

Thus, the first cable type should obligatorily contain two kinds of materials: one material with a large limit of strength and the other with an increased ultimate elongation. The third type of materials should be added to transfer pressure of the external layer to the surface of the internal one which is perpendicular to the direction of axial force action.

Steel wire strands can be treated as a material with an increased up to 10% ultimate elongation for the first type of the cable. Properties of GFRP (E-glass and epoxy matrix at 60% fiber content), CFRP (AS4/3501-6 graphite fibers and epoxy matrix at a 60% fiber content), Vectran HS 1500 and strands of steel wire are indicated in Table 1 (e.g. Beers and Ramirez [1]; Bengtson [2]; Berger [3]; Blum [4]; Houtman [5] and Peters [6]).

Table 1. Mechanical Properties of Hybrid Composite Cables Components

Components of hybrid composite cabes	E, MPa	R_u, MPa	ε_u, %
Steel wire strands	200000	1900	10
GFRP	75000	760	2.64
CFRP	137000	2100	1.6
Vectran	65000	2850	3.3

* In Table 1 moduli of elasticity E, limits of strength R_u, and breaking elongations ε_u are given in the longitudinal direction X.

Based on the materials properties given in Table 1, two following material combinations can be considered for the first type of hybrid composite cable: steel, GFRP, CFRP and steel, Vectran, CFRP.

Second type of the cables should be based on the material with the increased ultimate elongation and limit of strength, which is enough to take up tension forces, acting in the stressing cables of the net. Combination of steel, Vectran and GFRP, probably, enables to obtain hybrid composite cables with such properties.

3. EVALUATION OF MECHANICAL INTERACTION BETWEEN COMPONENTS IN HYBRID COMPOSITE CABLE

3.1 Approach to the Solution of the Problem

Hybrid composite cable is considered as a system of two cylinders (Figure 2). Steel wire strands are replaced by the external pressure p_b per unit of external surface area of the GFRP distributional layer.

The GFRP distributed layer is considered as a hollow cylinder inside which another cylinder, i.e., CFRP core is situated. The GFRP distributional layer has constant internal and external radii: a and b, respectively. The CFRP core has constant external radius, which is equal to a.

Interaction between the GFRP distributed layer and CFRP core is considered as a pressure p_a per unit of the surface area of the CFRP core or per unit of internal surface area of the GFRP distributed layer.
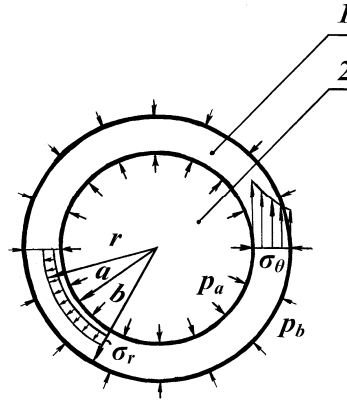
Figure 2. Scheme for Determination of Pressure at the CFRP core of Hybrid Composite Cable: 1 – GFRP Distributed Layer; 2 – CFRP Core; σ_r – Radial Stresses; σ_θ – Tangential Stresses; p_b – External Pressure Per Unit of the Surface Area of the GFRP (Due to the Pressure of Steel Wire Strands); p_a – External Pressure Per Unit of the Surface Area of the CFRP (Due to the Pressure of GFRP); a – Radius of the CFRP Core of the Cable and Internal Radius of GFRP Distributed Layer; b – External Radius of the GFRP Distributed Layer

Interaction between the GFRP distributed layer and CFRP core is considered as a pressure p_a per unit of the surface area of the CFRP core or per unit of internal surface area of the GFRP distributed layer.

Pressure p_b per unit of external surface area of the GFRP distributed layer could be determined by the following equation:

$$p_b = -\frac{ntg^2\alpha_i}{2\pi aR}, \tag{1}$$

where: n – part of axial force N, which takes up steel wire strands of the cable; α_i – angle of steel wire strands twisting; a – radius of the CFRP core; R – radius of the cable.

Eq. 1 was obtained for the case, when GFRP distributed layer limits the displacements of the steel wire strands in the radial direction. Pressure p_a per unit of the surface area of the CFRP core and per unit of internal surface area of the GFRP distributed layer could be determined by the Eq. 2. The Eq. 2 is obtained due to the equal radial deformations of CFRP core and GFRP distributed layer:

$$\frac{1-v_{Grx}}{E_{Gr}}\frac{p_a a^2 - p_b b^2}{b^2 - a^2}r + \frac{1+v_{Grx}}{E_{Gr}}\frac{a^2b^2(p_b - p_a)}{(b^2 - a^2)r} + \delta_{Gr} = \frac{1-v_{Crx}}{E_{Cr}}p_a r + \delta_{Cr}, \tag{2}$$

where E_{Gr}, E_{Cr} = modulus of elasticity for GFRP and CFRP, respectively, in the radial directions; r = coordinate of the point, where deformations are determined; v_{Grx} = Poisson's ratio of GFRP; v_{Crx} = Poisson's ratio of CFRP; a = radius of the CFRP core of the cable and internal radius of GFRP distributed layer; b – external radius of the GFRP distributed layer; δ_{Gr} = radial deformations of GFRP due to the part of axial force, acting in the GFRP component of the cable; δ_{Cr} = radial deformations of CFRP due to the part of axial force, acting in the CFRP component of the cable.

The left and right parts of the Eq. 2 are radial deformations of GFRP and CFRP components, respectively, due to the pressures p_b and p_a. Radial deformations of GFRP and CFRP components δ_{Gr} and δ_{Cr} due to the parts of axial force, acting in the components also are taken into account.

Values of radial deformations of GFRP and CFRP components δ_{Gr} and δ_{Cr} were determined basing on the consumption that components work in the elastic stage. Radial and tangential stresses act in the GFRP and CFRP due to the pressure p_b. The values of radial and tangential stresses could be determined by the equations which were obtained for the cylinder with the hole in the center, which is loaded by uniformly distributed by the internal and external surfaces pressures p_a and p_b, respectively.

$$\sigma_{Gr} = \frac{a^2 b^2 (p_b - p_a)}{(b^2 - a^2)} \frac{1}{r^2} + \frac{p_a a^2 - p_b b^2}{b^2 - a^2},$$ (3)

$$\sigma_{G\theta} = -\frac{a^2 b^2 (p_b - p_a)}{(b^2 - a^2)} \frac{1}{r^2} + \frac{p_a a^2 - p_b b^2}{b^2 - a^2},$$ (4)

where σ_{Gr} and $\sigma_{G\theta}$ = stresses acting in the GFRP component of hybrid composite cable in the radial and tangential directions.

For determination of radial and tangential stresses acting in the CFRP component of the hybrid composite cable, the following equation could be used:

$$\sigma_{Cr} = -p_a = \sigma_{C\theta},$$ (5)

where: σ_{Cr} and $\sigma_{C\theta}$ = stresses acting in the CFRP component of hybrid composite cable in the radial and tangential directions.

Eq. 5 was obtained from the Eq. 3 and 4 when the internal radius of the cylinder (CFRP core) is equal to zero, external radius of the cylinder is equal to a, and external pressure per unit of the surface area of the CFRP (due to the pressure of GFRP) is equal to p_a.

3.2   Determination of Pressures on the Components of Hybrid Composite Cables

The relationship between the pressure at the CFRP core of hybrid composite cable and the axial force N and angle of wire twisting α was developed by the example of tension cable of saddle-shaped cable roof with dimensions in plan 30x30m.

Cable, which is loaded by the uniformly distributed load, is considered as a scheme for analysis. From the point of view of materials consumption, the cable has rational initial deflection $f_l = 5.7$ m. The uniformly distributed load with intensity $q = 21$ kN/m loads the cable (Figure3).

Poisson's ratios in radial direction of GFRP and CFRP are equal to 0.05, 0.014, respectively. Limits of strength of GFRP and CFRP in radial direction are equal to 78 and 186 MPa, respectively.

The values of moduli of elasticity correspond to the elastic stages of the materials work. Volume fractions of fibers in GFRP and CFRP are 0.6. The fibers are oriented in the direction of axial force action. Volume fractions of steel wire, GFRP and CFRP are 0.4; 0.2 and 0.4, respectively. Total area of cross sections for hybrid composite cable was equal to 0.001 m^2.

The value of the axial force N, acting in the cable due to the uniformly distributed load, was determined in two stages. First it was evaluated by the approximate method. Than the value of axial force was adjusted by the computer program "ANSYS/ED 5.3" with taking into account elastic elongation of the cable.
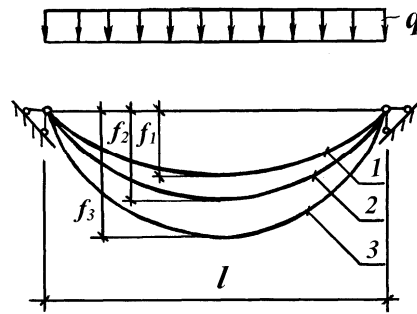
Figure 3. Scheme of Hybrid Composite Cable Work: 1 - Steel Wire, GFRP and CFRP Work Commonly; 2 - GFRP is Excluded from the Work; 3 - GFRP with CFRP are Excluded from the Work and Steel Wire Works Alone; q - Design Vertical Load, Acting at the Cable; f_1 - Deflection of the Cable, which Corresponds to the Stage, when Steel Wire, GFRP and CFRP Work Commonly; f_2 - Deflection, which Corresponds to the Stage, when GFRP is Excluded from the Work and Steel Wire Works Commonly with CFRP; f_3 - Deflection, which Corresponds to the Stage, when GFRP and CFRP are Excluded from the Work and Steel Wire Works Alone; l - Span of the Cable
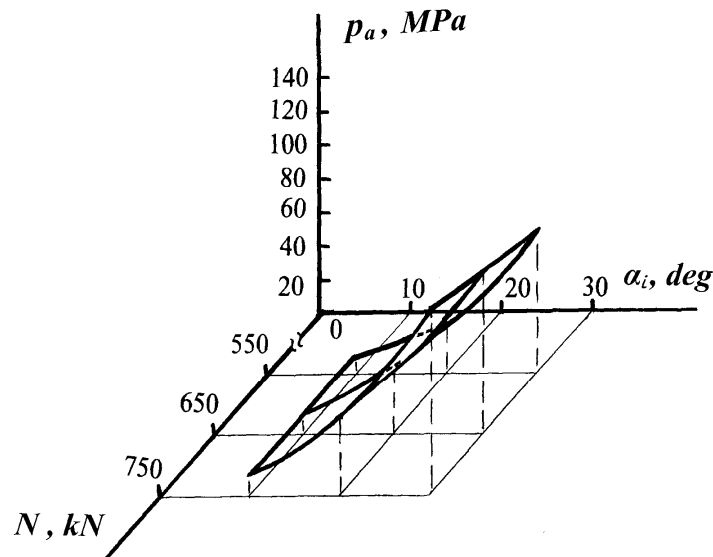
Figure 4. Relationship between the Pressure p_a, Axial Force N and Angle of Steel Wire Strands Twisting α_i.

Relationship between the pressure p_a, axial force N and angle of steel wire strands twisting α_i is shown in Figure 4. The upper limit of the axial force is equal to 750 kN because with the further growing of the axial force the GFRP component of the cable is excluded from the work. The value of the axial force N, acting in the cable, changes within the limits of 550 to 750 kN.

3.3 Determination of Radial and Tangential Stresses, Acting in the Components of Hybrid Composite Cable

Relationship between the maximum radial σ_{Cr}, tangential stresses $\sigma_{C\theta}$, acting in the CFRP component of the hybrid composite cable and the axial force N is shown in Figure 5.
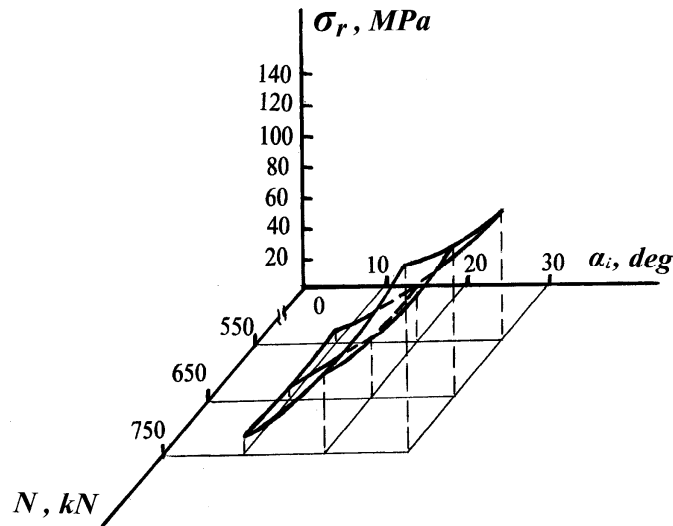
Figure 5. Relationship between the Radial σ_{Cr}, Tangential $\sigma_{C\theta}$ Stresses Acting in the CFRP and the Axial Force N and Angle of Steel Wire Strands Twisting α_i

The values of the radial and tangential stresses are equal for the CFRP component of hybrid composite cable.

Comparison of the maximum radial stresses σ_{Cr}, acting in the CFRP components of the hybrid composite cable with their strengths shows that the stresses are 1.65 times less, than the strength values, but the maximum values of tangential stresses $\sigma_{C\theta}$ are 13.79 times less, than the strength value. Maximum values of radial stresses were compared with the compression strength of CFRP in the direction perpendicular to the direction of fiber orientation, which is equal to 186 MPa. Tangential stresses were compared with the compression strength of CFRP in the direction corresponding to that of fiber orientation, which is equal to 1558 MPa.

The maximum values of radial σ_{Gr} and tangential $\sigma_{G\theta}$ stresses acting in the GFRP component of hybrid composite cable are given in Table 2 depending on the angle of steel wire strands twisting α_i. The maximum values of radial and tangential stresses were obtained when the axial force N, acting in the cable, was equal to 750 kN and $r = a$.

Table 2. Maximum Radial and Tangential Stresses,
Acting in the GFRP Component of Hybrid Composite Cable

Angle of steel wire strands twisting α_i,°	σ_{Gr}, MPa.	$\sigma_{G\theta}$, MPa.
10	10.77	21.29
20	45.02	44.85
30	114.81	93.32

Comparison of the maximum tangential and radial stresses, acting in the GFRP components of the hybrid composite cable with their strengths shows, that the maximum angle of steel wire strands twisting for the considered case is 20°, when the radial stresses are equal to 45.02 MPa, which are 1.73 times less than the strength value.

4.   EVALUATIONS OF MECHANICAL PROPERTIES OF HYBRID COMPOSITE CABLES

4.1   Evaluation of Modulus of Elasticity of Hybrid Composite Cables

Let us to determine behaviors of three variants of hybrid composite cables. The behaviors of hybrid composite cables are defined by the dependence of proportional components summing on the base of behaviors of separate components.

Generally known dependence of proportional components summing was used for the engineering evaluation of modulus of elasticity of the hybrid composite cable. The dependences are given for the variant of the hybrid composite cable on the base of steel, GFRP and CFRP.

$$E = \Omega_C E_C + (1 - \Omega_C - \Omega_S)E_G + \Omega_S E_S , \tag{6}$$

where

$$\Omega_C = \frac{A_C}{A}, \Omega_S = \frac{A_S}{A}, \tag{7}$$

$$E_S = \frac{\sum_{i=1}^{n} m_i A_i E_i \sin(90 - \alpha_i)\left[1 - (1+v)p_i \cos^2 \alpha_i\right]}{A_S}, \tag{8}$$

$$A_i = \pi r_0^2 , \tag{9}$$

$$p_i = \left(1 - v\frac{R_i}{r_i}\cos^2(90 - \alpha_i)\right) \times$$

$$\left[1 - \frac{R_i^2}{4r_i^2}\left(1 - \frac{v}{1+v}\cos^2(90 - \alpha_i)\right)\cos^2(90 - \alpha_i)\right], \tag{10}$$

where: E = modulus of elasticity of hybrid composite cable; A = cross-sectional area of hybrid composite cable; A_C, A_S = cross-sectional areas of CFRP and steel components, respectively; E_C, E_G, E_S = moduli of elasticity of CFRP, GFRP and steel components, respectively; m_i = amount of steel wires in the i-th strand; A_i = cross-sectional area of the separate steel wire in the i-th strand; r_0 = radius of separate steel wire; E_i = modulus of elasticity of steel wire; α_i - angle of i-th steel wire strands twisting; v = Poison's ratio of steel wire; R_i = radius of i-th steel wire strand; r_i = distance between the centers of i-th steel wire strand and cable.

Modulus of elasticity of the steel component of the hybrid composite cable was evaluated by the method of Cumar and Cochran (e.g. Costello [7]; e.g. Cumar and Cochran [8]).

4.2   Character of Deformations of Hybrid Composite Cables

The relationship between the strain ε and the force N, acting in the cable, was obtained for three variants of composite cables with the area of cross-sections equal to 0.001 m^2. Empty space was not taken into account. The relationship was obtained on the base of stress-strain curves of separate components (e.g. Beers [1], Bengtson [2] and Peters [6]). Following consumptions were considered. The steel wire and GFRP are working in the elastic stage till the strains, which are equal to 0.95 and 1%, respectively. Then occurs yielding till the ultimate strains of 10 and 2.64%, respectively. The CFRP and Vectran components are working in the elastic stage till the ultimate strains of 1.6 and 3.3%, respectively.

Volumetric fraction of steel for each variant changes within the limits of 0.1 to 0.7. Volume fractions of GFRP in the two first variants and Vectran in the third variant of hybrid composite cables were constant and equal to 0.2. Angle of steel wire strands twisting was adopted equal to 12 degrees on the base of the previous investigations and literature recommendations.

The relationship between the strain ε and the force N, acting in the cable, for hybrid composite cable on the base of steel, GFRP and CFRP is shown in Figure 6.

The relationship illustrates, that increase of volumetric fraction of steel from 0.1 to 0.7 enables the increase by 20.4% the value of the force, which can be taken up by the cable. The value of the force corresponds to 0.95% value of the strain. Modulus of elasticity of the cable grows from $1.25 \cdot 10^5$ to $1.57 \cdot 10^5$ MPa at the same time.
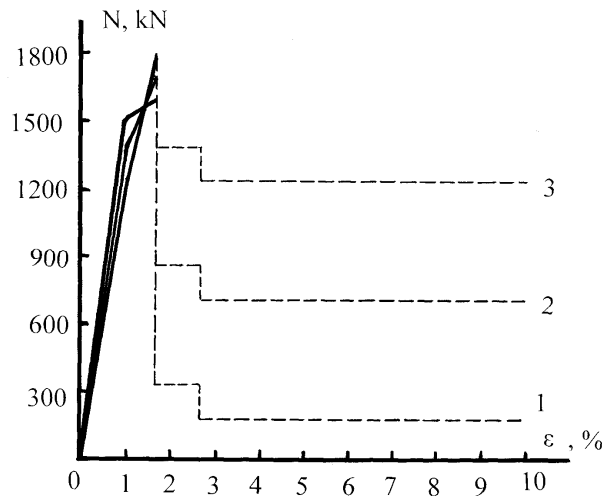
Figure 6. Strain of Hybrid Composite Cable on the Base of Steel, GFRP and CFRP ε vs. the Force N, Acting in the Cable: 1,2,3 – the Relationships, which were Obtained at Volumetric Fractions of Steel, Equal to 0.1; 0.4; 0.7, Respectively; (————) – Stage, when all the Components of the Cables Work Commonly; (------) – Stage, when some Components are Disrupted

The relationship between the strain ε and the force N, acting in the cable, for hybrid composite cable on the base of steel, GFRP and Vectran is shown in Figure 7.
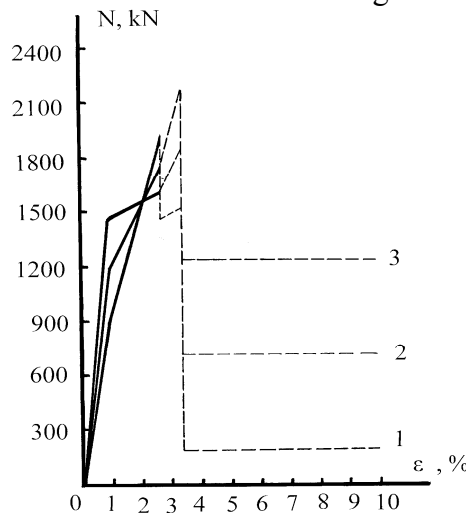
Figure 7. Strain of Hybrid Composite Cable on the Base of Steel, GFRP and Vectran ε vs. the Force N, Acting in the Cable: 1,2,3 – the Relationships, which were Obtained at Volumetric Fractions of Steel, Equal to 0.1; 0.4; 0.7, Respectively; (————) – Stage, when all the Components of the Cables Work Commonly; (------) – Stage, when some Components are Disrupted

The relationship illustrates, that increase of the volumetric fraction of steel from 0.1 to 0.7, increases by 1.63 times the value of the force, which can be taken up by the cable. Modulus of elasticity of the cable grows from $0.94 \cdot 10^5$ to $1.53 \cdot 10^5$ MPa at the same time.

The relationship of strain ε and the force N, acting in the cable, for the hybrid composite cable on the base of steel, Vectran and CFRP has a property which is analogous to the dependences shown in Figure 6 and Figure 7. The value of force, which can be taken up by the cable, changes from 1212.5 kN to 1517.8 kN, when the volumetric fraction of steel changes from 0.1 to 0.7. Modulus of elasticity of the cable grows from $1.27 \cdot 10^5$ to $1.6 \cdot 10^5$ MPa at the same time.

Comparison of the relationships between the strain ε and the force N for three variants of hybrid composite cables indicates, that maximum strain (2.64%) without any components disruption possesses a variant on the base of steel, GFRP and Vectran. But the value of the force, which can be taken up by the cable, is a minimum for all the variants and equals to 1453.6 kN. Variants on the base of steel, GFRP, CFRP and steel, Vectran, CFRP have increased values of the forces, which can be taken up by the cables – 1496 and 1517.8 kN, respectively. But the values of maximum strains without any components disruption are equal to 1.6%.

5.   STEEL COMPONENT IN HYBRID COMPOSITE CABLE FOR SADDLE–SHAPED ROOF

Hybrid composite cable on the base of steel, CFRP, GFRP and Vectran was considered as a material for the tension and main diagonal suspension cables of the saddle shaped cable roof since characteristics of the cables have significant influence on the compliance of the structure (e.g. Serdjuks et al. [9, 10, 11]). The cable roof was square in plan with dimensions 50x50 m. The initial deflections of the suspension, stressing and tension cables were equal to 20 and 8.6 m, respectively. The distance between the suspension and stressing cables was equal to 1.414 m. The geometrical characteristics of the cable roof are rational from the point of view of materials consumption (e.g. Serdjuks et al. [12]).

The structure was calculated for the basic combination of loads – the dead weight of the structure (0.27 kPa) and the weight of snow (1.12 kPa) – evenly distributed on the horizontal projection of the roof. The design load in the form of point wise forces was applied to the nodes of the cable net. The roof had the following layers: a glass net coated with polymer resin (2 mm), foam plastic, reinforced with a glass net (120 mm), and saddle-shaped plywood sheets (6 mm).

The cable net was prestressed by applying tension forces to the suspension and stressing cables, such that the residual tension forces in the stressing cables were equal to 20% of their initial values under the vertical design load.

The maximum vertical displacements of the cable roof were determined by the computer program "ANSYS/ED 5.3". The existence of two symmetry planes allows us to regard, as a design scheme, a quarter of the cable net of the saddle-shaped cable roof with a compliant supporting contour (Figure 9). Three quarters of the cable roof were replaced by the bonds imposed on its one-quarter part. The cable net was modeled by the finite element of LINK 10 type, with three degree of freedom for each node. Steel cables with an elastic modulus of $1.3 \cdot 10^5$ MPa were assumed as a material for the suspension and stressing cables, excluding the main diagonal ones.

The relationships between the maximum vertical displacements of the cable net and the volumetric fraction of the steel component in the hybrid composite cables are shown in Figure 8. The relationships were obtained for the stages when all the components of the hybrid composite cables work commonly and when all the components, excluding the steel, were disrupted. Deformations of the cables for the all stages of work were taken into account.

In the case, when all the components of the hybrid composite cable work commonly, the increase of volumetric fraction of the steel from 0.1 to 0.7 causes the decrease of the maximum vertical displacements of the cable roof by 9.31 and 8% for the variants, when the hybrid composite cable is on the base of steel, GFRP and CFRP, steel, GFRP and Vectran and steel, Vectran and CFRP, respectively.
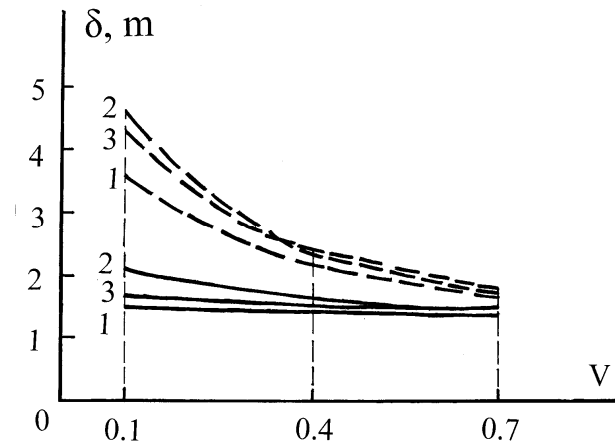
Figure 8. Relationship between the Maximum Vertical Displacements of the Cable Roof δ and the Volumetric Fraction of Steel in Hybrid Composite Cables V: 1− Variant on the Base of Steel, GFRP and CFRP; 2 − Variant on the Base of Steel, GFRP and Vectran; 3− Variant on the Base of Steel, Vectran and CFRP; (———) − Stage, when all the Components of the Cables Work Commonly; (------) − Stage, when all the Components, Excluding the Steel, are Disrupted

In the case of emergency, when all the components, excluding the steel, are disrupted, the increase of volumetric fraction of the steel from 0.1 to 0.7 causes decrease of the maximum vertical displacements of the cable roof by 2.21, 2.78 and 2.46 times for the variants, when hybrid composite cable is on the base of steel, GFRP and CFRP, steel, GFRP and Vectran and steel, Vectran and CFRP, respectively.

The points with maximum vertical displacements of the cable roof are placed approximately in the quarter of the span. Deformed shape of the cable net is shown in Figure 9 *(b)*. This stage of the cable roof works is characterized by the growing of vertical displacements and decrease of the axial forces, acting in the cables. The value of tension stresses, acting in the cables, does not exceed the limit of strength. The serviceability limit stage does not satisfied but the collapse of structure is prevented and evacuation can be organized normally.

Maximum vertical displacements of the cable roof are equal to 4.562 m. The value is 1.9 times less, than the distance down to the surface of the ground. So, we can suppose that the steel component of hybrid composite cable can prevent failure of the cable roof in emergency, when the strain of CFRP, Vectran and GFRP exceeds the ultimate values and these components are disrupted. The using of CFRP, GFRP and Vectran components enables to decrease the dead weight of the cables by 44-47% when the volumetric fraction of steel is equal to 0.4 at the same time.
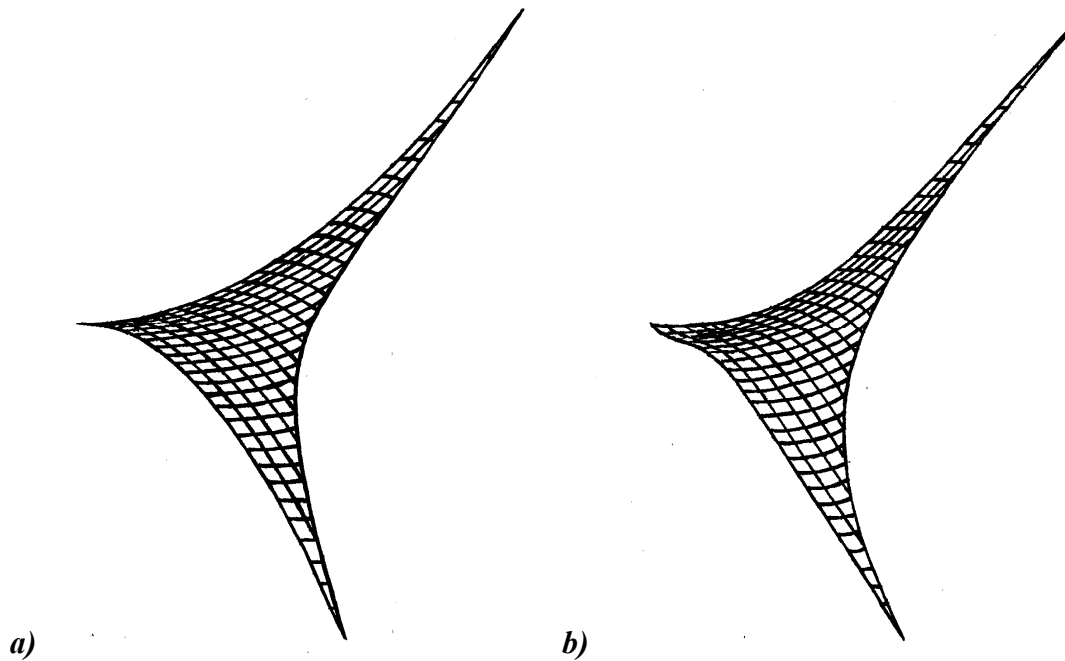
Figure 9. Deformed and Undeformed Shapes of Cable Net Quarter:
a) – Undeformed Shape; b) – Deformed Shape

Possibility to decrease the displacements of the composite saddle-shaped cable roof by using of cable trusses made of the material with the increased modulus of elasticity as structures of supporting contour was considered for the above mentioned example. Hybrid composite cable on the base of steel, GFRP and CFRP was considered as a material of cable truss together with the steel cables, which are considered as a material of suspension and stressing cables. Volumetric fractions of steel and CFRP were equal to 0.4. Volumetric fraction of GFRP was equal to 0.2. Quarter of the cable net with the cable truss as a structure of supporting contour is shown in Figure 10 together with the deformed shape of cable net, which is loaded by the design vertical load.
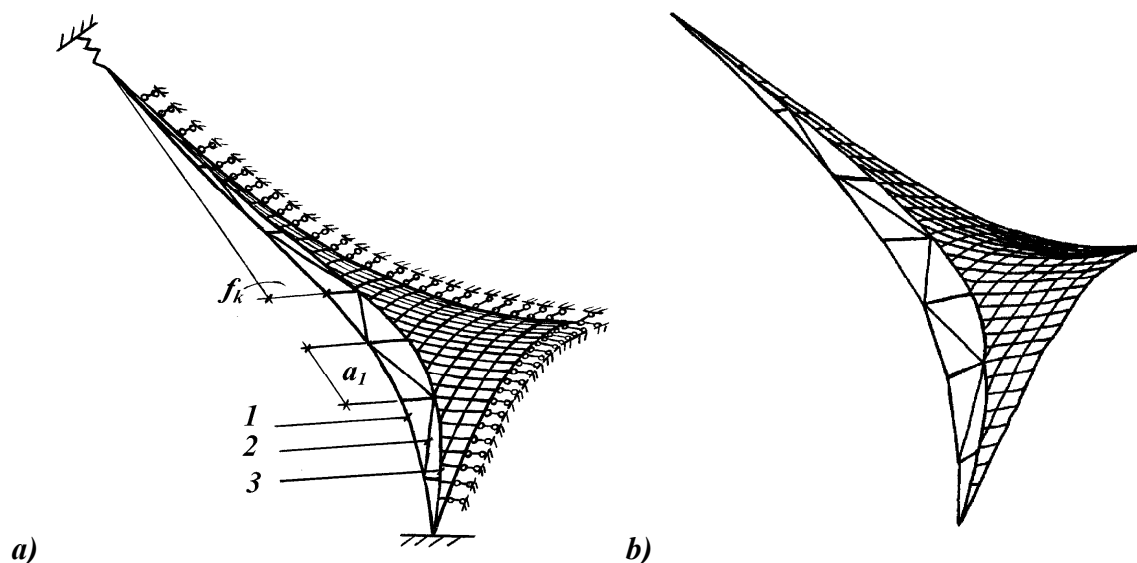
Figure 10. a) Quarter of Cable Net, Supported by Compliant Supporting Contour: 1 – Top Cable of Supporting Contour, 2 – Tie-bar, 3 – Bottom Cable of Supporting Contour, f_{k1} – Initial Deflection of Top Chord of Compliant Supporting Contour, a_l – Distance between the Support Points of Tie-bars. b) Shape of Prestressed Cable Net after Vertical Design Load Application

It was stated, that the minimum values of vertical displacements of cable net were obtained, when the initial deflection of top chord of cable truss were equal to 3.13 m and distance between the nodes of the cable truss was equal to 7 m.

Application of hybrid composite cable as a material of supporting contour instead of steel enables to decrease by 1.3 % maximum vertical displacements of the cable net. The using of the cable truss as a structure of support contour enables to decrease by 8 % the maximum vertical displacements of the cable net in the case, when the tension cables of the net are hybrid composite cables, but suspension and stressing cables of the net are made of steel.

6.   CONCLUSIONS

Hybrid composite cables on the base of steel, GFRP, CFRP and Vectran, which are differed by the components and volume fractions, were considered. The relationship between the external pressure per unit of the surface area of the GFRP (due to the pressure of steel wire strands) p_b of hybrid composite cable and the axial force N and angle of steel wire strands twisting α was obtained.

It was shown, that increasing of angle of steel wire strands twisting α_i from 10 to 30 degrees causes growing of external pressure per unit of the area of CFRP by 14.61 times when the axial force increases from 550 to 750 kN.

Tangential and radial stresses for GFRP and CFRP components of hybrid composite cable were obtained. It was shown, that the maximum angle of steel wire strands twisting α_i is equal to 20º for the considered hybrid composite cable.

It was shown, that maximum radial stresses σ_{Gr} acting in the GFRP component of hybrid composite cable, when the angle of the steel wire strands twisting α_i was equal to 20º, and the axial force N was equal to 750 kN, was 1.73 times less than the strengths of GFRP.

The relationship between strain ε and the force N, acting in the cable, for hybrid composite cables on the base of steel, GFRP, CFRP and Vectran, which are differed by the components and volumetric fractions,   were obtained. It was indicated that increase of volumetric fraction of steel from 0.1 to 0.7 enables to increase the value of the force, which can be taken up by the cable, by 20.4% for the cable on the base of steel, GFRP and CFRP; by 20.1% for the cable on the base of steel, Vectran and CFRP. Volumetric fractions of GFRP and Vectran were equal to 0.2. At the same time, increase of volumetric fraction of steel from 0.1 to 0.7 enables to increase the value of force, which can be taken up by the cable, by 1.63 times for the cable on the base of steel, GFRP and Vectran. Volumetric fraction of GFRP was equal to 0.2.

The using of the cable truss as a structure of support contour enables to decrease by 8 % the maximum vertical displacements of the cable net in the case, when the tension cables of the net are hybrid composite cables on the base of steel, GFRP and CFRP, but suspension and stressing cables of the net are made of steel.

REFERENCES

[1]   Beers, D.E. and Ramirez, J.E., "Vectran Fibers for Ropes and Cables", Proceedings of MTS Conference, Washington, 1990, pp. 662–670.

[2]   Bengtson, A., "Fatigue Tests with Carbon-Fiber-Reinforced Composite Cable as Nonmetallic Reinforcement in Concrete", Göteborg, 1994, pp. 1–14.

[3]   Berger, H., "Light Structures-Structures of Light: the Art and Engineering of Tensile Architecture", Birkhauser, Basel, 2002.

[4]   Blum, R., "Material Propertiesof Coated Fabrics for Textile Architecture", Proceedings of the symposium The design of Membrane and Light Weight Structures, Brussel, 2000, pp. 63–88.

[5]   Houtman, R., "There is no Material Like Membrane Material", Proceedings of the Tensinet Symposium Designing Tensile Architecture, Brussel, 2003, pp. 178–194.

[6]   Peters, S.T. "Handbook of Composites", London, 1998. pp. 758–777.

[7]   Costello, G.A., "Theory of Wire Rope, Second Edition", New York, Springer, 1997.

[8]   Kumar, K. and Cochran, Ir. I.E., "Closed form Analysis for Elastic Deformations of Multilayered Strands", Journal of Applied Mechanics, ASME, 1997, Vol. 54, pp. 898–903.

[9]   Serdjuks, D., Rocens, K., and Pakrastinsh, L., "Utilization of Composite Materials in Saddle-Shaped Cable Roof", Mechanics of Composite Materials, 2000, Vol. 36, No. 5, pp. 385–388.

[10]   Serdjuks, D., Rocens, K., "Hybrid Composite Cable Based on Steel and Carbon", Materials Science, 2000, Vol. 9, No. 1, pp. 27–30.

[11]   Serdjuks, D., Rocens, K. and Mitrofanov, V., "Behavior of Hybrid Composite Cable in Saddle-Shaped Roof", Scientific Proceedings of Riga Technical University, Architecture and Construction Science, 2002, Vol. 3, pp. 162–169.

[12]   Serdjuks, D., Rocens, K and Ozolinsh, R., "Influence of Diagonal Cables Strengthening by the Trusses on the Saddle-Shaped Roof Rigidity", Scientific Proceedings of Riga Technical University, Architecture and Construction Science, Vol. 6, pp. 210–218.

NUMERICAL ANALYSIS BY VIRTUAL TESTING REPLACING EXPERIMENTS WITH TENSION ROD SYSTEMS

Albrecht Gehring [1,*], Richard Goodman [2], Helmut Saal [3] and Chris Willett [4]

[1] *Engineering consultant, Lauer & Weiss GmbH, Höhenstraße 21, 70736 Fellbach, Germany*
[2] *Engineering design manager, Macalloy Limited, Caxton Way, Dinnington, S25 3QE, United Kingdom*
[3] *Professor, Versuchsanstalt für Stahl, Holz und Steine, Universität Karlsruhe (TH), Germany*
[4] *Sales director, Macalloy Limited, Caxton Way, Dinnington, S25 3QE, United Kingdom*
[*](Corresponding author: E-mail: albrecht.gehring@lauer-weiss.de)

ABSTRACT: The resistance of tension rod systems can be calculated according to design codes, e.g. Eurocode 3 or DIN 18800-1. Often the real load bearing capacity is not activated by the calculated resistance – which is due to a conservative approach of the analytical design methods. The real load bearing capacity of the whole system can be evaluated by a series of ultimate load tests. The results of these tests lead to technical approvals. This procedure takes a lot of time and is very cost intensive. Therefore some European building authorities are allowing virtual tests to reduce both costs and time. A general strategy for preparing and performing virtual tests of tension rod systems is presented in this paper. Special attention is paid to generate a clear numerical model with respect to possible failure modes. The application of this strategy is illustrated by an example of virtual tests which led to a technical approval in Germany.

Keywords: Tension rod system; finite-element analysis; virtual testing; failure criteria; static resistance

1.   INTRODUCTION

Modern sophisticated steel structures are unthinkable without the application of tension rod systems. They are applied as bracing for buildings or beams and in bridges. The first ever structure built with tension rod systems is shown on Figure 1. Commissioned as a distribution facility, the Renault Centre was designed to maximise internal flexibility. The repeated structural system makes use of tension rods, which support the roof structure. Stainless steel tension rods are used to support the bridge deck from a tubular steel arch or the flamboyant roof structure from large steel arches, see Figure 1 and Figure 2. Tension rods are used to support the roof trusses and skylights, see Figure 3. The roof of the Sazka arena shown on Figure 4 takes the shape of a spherical cap spanning 135m and with a rise of 9m. It is supported by a pre-stressed space beam tension rod structure. Other applications are described in Kathage et al. [1].
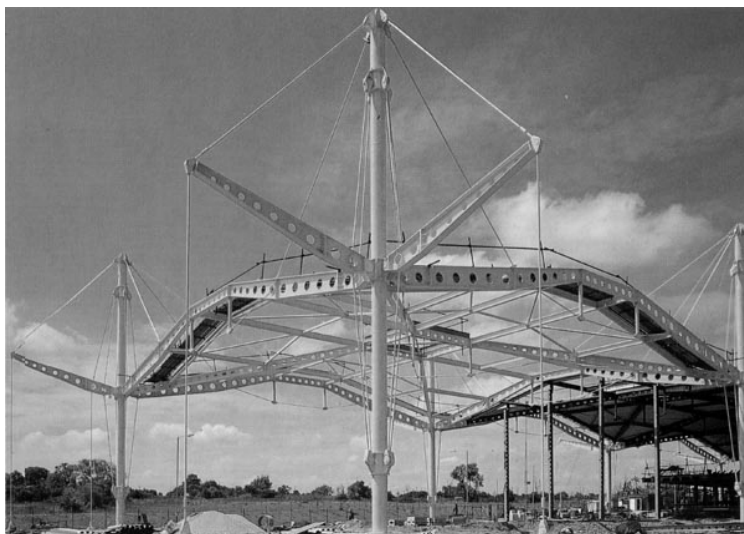
Figure 1. Renault Distribution Centre, Swindon, UK, 1983 (left)
Pedestrian Bridge, Tel Aviv, Israel, 2005 (right)
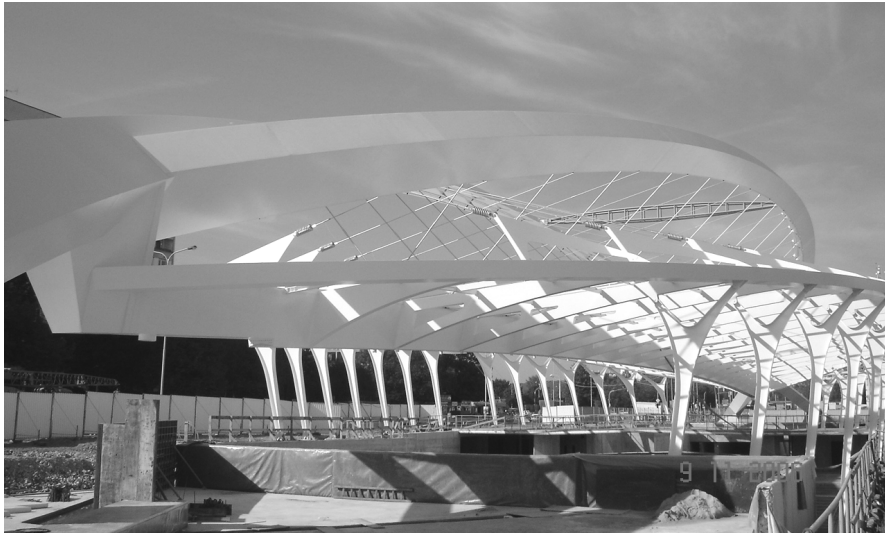
Figure 2. Metro station, Stritzkov, Prague, Czech Republic. 2005

Figure 3. Ports International Airport, Porto, Portugal. 2005

Figure 4. Sazka Arena, Prague, Czech Republic. 2004

Often conservative results are obtained by a calculation of the resistance of a tension rod system according to the European standards EN 1993-1-1 [2] and EN 1993-1-8 [3] or the German standard DIN 18800-1 [4], [5]. This leads to uneconomic building components. The actual load bearing capacity could be utilised by an assignment of a technical approval which is based on extensive tests. A Common Understanding of Assessment Procedure CUAP [6] regulates the test procedures and the number of tests in Europe. This procedure takes a lot of time and is cost intensive. Therefore some European building authorities [7], Breitschaft and Häusler [8], Kathage [9] are allowing virtual tests to reduce both costs and time. The strategy, performance and verification of virtual tests is exemplified below with a tension rod system. The results of the example, Saal and Gehring [10], led to an assignment of a technical approval [11] in Germany.

2.   COMPONENTS AND DESIGN METHODS

A tension rod system usually consists of several components, Figure 6. The fork end connectors are fabricated from steel by casting or forging. Usually high strength steel grades are utilised for the pins, Kathage et al. [1]. The tension rods are executed in steel grades up to S690. Couplers, turnbuckles and circular gusset plates complement standard tension rod systems. The tension rod is joint to the structure by a single bolted connection between a fork end connector and an end plate.
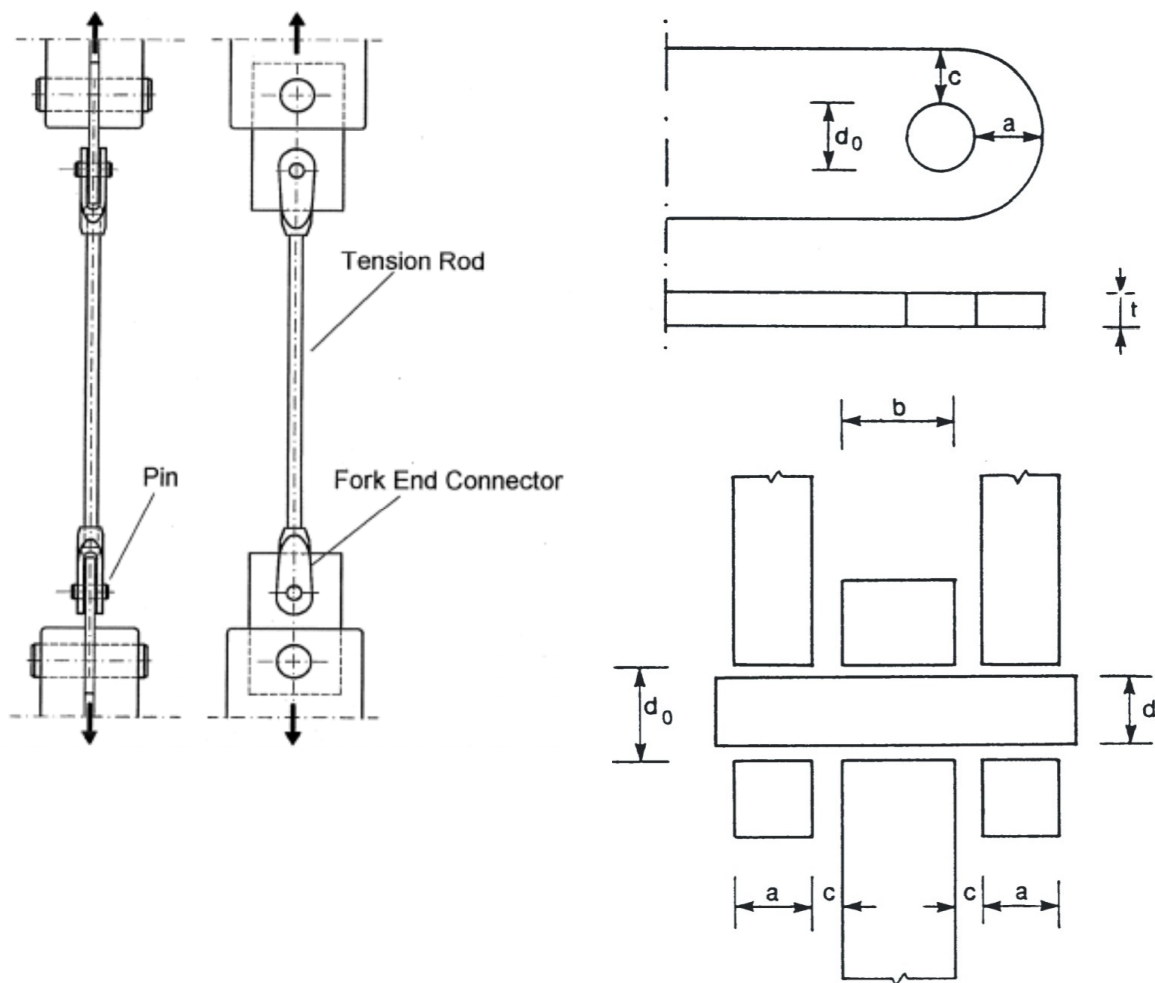
Figure 6. General Assembly of a Tension Rod System (left, from [6]) and Notation for Fork End Connector (right, top) and Pin (right, bottom), Both from [3]

The design of all components is usually performed according to Eurocode 3 [2, 3] or DIN 18800-1 [4, 5]. The resistance of the threaded connection of the tension rod to the fork end connector may be calculated according to VDI-Richtlinie 2230 [12] up to size M 100. The design methods are explained in detail in Kathage et al. [1].

With the notation of Eurocode 3 [2], [3] see Figure 6, the characteristic resistance $F_{fec,c}$ of a fork end connector is obtained according to German standards DIN 18000-1 [4], [5] from the formulae

$$F_{fec,c} = \min \begin{cases} F_{fec,1,c} = (a - 2/3 d_0) \, 2 \, t \, f_{y,fec} \, 2 \\ F_{fec,2,c} = (c - 1/3 d_0) \, 2 \, t \, f_{y,fec} \, 2 \\ F_{fec,3,c} = t \, d \, 1{,}5 \, f_{y,fec} \, 2 \end{cases} \tag{1}$$

and the characteristic resistance $F_{pin,c}$ of the pin is obtained from

$$F_{pin,c} = \min \begin{cases} F_{pin,1,c} = 0{,}6 \, A \, f_{up} \, 2 \\ F_{pin,2,c} = \dfrac{8 \, f_{yp} \, W_{el}}{1{,}25 \, (b + 4 \, c + 2 \, a)} \end{cases} \tag{2}$$

where W_{el} is the elastic section modulus of the pin. In addition the interaction of bending moment and shear forces has to be examined.

The characteristic resistance $F_{tr,c}$ of the tension rod is obtained from German standards DIN 18000-1 [4], [5] as

$$F_{tr,c} = \min \begin{cases} F_{tr,1,c} = \dfrac{f_{yb}}{1{,}1} \, A \\ F_{tr,2,c} = \dfrac{f_{ub}}{1{,}25} \, A_s \end{cases} \tag{3}$$

which is slightly different from European standards [2, 3]. In Eq. 3 A is the gross cross section and A_s is the tensile stress area of the tension rod.

Usually the resistance of the whole system is limited by the load bearing capacity of the pin according to Eq. 2. This is due to a conservative approach, which does not take into account the real load transfer, Kathage et al. [1]. A comparison of the assumed uniform distribution of the reactions between pin and fork end and their real distribution is given in Saal and Bechtold [13].

For safety purposes it is desirable that the load bearing capacity of a tension rod system is governed by that of the tension member. In this case it has to be guaranteed that the resistance of fork end connector, pin, coupler etc. exceeds the resistance of the tension member. This can be demonstrated by conservative formulae, e.g. Eq. 1 and Eq. 2, or by tests. This latter procedure is the basis for technical approvals for individual tension rod systems where the design is reduced to the application of Eq. 3, Kathage et al. [1].

3.   EXECUTION OF VIRTUAL TESTS

Virtual tests will only lead to safe results if they are based on a profound knowledge of the load transfer and the possible failure modes. This demands substantial experience with experimental and numerical analysis of the object. This has to be kept in mind for safety reasons when virtual tests are performed.

In general, the performance of virtual tests can be divided in the following sub-steps:

- Determination of characteristic resistances of all components according to European [2, 3] or German [4, 5, 12] standards.

- Estimation of results in order to simplify the numerical model such that only relevant failure modes are included

- Generation of a numerical model: geometry, material laws, contact conditions

- Theoretical verification of the model: proof of plausibility of the failure modes (shear failure, bending failure of pin, etc.) and derivation of failure criteria.

- Experimental verification of the model and the failure criteria: comparison of failure loads obtained numerically and experimentally.

- Performance of virtual tests with the verified model. The failure loads are obtained by application of the derived failure criteria.

A mechanically reasonable model is obtained by application of the first two steps. Economic design rules should be applied if available, e.g. VDI-Richtlinie [12]. The numerical model can be simplified with this, because these failure modes must not be analysed in the virtual tests. Thus, the attention can be focused on the interesting load transfer mechanisms and failure modes. Unlike Kathage et al. [1], we recommend to generate separate numerical sub-models for analysis of the different failure modes. This separation allows a target-oriented fine mesh for the numerical model and a clear interpretation of the results. The failure modes are assessed by the application of mechanical considerations and present experiences. The ultimate failure loads are determined with well defined failure criteria. The quality of the failure criteria has to be verified experimentally. Then, all necessary virtual tests can be performed with the verified numerical model. If the results obtained by the virtual tests physically make no sense, experimental investigations are unavoidable for safety reasons.

4.   EXAMPLE

4.1   Components and Limitations

All steps of the virtual tests are explained by an example, Saal and Gehring [12]. In this case a German technical approval [11] for a tension rod system was extended for sizes M85, M90 and M100 by the results of virtual tests. This tension rod system is shown in Figure 7 schematically. The relevant dimensions are listed in Table 1.

The characteristic resistances calculated with Eq. 1 to Eq. 3 are given in Table 4. The characteristic resistance $F_{VDI,c}$ of the threaded connection between fork end connector and tension rod given in Table 4 was calculated according to VDI-Richtlinie 2230 [13]. This was confirmed in many previous tests with connections of that type as a safe and economic approach. Because of this the thread need not be modelled.

Table 1. Dimensions of the Tension rod System

	M20	M30	M76	M85	M90	M100
	mm	mm	Mm	mm	mm	Mm
d_{sp}	17	25	67	77	82	92
A	122	178	410	459	489	555
B	51	79	199	236	248	289
C	29	43	108	121	129	143
D	15	22	70	70	80	85
E	24	32	78	87	92	102
G	19	26	76	79	87	92
H	37	48	148	153	169	174
K	21	31	78	91.5	96.5	111.5
N	20	30	76	90	93	108
T	9	11	36	37	41	41
V	33	52	131	153	162	188
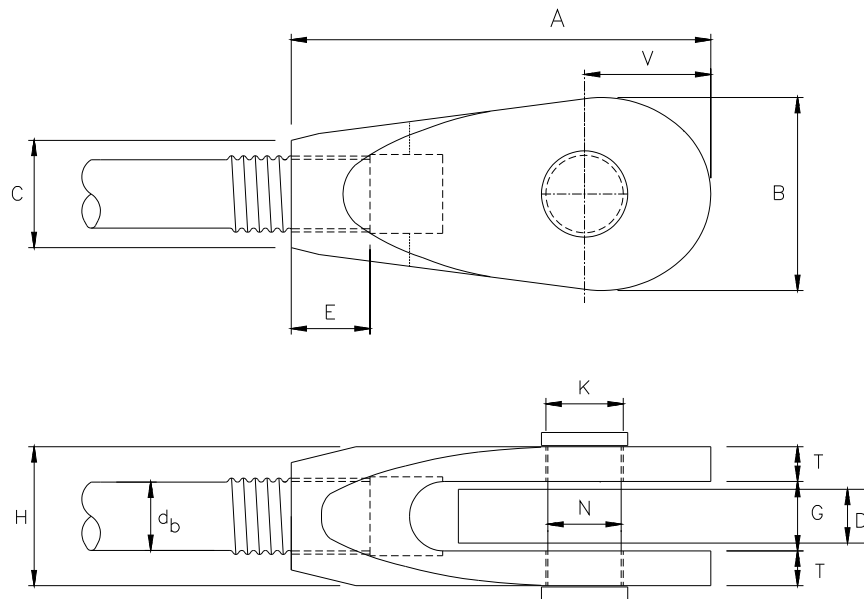
Figure 7. Schematic Drawing of Tension rod System, From [11]

4.2   Description of Numerical Model

The virtual tests are performed with the commercial Finite-Element package ABAQUS/Standard [14]. The single components fork end connector, pin and end plate are modelled. Due to the double symmetry, the finite-element model represents a quarter of the structure. The end of the fork end connector is modelled with parallel surfaces instead of the tapering. This has no effect on the load bearing capacity for which only the pin and the neighbouring area of the fork end is relevant. The end plate is represented by rigid elements for the same reason. A contact without friction is defined between fork end connector and pin. This assumption is based on test results, Saal and Gehring [10].

The end plate is defined as fixed support. The load is applied by a translation of the threaded area in 2-direction, see Figure 8. The fork end connector and the pin are meshed with continuum element type C3D8R, Abaqus [15]. The analysis is performed with the finite-element mesh shown in Figure 8.
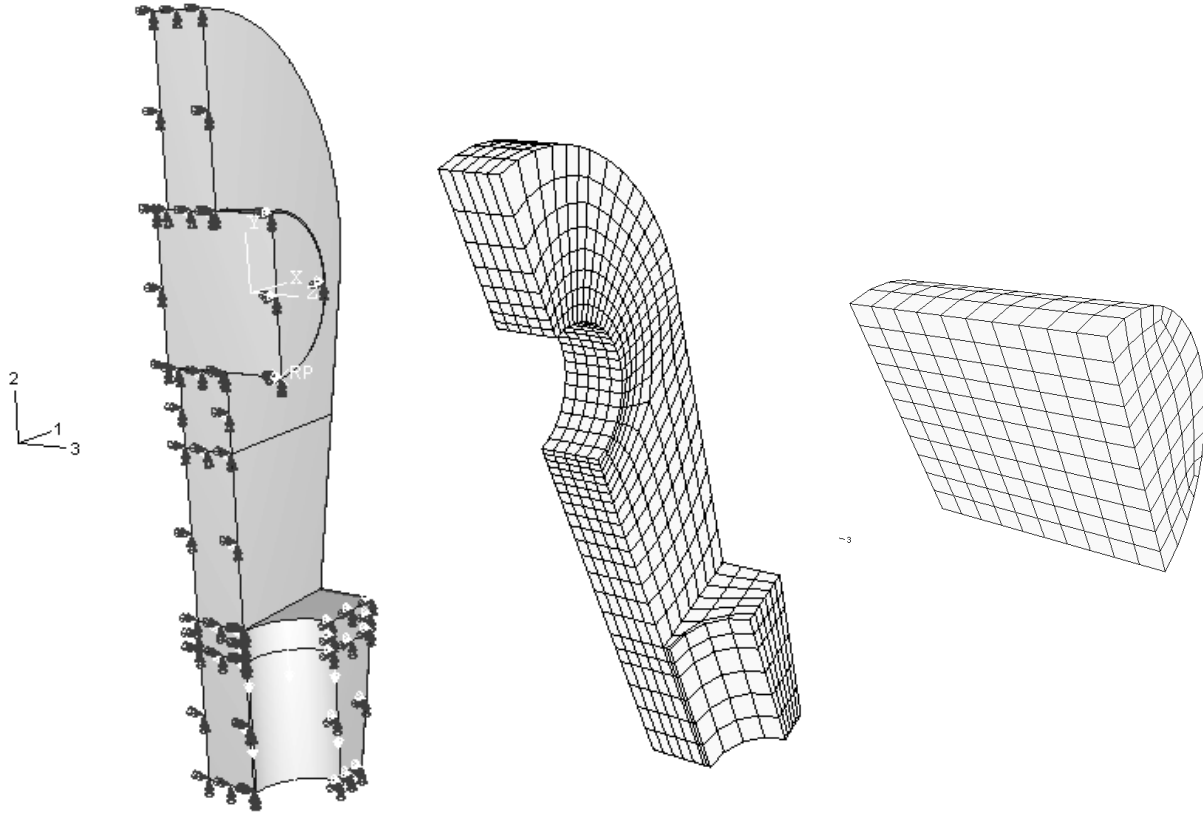
Figure 8. Boundary Conditions, Meshed Fork end Connector and Pin

The material behaviour is described by a bi-linear isotropic material law for both the fork end connector and the pin. Plastic deformations are controlled by the von-Mises yield criterion with an associated flow rule. The material is characterised by the yield strength f_y and the tensile strength f_u. The nominal stresses σ and strains ε are transformed into true stresses σ_{true} and true strains ε_{true} for all calculations with

$$\sigma_{true} = \sigma\,(1+\varepsilon) \tag{4}$$

$$\varepsilon_{true} = \ln\,(1+\varepsilon) \tag{5}$$

This gives a realistic deformation response for the ultimate failure load which is determined by the tensile strength.

The nominal material properties are taken from a technical approval [11]. The material parameters used for the analyses are given in Table 2.

Table 2. Material Parameters

	Elastic constants *		Point A **		Point B ***	
	E	ν	σ_{true}	ε_{true}	σ_{true}	ε_{true}
	GPa	-	MPa	-	MPa	-
Fork end connector	210	0.3	335	0.00	660	0.095
Pin	210	0.3	640	0.00	854	0.065

* Young's modulus E and Poisson's ratio ν
** Stress and plastic strain at yield point
*** Stress and plastic strain at failure

4.3 Derivation of a Failure Criteria

A failure criterion is derived from the design rules for the net section of tension members. According to Anpassungsrichtlinie [5] the ultimate limit state is controlled by the tensile strength without limitation of plastic strains. However, for the virtual ultimate failure load $F_{FEM,u}$ of the fork end connector this criterion is extended by a limitation of the plastic strain ε_{pl} to the ultimate value ε_{true}. Thus

$$F_{FEM,u} = F_{FEM}(\varepsilon_{pl})\tag{6}$$

where $\varepsilon_{pl} = \max(\varepsilon_{EPPQ}, \varepsilon_{PE22}) < \varepsilon_{true}(A_g)$ and A_g is the uniform elongation.

The plastic strain ε_{pl} is obtained from the numerical calculations as the maximum of equivalent plastic strain ε_{EPPQ} and the plastic strain ε_{PE22} in direction of loading. The equivalent plastic strain accounts for the triaxial stress state. Tension stresses close to the hole are represented by the plastic strain in the direction of loading. The ultimate failure load is attained, when the plastic strain ε_{pl} equals $\varepsilon_{true}(A_g)$. This means, the tensile strength is reached locally in contrast to the design rules for the net section of tension members.

In this example the pin is not controlling the ultimate failure load of the tension rod system because the tensile strength of the fork end connector is much less than the yield strength of the pin.

4.4 Experimental Verification

The finite-element model is verified with the results of existing ultimate load tests obtained for different system sizes. The comparative calculations are performed with the measured geometries and material data from the tests. The ultimate failure loads of the virtual tests are determined by application of the failure criterion Eq. 6. The failure loads determined numerically with this criterion are compared to the experimental results in Table 3.

A fork end connector size M 76 in the ultimate limit state according to Eq. 6 is shown in Figure 9 with the distribution of the equivalent plastic strain and plastic strain in direction of loading. An example of a broken fork end connector is shown in Figure 10. The collapse was initiated by a tensile failure of one plate of the fork end connector. The following dynamic process leads to the visible bending of the other plate. Plastic deformations did not occur in the pin and the end plate.

Table 3. Verification of the Numerical Model by
Comparison of Numerical and Experimental Failure Loads

Size	Virtual test $F_{FEM,u}$	Real test F_{Exp}	Difference
	kN	kN	%
M 20	243	272	-10.1
M 30	506	505	+0.2
M 76	3778	3816	-1.0
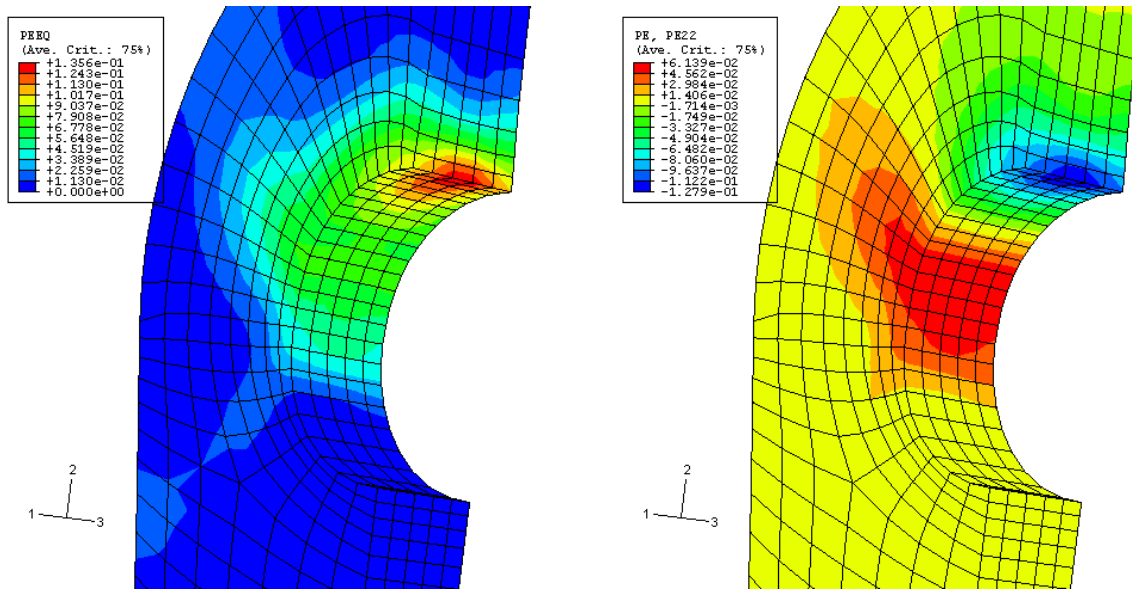
Figure 9. Equivalent Plastic Strain (Top) and Plastic Strain in Direction of Loading (Bottom) at
Ultimate Limit State According to Failure Criteria (6)

Figure 10. Broken Fork End Connecter after Ultimate Load Test
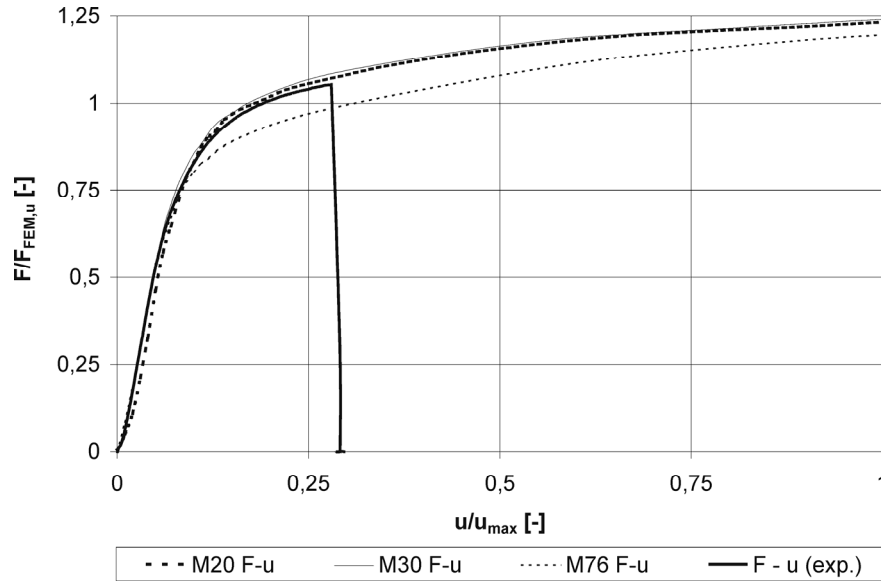
Figure 11. Normalized Load-Displacement-Curves

The normalized load-displacement-curves from the calculations are shown in Figure 11. The displacements are normalized with respect to a maximum translation specified as one fifth of the hole diameter K and the forces are normalized with respect to the ultimate failure load $F_{FEM,u}$. Figure 11 includes a load-displacement-curve obtained experimentally. All of the four curves are in good agreement. The results of the verification show, that

- the load bearing capacity of the tension rod system is modelled physically correct

- the application of the failure criterion leads to a safe and economic estimation of the ultimate failure load

4.5   Results and Comparison of Results

The ultimate failure load of the fork end connectors with pin is calculated with the nominal material properties transformed by Eq. 4 and Eq. 5. It is determined for each size with the failure criterion Eq. 6. Additional calculations are performed with sizes M20, M36 and M76. The ultimate failure loads $F_{FEM,u}$ obtained from the virtual tests and the resistances calculated according to Eq. 1 to Eq. 3 are listed in Table 4 as well as the characteristic resistance $F_{VDI,c}$ of the threaded connection according to VDI-Richtlinie [12].

The load bearing capacity F_{trsys} of the fork end connector with pin is obtained as minimum from $F_{VDI,c}$ and $F_{FEM,u}$. All possible failure modes are included through this.

The results should show that the tension rod governs the load bearing capacity of the system in design. Therefore the ratio η, which is defined as

$$\eta = \frac{\min(F_{FEM,u}, F_{VDI,c})}{\dfrac{F_{tr,c}}{1,1}} \tag{7}$$

has to be greater than the safety factor γ_M specified in DIN 18800-1 [4] or CUAP [6] for this application. The safety factor $\gamma_M = 1.1$, CUAP [6] for tension members is included in the denominator of Eq. 7. The ratios η from the example are given in Table 4. The safety factor γ_M specified in CUAP [6] is $\gamma_M = 1.25$ and in DIN 18800-1 [4] is $\gamma_M = 1.25 \cdot 1.1 = 1.375$. The comparison of η and γ_M shows, that the fork end connectors with sizes M 85, M 90 and M 100 are not determining the load bearing capacity of the tension rod system and thus are not relevant for design.

Table 4. Results of Calculations According to Formulae (1) to (3),
VDI-Richtlinie and Results of Virtual Tests

Size		M20	M30	M76	M85	M90	M100
$F_{fce,1,c}$	kN	104	251	2042	2380	2939	3406
$F_{fce,2,c}$	kN	95	214	1745	2132	2555	2994
$F_{fce,3,c}$	kN	161	332	2750	3347	3832	4450
$F_{fce,c}$	kN	95	214	1745	2132	2555	2994
$F_{pin,1,c}$	kN	302	679	4355	6107	6521	8794
$F_{pin,2,c}$	kN	82	209	1146	1810	1838	2799
$F_{pin,c}$	kN	82	209	1146	1810	1838	2799
$F_{tr,1,c}$	kN	124	265	1736	2252	2538	3154
$F_{tr,2,c}$	kN	111	242	1723	2281	2593	3269
$F_{tr,c}$	kN	111	242	1723	2252	2538	3154
$F_{VDI,c}$	kN	204	429	2846	3555	4031	4947
$F_{FEM,u}$	kN	216	388	3366	4230	5027	5761
F_{trsys}	kN	204	388	2846	3555	4031	4947
η	-	2,02	1,77	1,82	1,74	1,75	1,73

5.   SUMMARY

The design methods for tension rod systems are presented and discussed. It is shown, that the common design procedures give uneconomic results. Therefore it is advisable to determine the real load bearing capacity by tests. This requires a technical approval. The procedure of testing is time and cost intensive. Costs and duration can be decreased by the application of virtual tests. A general strategy is presented for planning and performing virtual tests. The procedure is divided into several steps. With respect to a physical reasonable and preferably simple numerical model, a thorough consideration of the structure is absolutely necessary. We recommend to divide the component or structure into sub models for the analysis of different failure modes. This allows a target-oriented fine mesh of the individual numerical model for each failure mode and a clear interpretation of the results. All steps of the strategy are explained by the example of an extension of an existing technical approval for a tension rod system.

It has to be kept in mind that virtual tests will only lead to safe results if they are based on a profound knowledge of the load transfer and the possible failure modes. This demands substantial experience with experimental and numerical analysis of the object.

REFERENCES

[1]   Kathage, K., Ruf, D.C. and Ummenhofer, T., "Zugstäbe und ihre Anschlüsse", In: Kuhlmann, U. (Editor), Stahlbau-Kalender 2005, Verlag Ernst & Sohn, 2006, pp. 725-784.

[2]   EN 1993-1-1:2005-07: Eurocode 3: Design of Steel Structures – Part 1-1: General Rules and Rules for Buildings.

[3]   EN 1993-1-8:2005-07: Eurocode 3: Design of Steel Structures – Part 1-8: Design of Joints.

[4]   DIN 18800-1:1990-11: Stahlbauten – Bemessung und Konstruktion.

[5]   Anpassungsrichtlinie Stahlbau Fassung Dezember 1998, inkl. Änderungen und Ergänzungen Ausgabe Dezember 2001, DIBt Mitteilungen 2002. Sonderheft 11.

[6]   CUAP (Common Understanding of Assessment Procedure), "Tension Rod System", Deutsches Institut für Bautechnik, Berlin, 2003.

[7]   "Gemeinsame Erklärung des CSTB und DIBt zur technischen Bewertung von Bauprodukten auf Grundlage virtueller Versuche mit dem Ziel der Kostenreduzierung im Bauwesen", DIBt Mitteilungen, 2004, Vol. 35, No. 5, pp. 146-147.

[8]   Breitschaft, G. and Häusler, V., "Verwendung von rechnerischen Nachweisen bei Erteilung von Zulassungen", DIBt Mitteilungen, 2004, Vol. 35, No. 5, pp. 147-149.

[9]   Kathage, K., "Finite-Elemente-Berechnungen als Grundlage zur Erteilung von Zulassungen für Zugstabsysteme", DIBt Mitteilungen, 2004, Vol. 35, No. 5, pp. 149-151.

[10]   Saal, H. and Gehring, A., Gutachten Nr. 044074: Änderung und Ergänzung der bauaufsichtlichen Zulassung Z-14.4-427", Versuchsanstalt für Stahl, Holz und Steine, Universität Karlsruhe (TH), 2004, Unpublished.

[11]   Allgemeine bauaufsichtliche Zulassung Z-14.4-427, "Zugstabsystem MACALLOY 460", Deutsches Institut für Bautechnik, Berlin, 2004.

[12]   VDI-Richtlinie 2230 Blatt 1:2003-02: Systematische Berechnung hochbeanspruchter Schraubenverbindungen - Zylindrische Einschraubenverbindungen.

[13]   Saal, H and Bechtold, M., "Zugstäbe und Seile. Vielfalt der Möglichkeiten? Gestaltung und Nachweis", In: Proceeding of 25th Stahlbauseminar Neu-Ulm, Biberach, 2003.

[14]   ABAQUS/Standard. Version 6.4.1. Copyright 2003. ABAQUS, Inc.

[15]   ABAQUS Documentation – Version 6.4. Copyright 2003. ABAQUS, Inc.

ASSESSMENT OF CYCLIC DUCTILE ENDURANCE OF STRUCTURAL STEEL MEMBERS

C.W.K. Hyland[1],*, W.G. Ferguson[2] and J.W. Butterworth[3]

[1]Secretary Manager, Steel Construction New Zealand Inc., PO Box 76403, Manukau City 2241, New Zealand
Phone: +64-9-262-6680 Fax: +64-9-263-5638
*(Corresponding author: E-mail: clark.hyland@scnz.org)
[2]Professor of Chemical & Materials Engineering, University of Auckland, Private Bag 92019,
Auckland 1061, New Zealand
Phone: +64-9-373-7599 Ext 88133 Fax: +64-9-373-7463
[3]Associate Professor of Civil and Environmental Engineering, University of Auckland, Private Bag 92019,
Auckland 1061, New Zealand
Phone: +64-9-373-7599 Ext 88154 Fax: +64-9-373-7462

ABSTRACT: This paper describes a new method using Crack Tip Opening Displacement (CTOD) testing in conjunction with a relatively simple elasto-plastic finite element analysis to assess the likelihood of fast running or slow stable fracture during monotonic and cyclic loading of steel members. The similitude relationship between monotonic and cyclic displacement ductility is then used to assess cyclic endurance of the steel member. The fracture toughness of steel defined by the critical specific work of fracture R_c of the steel is determined from CTOD specimens making allowance for remote plastic flow. A finite element model is used to assess elastic compliance of a cracked bar with varying lengths of cracks as well as to assess the inelastic displacement of the bar at calculated cracking loads. Failure limit state surfaces comprising plastic hinging, plastic over-strength and cracking limits are plotted in 3-D surfaces to identify the characteristics of how fracture behaviour changes dramatically as the strain hardening and crack length increases.

Keywords: Specific work of fracture, fracture toughness, structural ductility, cyclic endurance, seismic, finite element analysis, CTOD

1.   INTRODUCTION

This paper describes a cyclic plastic endurance assessment method developed from the findings of an experimental and theoretical study by Hyland, Ferguson and Butterworth [1]. The study was undertaken to investigate the development of running fracture in large structural steel assemblies in building structures subjected to earthquake loading. A specific work of fracture approach was found to be effective in conjunction with elasto-plastic finite element modelling of members in assessing the mode of fracture and the expected endurance of members under cyclic plastic loading.

The determination of the specific work of fracture properties based on the use of small scale side grooved CTOD specimens is first described. The effect of remote plastic flow, strain hardening and aging is considered in determining the critical specific work of fracture value R_c. The assessment of the governing fracture condition is made by evaluating the plastic hinge, strain hardened and running fracture limit states plotted as surfaces to determine which governs as the material strain hardens under cyclic loading.

The similitude relationship is then used to assess the expected endurance of an example simply supported beam under plastic cyclic loads of constant amplitude. The approach is extended into a variable amplitude case equivalent to an ATC-24 loading regime by use of a Palmgren-Miner summation method.

2.   DETERMINATION OF FRACTURE TOUGHNESS BASED ON CRITICAL SPECIFIC WORK OF FRACTURE R_C

2.1   Overview

Using the data for a side-grooved CTOD sample of steel, the specific work of fracture may be determined over a portion of the load-displacement X-u plot shown in Figure 1.   If the applied strain energy in the crack tip process zone exceeds R at any point then the crack will propagate. Stable crack growth typically occurs for ductile steels throughout the testing indicated by a rising R curve.   If the applied strain energy is subsequently reduced then the crack will stop growing. However a limiting upper bound or critical value R_c can eventually be reached after which the crack will continue propagating or running after removal of the applied loading.

Taking the load, X, near the limiting value and the corresponding load line displacement the work of fracture in the crack tip process zone at the load may be determined by comparison with an adjacent load and displacement for an increased crack length as shown in Figure 2.   The fatigue crack length is measured in conjunction with the net width at the side-grooved crack front to allow a change in crack area to be assessed.

From the Direct Current Potential Drop (DCPD) output the crack length at each load can be determined using a pre-calibrated crack length curve.   The elastic component of displacement may then be determined at each load to assess the compliance of the specimen at each crack length. From BS 7446-1:1997 Eq. 11 the elastic displacement of a 3 point bend CTOD specimen with side-grooves is :

$$u_{el} = \frac{F(1-v^2)}{EB_{eff}}\left(\frac{S}{W-a}\right)^2 \left\{1.193 - 1.980\left(\frac{a}{W}\right) + 4.478\left(\frac{a}{W}\right)^2 - 4.443\left(\frac{a}{W}\right)^3 + 1.739\left(\frac{a}{W}\right)^4\right\} \qquad (1)$$

and the effective width of the specimen is given as

$$B_{eff} = B - \left(\frac{(B-B_N)^2}{B}\right) \qquad (2)$$

Therefore plastic displacement after unloading from each load point is the measured displacement minus the elastic component.   The total work done in the specimen as the crack advances is the area within the curve LMNP of Figure 1.

The specific work of fracture in the crack process zone as the crack advances is the area within the curve LQP of Figure 2. If for elastic brittle fracture to occur the remote plastic flow would be zero and the radial elastic compliance lines would converge to the same point.   So the approach taken here is to say that there is a component of crack tip fracture that occurs whether in a field of remote plastic flow or not.   The magnitude of this component can be identified by converging the change in elastic compliance back to the point of origin of the elastic compliance curve prior to the change of crack length being investigated.   To make the convergence however the new elastic compliance curve must be displaced back by the amount of the net plastic displacement developed in increasing the crack length.

The work done in plastic flow in side-grooved CTOD specimens of 300Plus steel conforming to G300 AS3679 constructional steel, tested in this study, can be as much as 33 times greater than the specific work of fracture.   This shows how significant the remote plastic flow is on the energy balance in these samples and underlines the importance of isolating the remote plastic flow components from any assessment of fracture toughness gained from small sample testing.   Care is also required when applying small scale test results to large scale situations.

A comparison of the calculated value of R_c=37.3 kJ/m^2 obtained from the CTOD specimen in this study shown in Figure 1 and Figure 2 with those published by Atkins and Mai [2] indicates that this is within the range for carbon steels.   A medium carbon steel is listed with R=14 kJ/m^2, a high strength alloy having R=45 kJ/m^2 listed.
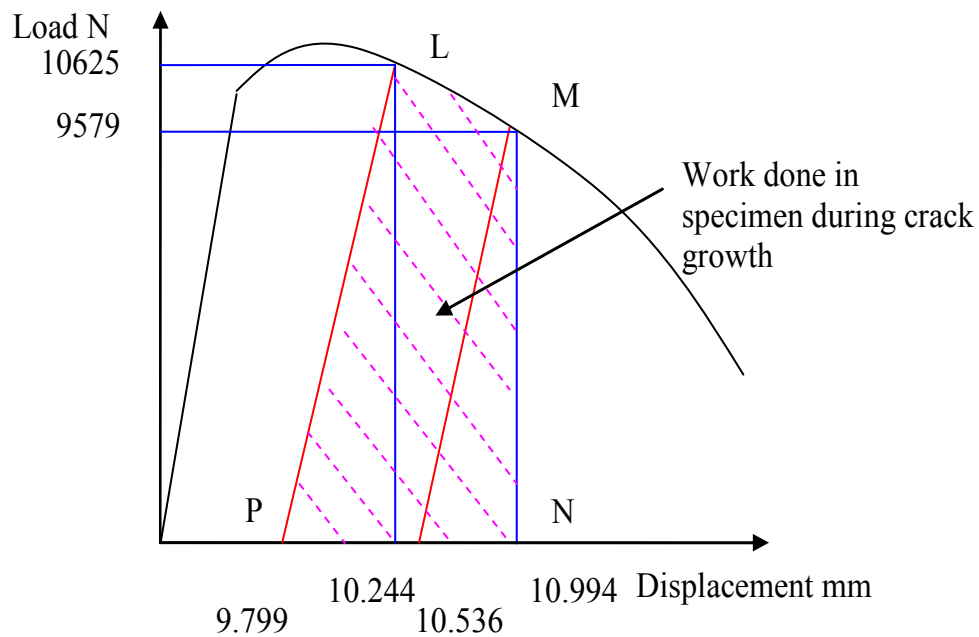
Figure 1. Total Work Done During Crack Growth in the Presence of Remote Plastic Flow
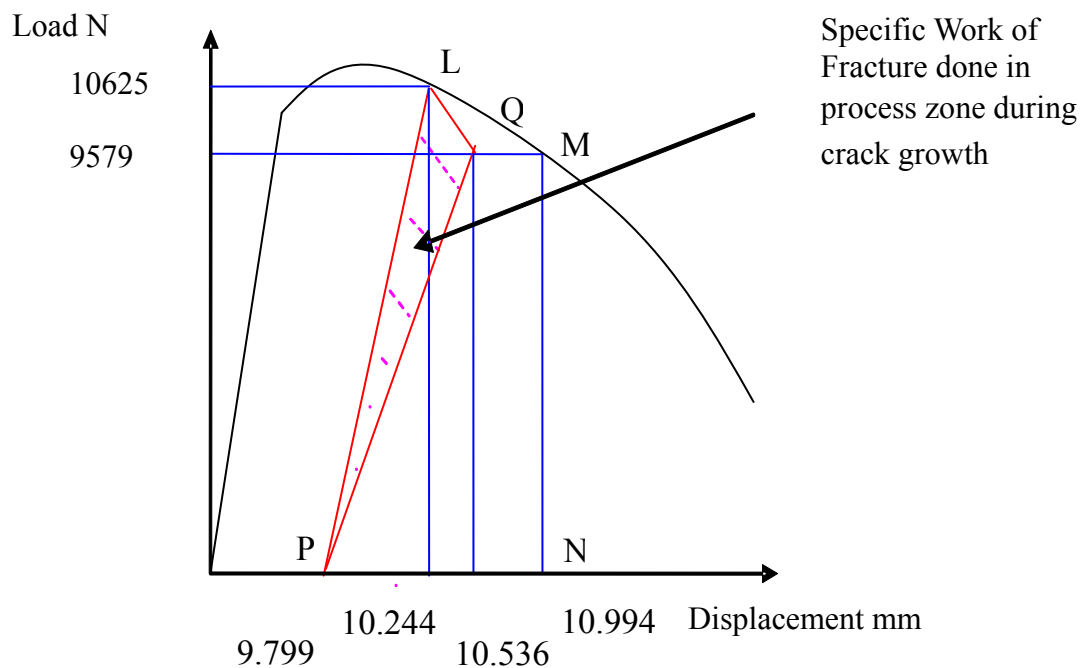
Figure 2. Specific Work of Fracture in Process Zone

The method used for determining R_c can be applied to data collected from CTOD testing when DCPD measurement of crack area growth has been used.   This was done in tests undertaken as part of this study. Incremental specific work of fracture calculations can be made for every recorded increment of crack area growth.   Curves developed in this way are shown for each pre-strained steel, combined into a single summary graph in Figure 3.

2.2   Effect of Strain Hardening and Aging on the R Curve

The plots of R versus crack area reveal a number of interesting features of toughness variation with strain hardening and aging. The first observation is that no matter the level of strain hardening all the samples of a particular steel eventually develop R curves that approach a reasonably consistent upper bound value of R_c. The main effect of strain hardening appears to be that of 'tightening' the R curve, so that less crack development is required to develop the critical R_c value. This is highlighted in the stylised representation of specific work of fracture versus crack area shown in Figure 5. The biggest change in the R curves is seen between that of the as-received steel and the 4.9% pre-strained steel.   A smaller sharpening of the curve occurs between the 4.9% and 9.8% pre-strained steels. A plateau value of 38 kJ/m^2 is indicated by all the samples if they avoid development of brittle fracture. The plateau value provides a useful upper bound for constructional steel assessment purposes.

The running fracture behaviour of the 9.8% and 17.7% pre-strained specimens at 10 ^{o}C and 20 ^{o}C indicates that the additional effect of strain aging and temperature has elevated the initiation point above the R_c value so that any crack development will result in fast running fracture.

Specific Work of Fracture R vs Normalised Crack Length CTOD 0% Pre-strain 300+ & M
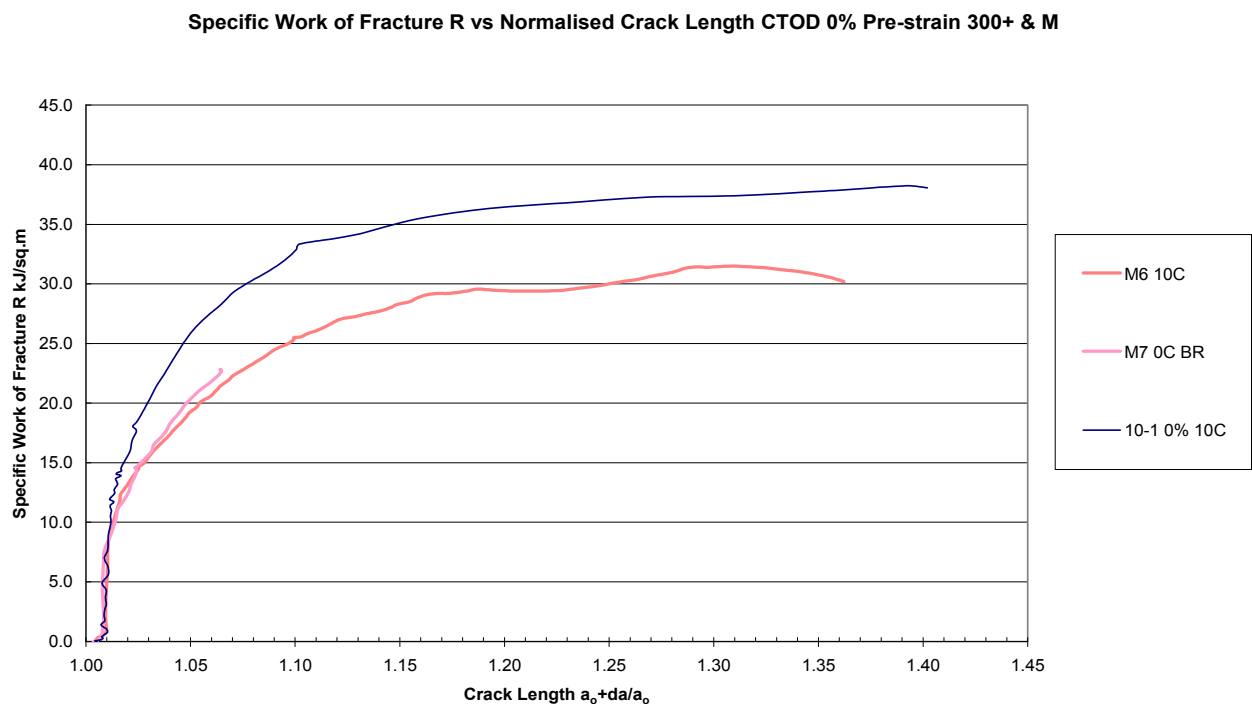
Figure 3. Specific Work of Fracture R vs Crack Length for
Unknown M Steel Compared to 300+ As-Received

2.3 Summary R Curves of Another Steel

CTOD test results M6 and M7 were for a steel with similar yield strength to the 300Plus steel, but not traceable to a particular grade or manufacturer. A plateau value of 30 kJ/m^2 is indicated by M6, though M7 failed with running fracture at 22 kJ/m^2. When compared to the 300Plus steel there is clearly a significant drop in toughness (Figure 4). However the constructional steel characteristic of a soft curving R similar to that of the as-received 300Plus steel is still evident.

Specific Work of Fracture R vs Normalised Crack Length 0%-17.7% Pre-strain
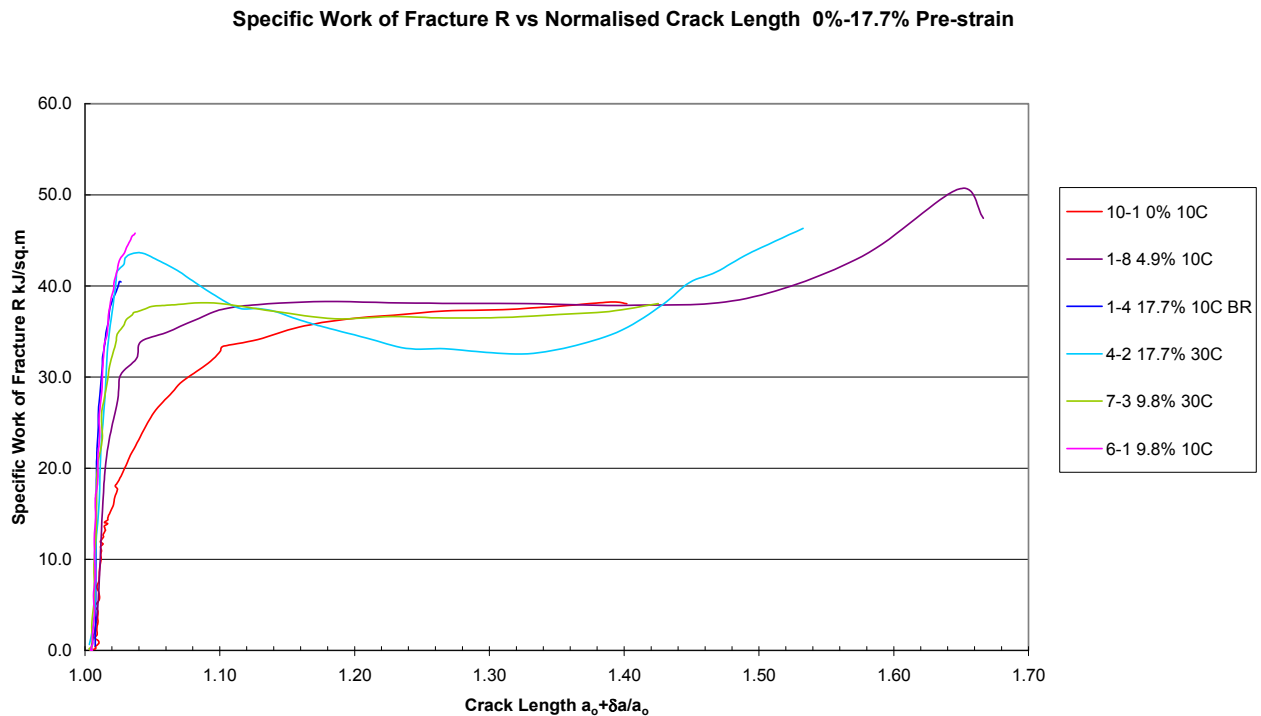
Figure 4. Specific Work of Fracture R vs Crack Length Summary for 300+ Steel
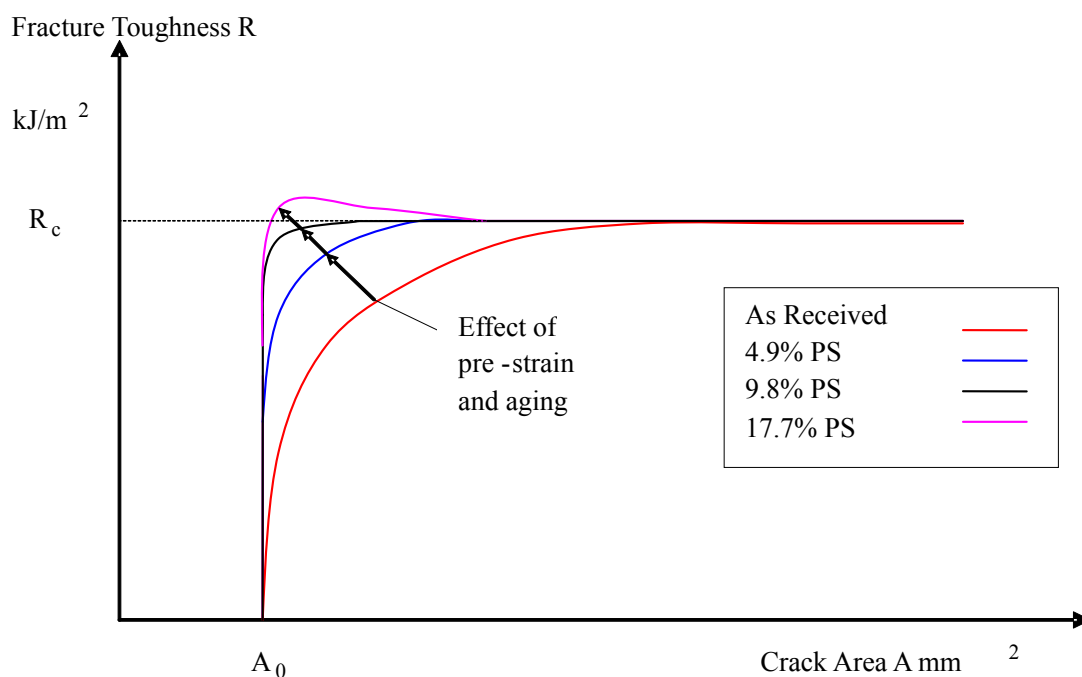
Figure 5. Stylised Specific Work of Fracture vs Crack Area,
Showing the Effect of Pre-Strain and Aging

2.4   Equivalent K_r Values

An equivalent elastic stress intensity at fracture can be derived from the R_c values of 38 kJ/m^2 for the 300Plus steel and 30 kJ/m^2 for the M series steel, by considering plane strain conditions to have been present in the CTOD samples as evidenced by the square fracture behaviour.

$$K_{Rc}^2 = E^* R_c \tag{4}$$

$$K_{Rc} = \sqrt{\frac{ER_c}{1-v^2}} = \sqrt{\frac{210 \times 10^3 \times 38 \times 10^{-3}}{1 - 0.3^2}} = 93.6 \quad MPa\sqrt{m}$$

for 300Plus steel samples

$$K_{Rc} = \sqrt{\frac{210 \times 10^3 \times 30 \times 10^{-3}}{1 - 0.3^2}} = 83.2 \quad MPa\sqrt{m}$$

for the unknown M series steel.

These values are well within the range for K_{Ic} values identified for constructional steels, adding to the confidence that this approach is valid. Such a value is particularly useful in allowing an upper bound approach to be applied to normal structural analyses. The peak strain hardened stress in a section may be used to identify whether the peak equivalent elastic stress intensity will be exceeded during the course of a load cycle irrespective of whether plastic flow is present or not.

3.   SUMMARY OF FINDINGS WITH RESPECT TO SPECIFIC WORK OF FRACTURE DERIVED R CURVES

Realistic values of fracture toughness have been derived using the specific work of fracture approach. These correspond well to published values of R and K_{Ic} found for constructional steels. The method is able to distinguish between one steel and another as evidenced by the differing values for the 300Plus steel and M series steels tested.

Where the rate of change of the applied crack tip strain energy G is greater than the change in the crack growth resistance R, unstable crack propagation will occur. The effect of pre-strain is to sharpen the curvature of the R curve such that less crack growth is required before a critical R_c value is reached at which the crack will propagate. When R_c is reached and significant remote plastic flow is available then stable crack propagation will result as the remote plastic flow will absorb the strain energy released by crack propagation. When R_c is reached and the energy balance in the specimen is dominated by elastic strain energy then fast unstable running fracture is expected to occur.

With cyclic loading the steel is being put through elastic and plastic strain hardening cycles so the energy balance within the steel at a particular stress state is dependent on its strain history. For example when reloading up to a strain hardened stress after an unloading phase, unstable running fracture will result if the critical R_c value is reached and no plastic flow is available to dissipate the release of strain energy upon crack propagation.

The effect of strain aging may be mainly limited to steel that has been significantly strain hardened such that the strain aged ultimate tensile strength is elevated above the as-received ultimate tensile stress.   The effect is that it will be almost impossible for the steel to develop remote plastic flow should R_c be reached as any plastic deformation would have to be localised into necking which has a reduced energy state compared to strain hardening plastic flow.

It is therefore productive to investigate the combined effect of deformation behaviour with strain hardened material property curves and R on specimens with varying crack areas.   The deformation plasticity effects are considered to be linked by the common energy balance requirement.

Geometrical size effects need to be considered when applying the R_c values derived from small scale specimens to large scale structures as while the material properties will be the same if the same material is used, the energy balance may be significantly different.   Potentially, more elastic strain energy may be available relative to remote plastic deformation in a larger specimen than in a smaller one.   Such effects may be identified by elasto-plastic modelling in appropriate FEA software.

4.   EXAMPLE ASSESSMENT OF MONOTONIC FRACTURE LIMIT STATES IN A STEEL BAR

4.1   Overview

In order to investigate the combined effects of deformation plasticity history and specific work of fracture it is necessary to be able to determine what particular deformation will occur under a load, including the plastic and elastic deformation components.   The elastic component can be determined by modelling the specimen in FEA software with elastic properties and varying crack lengths.   The plastic deformation component may similarly be modelled but using true plastic stress– log strain data for each strain hardened state of the steel.

4.2   Determination of Bar Elastic Compliance Function

A 50 mm deep x 40 mm wide rectangular bar simply supported with a span of 600mm and a single point load was modelled in ABAQUS (Figure 6).   The bar is similar to one reported by Kuwamura and Takagi [3], with a 0.5 mm deep 30 degree notch cut into the top and bottom faces.   In this case however no deepening in the section occurs at mid-span apart from variation in the crack depth on the tension face. This was done to simplify the FEA modelling (Figure 7). The bar is sized so that shear stresses are small and won't cause significant interaction effects with the flexural stresses.

Crack lengths of 0.5, 2.0, 3.0, 5.0, 8.0 and 10.0 mm were modelled on the tension face to determine the change in elastic compliance of the bar as the crack length increased.   The bar was subjected to a mid-span displacement of 1.0mm for each crack length and a curve fitted to the data to determine an equation for elastic compliance as plotted in Figure 8.
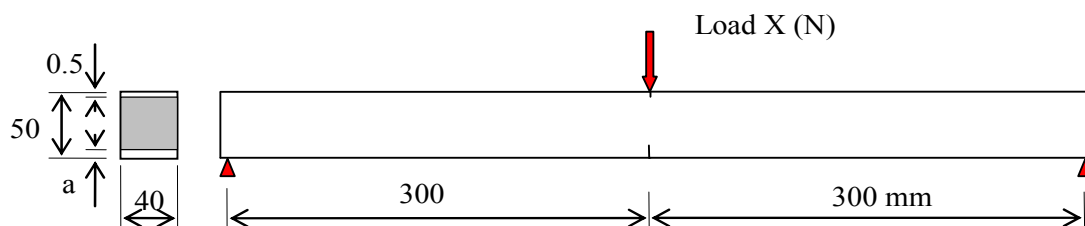
Figure 6.   50 x 40 mm Cracked Steel Bar Used in FEA Model
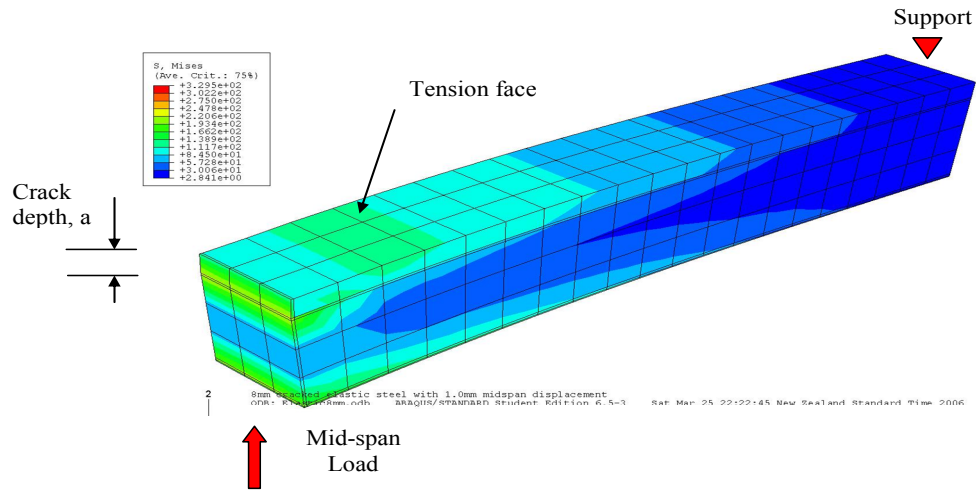
Figure 7. Elastically Deformed FEA Model of Half Span of 50 x 40 mm Bar (Loaded Upwards)
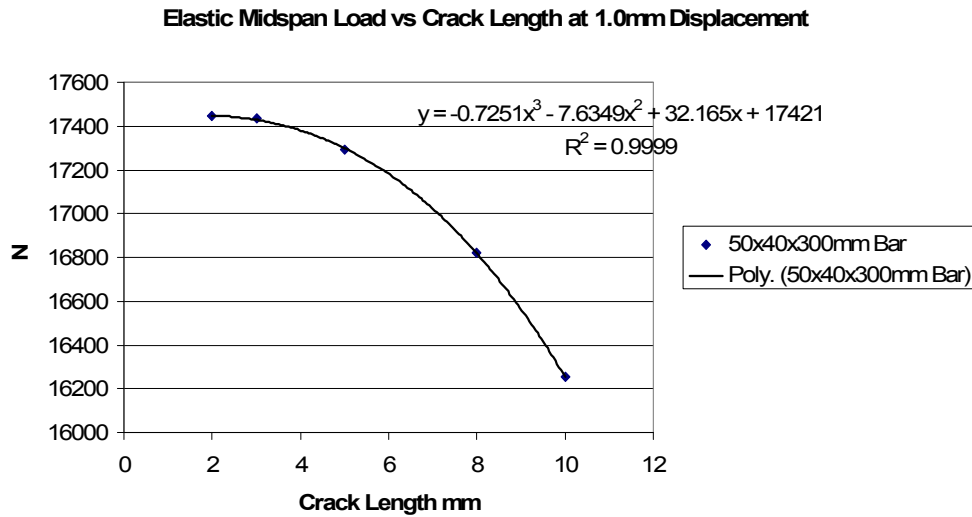
Figure 8. Elastic Compliance Function of Cracked 50 x 40 mm Bar From FEA

4.3   Calculation of Critical Crack Propagation Load

For each crack length case the mid-span load at which unstable running crack propagation would be predicted by R_c was calculated and compared to the plastic hinge load for the specimen with the range of strain hardened tensile stress strain properties derived from pre-straining tests by the authors [1].   A published applied crack tip strain energy, G, expression in terms of R for a notched bar published by Atkins and Mai [2] is used to determine cracking moment M_{Rc} .   For a rectangular bar in flexure this is

$$E^*R = \frac{36M_{Rc}^{\,2}a}{t^2W^4}Y^2$$

(5)

$$Y = 1.992 - 2.468\left(\frac{a}{W}\right) + 12.97\left(\frac{a}{W}\right)^2 - 23.17\left(\frac{a}{W}\right)^3 + 24.80\left(\frac{a}{W}\right)^4$$

(6)

a = Crack depth (m)   W = Bar depth   t = Bar thickness

L = Bar span M_{Rc} = Bending moment at mid – span (kNm)

This equation can be re-written in terms of the critical cracking moment M_{Rc}

$$M_{Rc} = \sqrt{\frac{E^* R t^2 W^4}{36 a Y^2}} = \frac{X_{Rc} \, L}{4} \tag{7}$$

$$E^* = \frac{E}{1 - v^2} \quad \text{plane strain} \tag{8}$$

For an 8 mm crack in the bar, with R=38 kJ/m^2

$$Y = 1.992 - 2.468\left(\frac{8}{50}\right) + 12.97\left(\frac{8}{50}\right)^2 - 23.17\left(\frac{8}{50}\right)^3 + 24.80\left(\frac{8}{50}\right)^4 = 1.851$$

$$M_{Rc} = \sqrt{\frac{210000 \times 38000 \times 0.04^2 \times 0.05^4}{\left(1 - 0.3^2\right) \times 36 \times 0.008 \times 1.851^2}} = 9.427 \quad \text{kNm}$$

$$X_{Rc} = \frac{4 M_{Rc}}{L} = \frac{4 \times 9.427}{0.60} = 62.85 \quad \text{kN}$$

4.4   Upper Bound Plastic Hinge Load

Upper bound mid-span loads for a notched bar (Figure 9) may be calculated for plastic hinge development using classical virtual work approaches for a rectangular bar by Knott [4].   A plastic hinge with a maximum included angle of 66° 50' gives

$$M_{pl} = \tau_y \, t \frac{(W-a)^2}{2} \cos ec^2 \alpha . \alpha = 0.345 \, \sigma_y \, t \, (W-a)^2 \tag{9}$$

$$\sigma_y = 2\tau_y \tag{10}$$
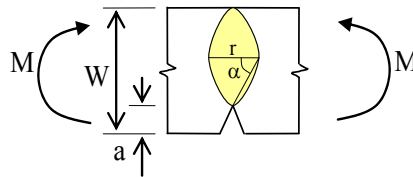
Figure 9. Plastic Hinge Zone in Notched Bar

This would be bounded by the gross unnotched section plastic moment limit from beam theory of

$$M_{pl} = 0.25 \sigma_y \, t \, W^2 \tag{11}$$

If the cracking moment M_{Rc} is reached before the section reaches M_{pl} then running fracture will occur before the attainment of the reference value of monotonic displacement ductility μ=1.   To allow for strain hardening after significant rotation, the yield stress is substituted for the flow stress, the average of the yield and ultimate tensile stress of the material

$$\sigma_{fl} = \frac{\sigma_y + \sigma_u}{2} \qquad\qquad\qquad\qquad\qquad\qquad\qquad\qquad (12)$$

So for the bar with an 8 mm crack in as-received 300Plus steel the upper bound plastic hinge loads at yield for a notched and full section are

$$M_{pl.notch} = 0.345 \times 307 \times 40 \times (50-8)^2 \times 10^{-6} = 7.473 \quad kNm$$

$$M_{pl.gross} = 0.25 \times 307 \times 40 \times 50^2 \times 10^{-6} = 7.675 \quad kNm$$

$$M_{pl.hinge} = 7.473 \quad kNm$$

For a crack depth of 8mm the notched section hinge capacity governs hinge formation at 7.473 kNm.   This is less than M_{Rc}= 9.427 kNm, so running fracture won't occur before full development of the plastic hinge.

The maximum strain hardened or over-strength plastic hinge moment of the cracked section M_{os} using the flow stress is

$$\sigma_{fl} = \frac{306 + 511}{2} = 409 \text{ MPa}$$

is

$$M_{os.hinge} = 0.345 \times 409 \times 40 \times (50-8)^2 \times 10^{-6} = 9.956 \quad kNm$$

This is greater than M_{Rc}, so for an 8mm deep crack, fast running fracture is expected after significant development of plastic hinge rotation, but before achievement of the theoretical upper bound strain hardened plastic hinge moment. Results of calculations for cracking moment and plastic hinge limit states are plotted to develop the surfaces in Figure 10, Figure 11 and Figure 12.

4.5   Plastic Hinge Formation and Cracking Limit State Surfaces

The limit state surface of bending moment at which crack propagation occurs is shown in Figure 10. The surface showing the point at which plastic hinge development occurs is seen in Figure 11, and the upper bound over-strength plastic moment surface is shown in Figure 12. These considered together show that as the crack lengthens and strain hardening increases then cracking will occur before a plastic hinge can fully form in some cases.   In other cases cracking will occur after the development of a plastic hinge but before development of the hinge strain hardened or over-strength capacity.   In the final case no cracking will occur before development of the strain hardened moment capacity followed by stable necking and micro-void coalescence based fracture. Cleavage fracture modes with rapid running fracture have been observed by Kuwamura and Takagi [3] in this last condition after necking has initiated.   However such a mode of fracture is not modelled by the method proposed for the reasons discussed in the following section.

In summary the intersection of the crack propagation surface with the plastic hinge and strain hardened surfaces determines which limit state governs for a particular pre-strain and crack length.

Critical Cracking Moment vs Crack Length & Steel Pre-strain %
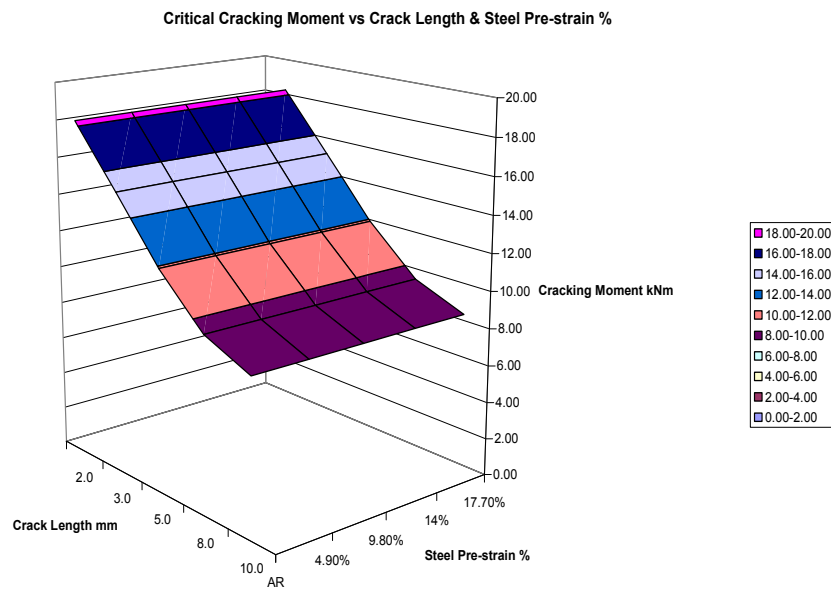
Figure 10. Cracking Moment Limit Surface

Plastic Hinge Moment vs Crack Length & Steel Pre-strain %
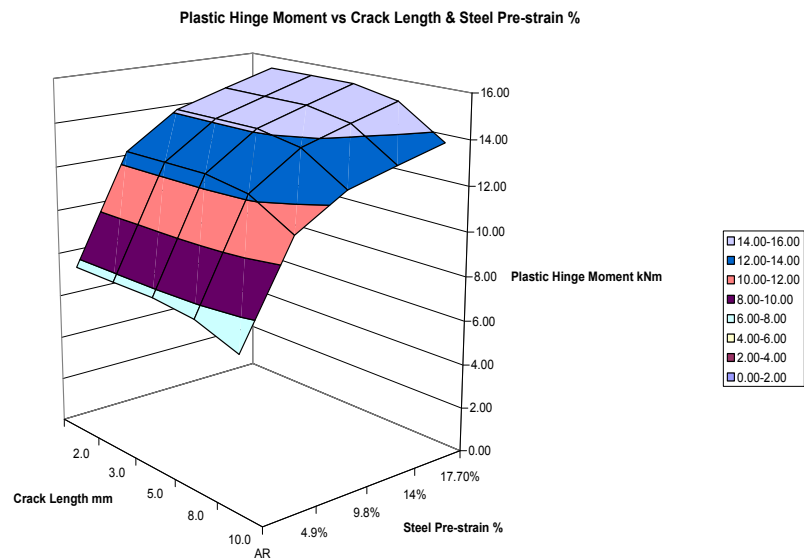
Figure 11. Plastic Hinge Development Limit Surface

Plastic Hinge Overstrength Moment vs Crack Length & Steel Pre-strain %
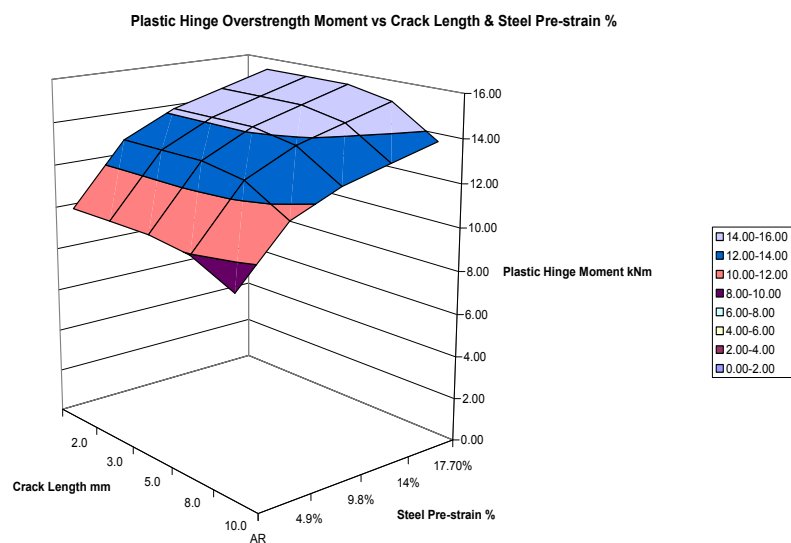
Figure 12. Over-Strength Moment Limit State Surface
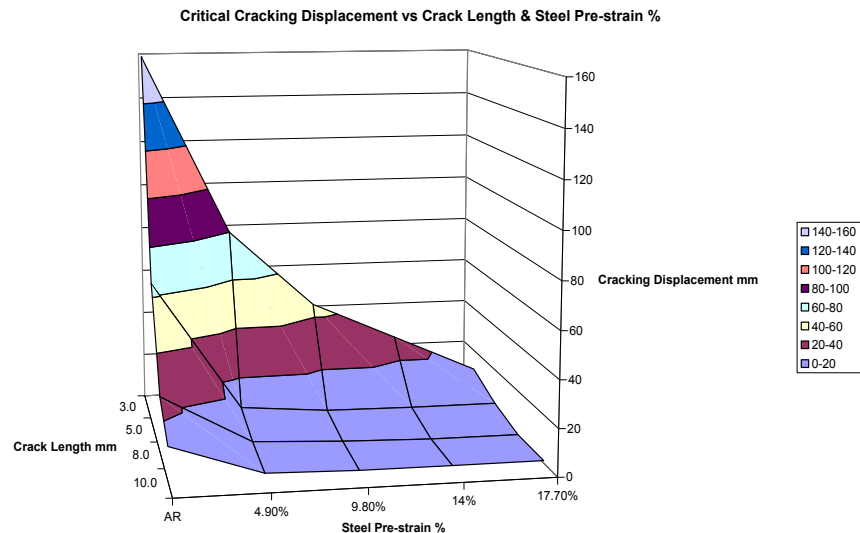
Figure 13. Displacement Limits for Pre-Strained Steel with Varying Crack Lengths

4.6   Member Displacement at Cracking Load and Necking

There will be a limit on how much rotation and therefore displacement can be sustained by the section before the other limiting condition of necking and ductile fracture occurs.   Once necking occurs the cracking mechanism predicted by this method can not occur.   This method assumes proportional elongation of the section, whereas once necking commences the elongation becomes localised and stable fracture involving micro-void coalescence is assumed to occur.

The point at which necking commences is not easy to determine even using Finite Element Analysis (FEA).   A different set of modelling assumptions are needed to consider the effect of micro-void coalescence involving continuum mechanics.   In that approach the steel is modelled using porous plasticity theory.   This requires assumptions about initial micro-particle density and size.   Only a "best judged" estimate of properties can be made using published data used in some studies done internationally.   Consequently the properties need to be confirmed on the basis of actual testing to calibrate the FEA model.

This would give some indication of whether running fracture failure will occur after the initiation of necking.   In this study the modelling has not been taken to that level and is not necessary for most structural engineering considerations of ductility and endurance.   This is because the initiation of necking also coincides with peak tensile strength of the material and thereafter a rapid drop off in load carrying capacity of the member.   However, having determined the cracking load, and if some upper bound approach is used to identify the necking limit state, it is necessary to determine what the mid-span displacement of the bar will be at that load if a measure of member displacement ductility is sought.

To achieve this, the displacement of the bar at the calculated critical cracking load may be determined from an elasto-plastic FEA analysis of the bar at a given crack length.   The same FEA models used for the determination of elastic compliance are used but with the actual tensile properties of the steels.   In this instance a strain hardened moment capacity limit is defined using the flow stress as an upper bound average stress in the plastic hinge with full development of hinge rotations.

It is apparent from the critical displacement plot that the ability of the steel bar to sustain significant displacement before cracking reduces as both strain hardening and crack length increases. Once over 4.9% pre-strain and 5 mm crack length, the bar can sustain no more than around 8 mm mid-span displacement before crack propagation occurs, whereas in the as-received condition with the same crack length the bar could sustain up to 65 mm displacement. This result goes a significant way to explaining observed behaviour in structures subjected to seismic inelastic demands.

5.   EXAMPLE ASSESSMENT OF CYCLIC MEMBER DUCTILE ENDURANCE

5.1   Overview

The same 50 mm deep x 40 mm wide rectangular bar, simply supported with a span of 600mm, used in the assessment of monotonic fracture limit states is used to assess cyclic fracture limit states. Some knowledge of what the strain hardened state of the steel will be at a particular step in the cyclic loading cycle is then needed to make some assessment of the likelihood of stable plastic flow or running fracture at any point in the loading regime.

5.2   Cyclic Ductility Using Similitude Approach

The ability to assess the monotonic total displacement at which crack propagation will occur, allows the cyclic ductility to be determined for a range of cyclic displacement amplitudes using the Kuwamura Takagi [3] similitude relationship.

The monotonic displacement ductility, μ_p, is the ratio of the plastic displacement, δ_p,   in terms of the elastic displacement at development of the gross section plastic moment, δ_y,

$$\mu_p = \frac{\delta_p}{\delta_y} \tag{13}$$

For the 50 mm x 40 mm bar with a 5 mm crack, running fracture is not expected to govern for the as-received steel.   However if the 4.9% pre-strained steel was used the development of running fracture in the bar is predicted to occur at a lower load. The bar's monotonic displacement ductility, which is the plastic displacement at monotonic crack propagation or fracture over the elastic displacement at the development of plastic section capacity, may therefore be calculated for that pre-strained state.

5.3   Monotonic Brittle Fracture Curves

Monotonic brittle fracture curves may be calculated using this approach by determining the plastic displacement ratio at fracture under monotonic load

$$\eta_{pM} = \frac{\delta_{pM}}{\delta_y} \tag{14}$$

for each of the crack lengths for each pre-strained steel state.   The results of these calculations are plotted in Figure 14.

5.4   Constant Amplitude Cyclic Brittle Fracture Ductility to NZS 1170.5

The similitude relationship allows the monotonic ductility ratings of the cracked steel beam in each pre-strain condition to be related to the NZS 1170.5 [5] cyclic ductility rating system.   In the NZS 1170.5 context ductility is defined as,

$$\mu = \frac{\delta_{max}}{\delta_y} = \frac{\delta_y + \delta_p}{\delta_y} = 1 + \mu_p \tag{15}$$

This is the total displacement ductility of the system being considered, not just the plastic displacement ductility used in the Japanese case. Under the NZS 1170.5 regime the specimen need only develop three cycles of displacement at a given constant displacement ductility without losing more than 20% of its strength.   The New Zealand ductility requirement is one of the least severe requirements internationally as no development of damage needs to be accounted for in cycles preceding the ductility classification cycles.

For example the number of complete cycles that the as-received steel bar with a 2.0mm crack at a ductility demand of μ=10 will achieve is calculated as follows:

The monotonic plastic displacement ratio, $\eta_{pM} = 192$.

For $\dfrac{\eta_{pM}}{\mu_p} \geq 2$ the number of quarter cycles of plastic displacement at μ_p is $N_f = \dfrac{\eta_{pM}}{\mu_p}\left(\dfrac{\eta_{pM}}{\mu_p} - 1\right)^{2/3}$

Therefore the expected number of complete cycles n, is

$$n = \frac{N_f}{4} = \frac{192}{4 \times 10}\left(\frac{192}{10} - 1\right)^{2/3} = \frac{159}{4} = 39.8$$
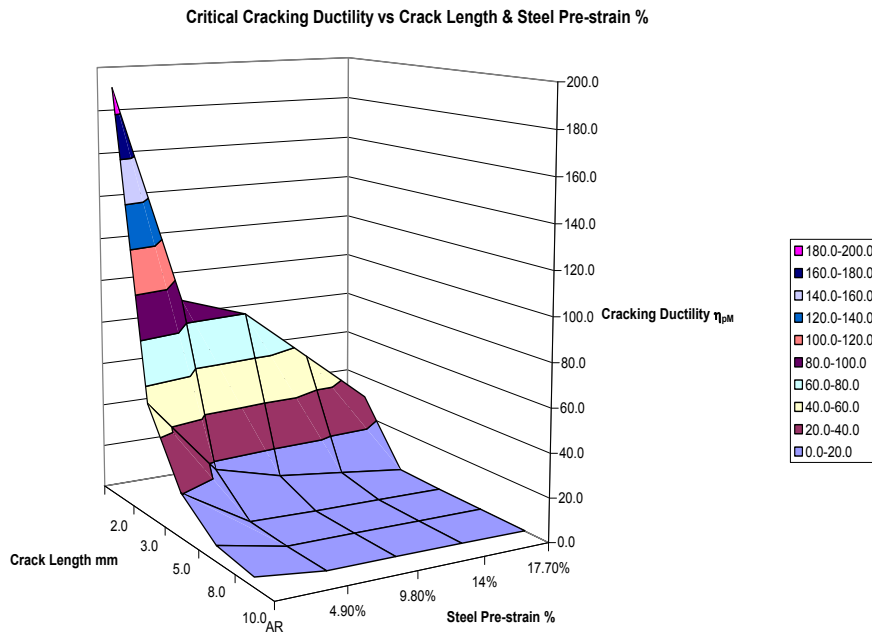
Figure 14. 50 x 40 x 600mm Bar:
Plot of Critical Cracking Ductility vs Crack Length and Steel Pre-Strain

5.5   Effect of R_c on Cyclic Fracture Ductility and Endurance

The effect of reduced critical specific work of fracture, R_c, values on the cyclic ductility of the bar can be determined using the method.   When less than 12 quarter cycles or 3 full cycles are expected to be achieved by the specimen at that level of ductility demand it can not be categorised as able to achieve the particular ductility grading in accordance with NZS 1170.5.

The reduced cracking moment and related displacements lead to reduced monotonic ductility, η_{pM}, and therefore reduced cyclic ductility. The effect of reducing the as-received steel toughness is significant.   A comparative plot in Figure 15 of the two cyclic endurance and ductility curves $R_c =$ 38 kJ/m^2 and in Figure 16 $R_c =$ 30kJ/m^2 shows a reduction in the cyclic endurance at all levels of ductility.   The endurance of the tougher steel is three times that of the lower steel for the 2 mm cracked specimens;   two times greater for the 3mm cracked specimens; two and a quarter times greater for the 5mm cracked specimens; and three times greater for the 8 and 10 mm cracked items. It is therefore clear that the specific work of fracture property of a steel, has a significant effect on the ductility and cyclic endurance of structural steel members.
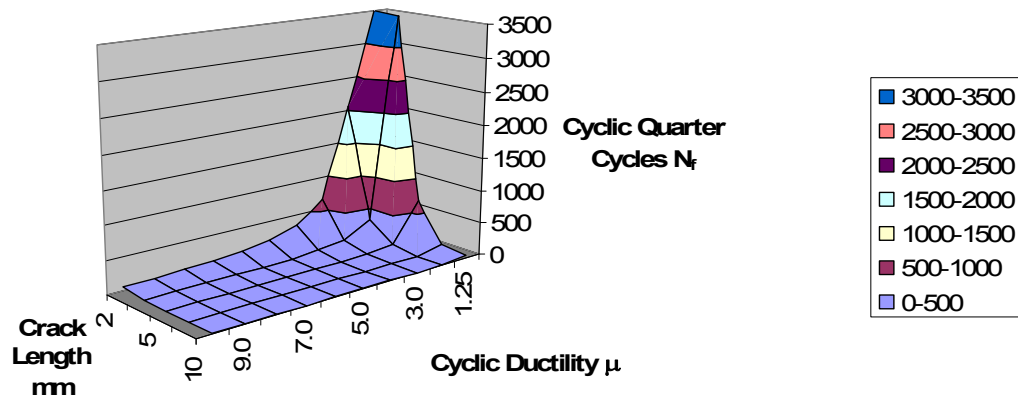
Figure 15. Cyclic Endurance and Ductility of As-Received R_c=30 kJ/m^2 Steel
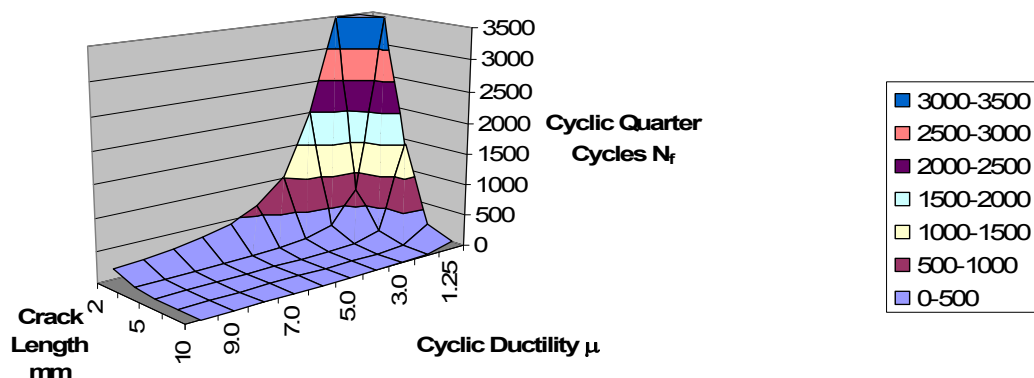
Figure 16. Cyclic Endurance and Ductility of As-Received R_c=38 kJ/m^2 Steel

5.6 Application to Variable Amplitude Cyclic Loading

The above analysis shows how constant amplitude cyclic endurance can be assessed for specimens operating at constant amplitude cyclic loading. However a method of assessing cyclic endurance for variable amplitude loading is desirable. In the first instance it is desirable to be able to classify the various seismic loading testing regimes that use progressively increasing amplitudes of displacement.

The proposed approach is that a Palmgren-Miner summation be used in which the proportion of quarter cycles required per displacement step relative to the constant amplitude endurance for cycles at that step be accumulated until the greatest step is reached at which the accumulated proportion of endurance is less than or equal to 1.0. This sets the structural ductility limit .

This is summarised in terms of ATC-24 cyclic loading in Table 1., based on the calculated ductility ratings in Tables 2 to 6. This is illustrated in Figure 17 for an ATC-24 loading regime applied to the 300Plus steel with specific work of fracture R_c=38 kJ/m^2.

The values for η_{pM} and the number of cycles N_f to running fracture are within the same range as those found in cyclic testing reported by Kuwamura and Takagi [3] for a similarly proportioned bar in their Series 2 tests made from SN490 steels. This is very encouraging with respect to validating the approach taken with the use of specific work of fracture based measures of fracture toughness in what are very ductile materials.
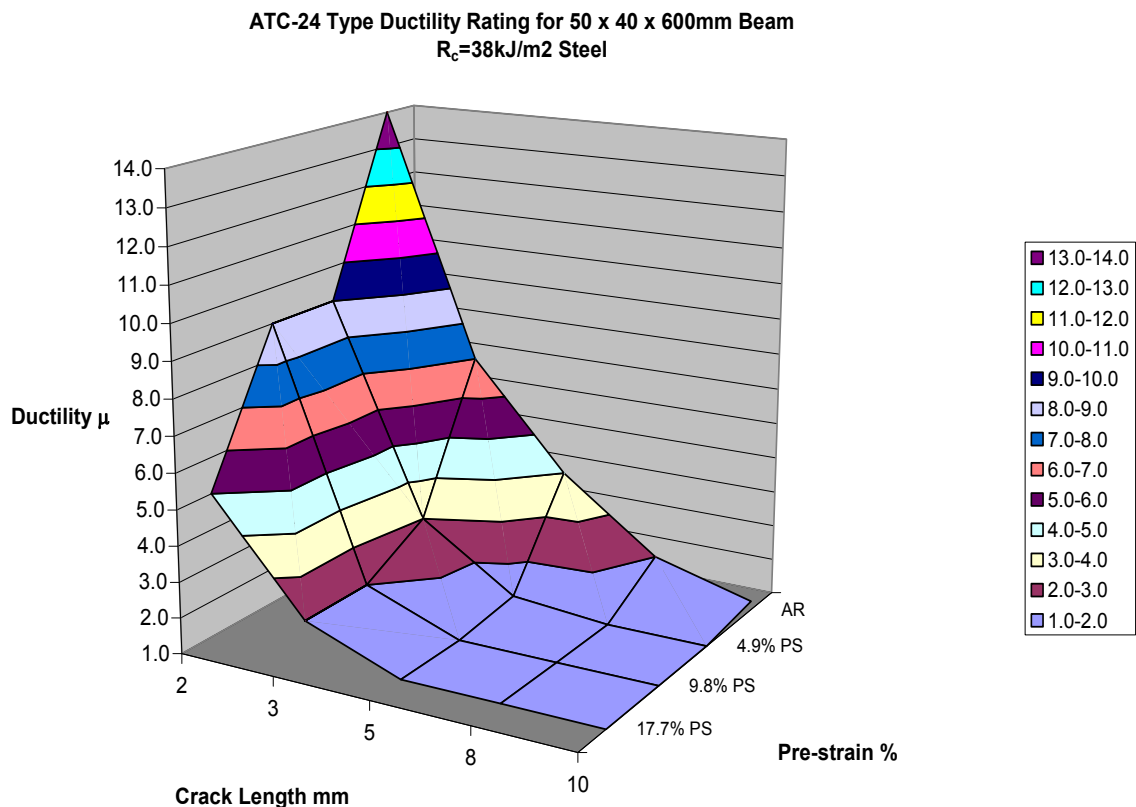
Figure 17. ATC-24 Loading Regime Cyclic Ductility Prediction for
Varying Crack Length and % Strain State

Table 1. ATC-24 Loading Regime Cyclic Ductility Prediction

Crack Length a mm	2		3		5		8		10	
Toughness Rc kJ/m²	38	30	38	30	38	30	38	30	38	30
Monotonic Ductility η_{pM}	192.0	97.6	52.6	33.4	20.4	12.5	7.4	3.8	4.5	2.2
Steel Pre-strain	ATC-24 Type Ductility Rating μ									
AR	14.0	10.0	7.0	5.0	4.0	3.0	2.0	1.25	1.25	1.25
4.9% PS	9.0		3.0		1.25		1.0		1.0	
9.8% PS	9.0		2.0		1.0		1.0		1.0	
17.7% PS	5.0		2.0		1.0		1.0		1.0	

Table 2. M Series Bar ATC-24 Cyclic Endurance Surface for Varying Crack Lengths

As-Received M: 50 x 40 x 600 mm Bar: R_c=30 kJ/m²

Crack Length a mm	2		3		5		8		10	
Monotonic Ductility η_{pM}	97.6		33.4		12.5		3.8		2.2	
ATC-24 Ductility μ	10.0		5.0		3.0		1.25		1.25	
Plastic Ductility μ_p	N_f	$12/N_f$	N_f	$12/N_f$	N_f	$12/N_f$	N_f	$12/N_f$	N_f	$12/N_f$
0.25	20818		3474		670		89	0.135	35	0.347
1.0	2055	0.006	339	0.035	64	0.188	8		2	
2.0	643	0.019	105	0.115	19	0.636	2		1	
3.0	325	0.037	52	0.230	9		1		1	
4.0	200	0.060	32	0.380	5		1		1	
5.0	137	0.088	21		3		1		0	
6.0	100	0.120	15		2		1		0	
7.0	30	0.398	4		1		0		0	
8.0	26	0.459	3		1		0		0	
9.0	23	0.523	3		1		0		0	
Endurance Ratio		1.709		0.760		0.824		0.135		0.347

Table 3 As-Received 300+ Bar ATC-24 Cyclic Endurance Surface for Varying Crack Lengths

As-Received 300+: 50 x 40 x 600 mm Bar: R_c=38 kJ/m²

Crack Length a mm	2		3		5		8		10	
Monotonic Ductility η_{pM}	192.0		52.6		20.4		7.4		4.5	
ATC-24 Ductility μ	14.0		7.0		4.0		2.0		1.25	
Plastic Ductility μ_p	N_f	$12/N_f$	N_f	$12/N_f$	N_f	$12/N_f$	N_f	$12/N_f$	N_f	$12/N_f$
0.25	64351		7419		1523		277		119	0.101
1.0	6368	0.002	729	0.016	147	0.081	26	0.470	10	
2.0	1999	0.006	227	0.053	45	0.268	7		3	
3.0	1013	0.012	114	0.105	22	0.547	3		2	
4.0	625	0.019	69	0.173	13		2		1	
5.0	429	0.028	47	0.254	9		1		1	
6.0	316	0.038	34	0.349	6		1		1	
7.0	243	0.049	26		4		1		1	
8.0	194	0.062	21		3		1		1	
9.0	159	0.076	17		3		1		1	
10.0	133	0.090	14		2		1		0	
11.0	113	0.106	12		2		1		0	
12.0	97	0.123	10		2		1		0	
13.0	85	0.141	9		2		1		0	
14.0	75	0.161	7		1		1		0	
Endurance Ratio		0.913		0.950		0.896		0.470		0.101

Table 4.   4.9% Pre-Strained 300+ Bar ATC-24 Cyclic Endurance Surface for Varying Cracks

4.9% Pre-strained 300+: 50 x 40 x 600 mm Bar: R_c=38 kJ/m²

Crack Length a mm	2		3		5		8		10	
Monotonic Ductility η_{pM}	90.0		16.6		1.6		0.7		0.7	
ATC-24 Ductility μ	9.0		3.0		1.25		1.0		1.0	
Plastic Ductility μ_p	N_f	$12/N_f$	N_f	$12/N_f$	N_f	$12/N_f$	N_f	$12/N_f$	N_f	$12/N_f$
0.25	18184		1078		20	0.609	4		4	
1.0	1794	0.007	104	0.116	2		1		1	
2.0	561	0.021	31	0.384	1		0		0	
3.0	283	0.042	15		1		0		0	
4.0	174	0.069	9		0		0		0	
5.0	119	0.101	6		0		0		0	
6.0	87	0.138	4		0		0		0	
7.0	67	0.179	3		0		0		0	
8.0	53	0.226	2		0		0		0	
9.0	43		2		0		0		0	
Endurance Ratio		0.784		0.500		0.609		0.000		0.000

Table 5.   9.8% Pre-Strained 300+ Bar ATC-24 Cyclic Endurance Surface for Varying Cracks

9.8% Pre-strained 300+: 50 x 40 x 600 mm Bar: R_c=38 kJ/m²

Crack Length a mm	2		3		5		8		10	
Monotonic Ductility η_{pM}	79.8		8.3		0.9		0.7		0.7	
ATC-24 Ductility μ	9.0		2.0		1.0		1.0		1.0	
Plastic Ductility μ_p	N_f	$12/N_f$	N_f	$12/N_f$	N_f	$12/N_f$	N_f	$12/N_f$	N_f	$12/N_f$
0.25	14877		336		7		4		4	
1.0	1467	0.008	31	0.384	1		1		1	
2.0	458	0.026	9		0		0		0	
3.0	231	0.052	4		0		0		0	
4.0	142	0.085	2		0		0		0	
5.0	97	0.124	2		0		0		0	
6.0	71	0.169	1		0		0		0	
7.0	54	0.221	1		0		0		0	
8.0	43	0.279	1		0		0		0	
9.0	35		1		0		0		0	
Endurance Ratio		0.964		0.384		0.000		0.000		0.000

Table 6.   17.7% Pre-Strained 300+ Bar ATC-24 Cyclic Endurance Surface for Varying Cracks

17.7% Pre-strained 300+: 50 x 40 x 600 mm Bar: R_c=38 kJ/m²

Crack Length a mm	2		3		5		8		10	
Monotonic Ductility η_{pM}	29.7		0.7		0.2		0.2		0.2	
ATC-24 Ductility μ	5.0		2.0		1.0		1.0		1.0	
Plastic Ductility μ_p	N_f	$12/N_f$	N_f	$12/N_f$	N_f	$12/N_f$	N_f	$12/N_f$	N_f	$12/N_f$
0.25	2855		336		7		4		4	
1.0	278	0.043	31	0.384	1		1		1	
2.0	86	0.140	9		0		0		0	
3.0	43	0.282	4		0		0		0	
4.0	26	0.468	2		0		0		0	
5.0	17		2		0		0		0	
6.0	12		1		0		0		0	
7.0	9		1		0		0		0	
8.0	7		1		0		0		0	
9.0	6		1		0		0		0	
Endurance Ratio		0.933		0.384						

6. CONCLUSIONS

The application of Specific Work of Fracture concepts to deriving critical specific work of fracture R_c values for ductile steels from CTOD specimens has proved to be useful, allowing a prediction of fracture behaviour for a range of crack depths and strain hardening conditions. The importance of using a Direct Current Potential Drop approach to assess crack growth characteristics during the CTOD tests is emphasised as this allows development of R curves related to crack area to be readily calculated throughout the test.

In conjunction with elastic and elasto-plastic finite element analyses of structural members the method allows a consistent and rational estimation of cracking load either pre- or post yielding. Limit state failure surfaces may be constructed for crack propagation loads, plastic hinge development loads and also for displacement to cracking. By using this approach to assess monotonic displacement ductility a wide range of structural configurations may potentially be analysed and assessed with respect to cyclic ductility capacity using Kuwamura's similitude relationship or the strain history approach. This is a significant benefit to structural engineering designers and researchers seeking to assess the ductile endurance of existing and new seismic resisting frames.

The combination of specific work of fracture and tensile stress-strain properties when incorporated into a finite element model allows useful prediction of fracture loads and member displacement behaviour. While the method appears valid for constant displacement amplitude behaviour a method of application for variable increasing amplitude loading cycles is proposed which utilises a Palmgren-Miner summation method. This allows ductility assessments in terms of cyclic test loading regimes to be assessed. A rain flow counting method is potentially applicable also to extend the approach to fully variable amplitude cyclic loading as commonly occurs in earthquakes. However no validation has been made of such an approach, although it seems reasonable.

A review of test results reported by Kuwamura and Takagi indicates that the values of monotonic and cyclic ductility predicted by the method proposed in this report are within the right range to be considered useful in a structural engineering assessment sense. Further calibration and refinement of the method therefore appears to be well justified.

NOTATION AND SYMBOLS

ATC-24	Applied Technology Council cyclic testing guideline
a	Crack length
B	Breadth or thickness of a CTOD specimen; Proportionality constant
B_{eff}	Effective section thickness of side-grooved CTOD specimen per BS7448.4
B_N	Net section thickness of side-grooved CTOD specimen per BS7448.4
CTOD	Crack Tip Opening Displacement
DCPD	Direct current potential drop method of monitoring crack growth.
E	Youngs modulus
F	Applied force to CTOD specimen
G_c	Critical strain energy to generate crack growth
K_r	Stress intensity at crack propagation derived from an R-curve for elastic fracture without extensive plastic flow.
K_{Rc}	Equivalent elastic stress intensity at fracture derived from an R_c
K_{Ic}	Critical stress intensity at the crack tip perpendicular to the crack propagation or I-I plane for elastic brittle cracking to initiate with minimal far field plasticity in the specimen.
$M_{os.hinge}$	Over-strength plastic section capacity

M_{pl}	Bending plastic section capacity
M_{Rc}	Critical cracking moment
M_y	Bending capacity calculated at first yield of the extreme fibres of the section
N	Number of cycles under cyclic loading
N_f	Number of quarter cycles under cyclic loading to fracture
Plane strain	The stress condition at a particular location along a crack front in which the transverse restraint is fully rigid, measured in terms of strain on the 3-3 plane $\varepsilon_{33}=0$.
Plane stress	The stress condition at a particular location along a crack front in which the transverse restraint in terms of stress on the 3-3 plane $\sigma_{33}=0$.
R_c	Fracture toughness of steel based on specific work of fracture at which a crack will run without further energy input.
S	Span between outer loading points in three point bend test
SENB3	Simply supported three point bend specimen
SN490	Japanese constructional grade of steel with nominal UTS of 490 MPa
u	Displacement
u_{el}	Elastic component of displacement
W	Width of CTOD specimen
X	Applied force
Y	Stress intensity coefficient
$\Delta\delta_p$	Half-cycle plastic displacement
ΔK	Change in stress intensity during cyclic loading
δ_c	Crack tip opening displacement at fracture
δ_{pM}	Total monotonic plastic displacement of an applied load at fracture
η_p	Cumulative cyclic plastic displacement ratio at fracture
η_{pM}	Plastic displacement ratio at fracture under monotonic load
μ	Total displacement ductility amplitude
μ_p	Cyclic plastic displacement ductility amplitude
ν	Poissons ratio
$\Sigma\Delta\delta_p$	Cumulative absolute plastic cyclic displacement at fracture
σ_{fl}	Flow stress
σ_{fr}	Fracture stress
σ_u	Ultimate tensile stress
σ_y	Yield stress
σ_{crit}	Critical section stress at which fracture will occur
τ_y	Dislocation shear yield stress of a crystal

REFERENCES

[1] Hyland, C.W.K., Ferguson, W.G. and Butterworth, J.W., "Effects of Pre-strain and Aging on the Fracture Toughness of Australasian Constructional Mild Steel", Proceedings of Structural Integrity and Fracture 2004, Brisbane, 2004.

[2] Atkins, A.G. and Mai, Y.-W., "Elastic and Plastic Fracture: Metals, Polymers, Ceramics, Composites, Biological Materials", Ellis Horwood Limited, Chichester, 1985.

[3] Kuwamura, H., and Takagi, N., "Similitude Law of Prefracture Hysteresis of Steel Members", Journal of Structural Engineering, Vol. 130, No. 5, pp. 752-761, 2004.

[4] Knott, J.F., "Fundamentals of Fracture Mechanics", Cambridge University, 1973.

[5] Standards New Zealand, "Structural Loadings Standard: Earthquake", NZS1170.5, Wellington, 2005.

PRACTICAL ANALYSIS PROCEDURE FOR COMPRESSIVE LOCAL BUCKLING OF SKIN SHEETS IN COMPOSITE PANELS

X. Ma[1], J.W. Butterworth[2, *] and G.C. Clifton[3]

[1] Postdoctoral Research Fellow, Department of Civil and Environmental Engineering,
University of Auckland, Auckland, New Zealand
[2] Associate Professor, Department of Civil and Environmental Engineering,
University of Auckland, Auckland, New Zealand
*(Corresponding author: Email: jw.butterworth@auckland.ac.nz)
[3] Associate Professor, Department of Civil and Environmental Engineering,
University of Auckland, Auckland, New Zealand

ABSTRACT: This paper addresses the problem of determining the relationship between the properties of a composite wall panel, consisting of a thin sheet steel outer skin filled with light weight concrete or similar material, and the initiation of skin buckling. The skin sheet, considered as an infinite thin plate with two clamped lateral edges resting on a tensionless Winkler foundation, is simplified to a one-dimensional mechanical model by assuming a buckling mode function in terms of the lateral coordinates. After the governing differential equations for the plate sections in the contact and non-contact regions have been solved, the problem reduces to two nonlinear algebraic equations. Practical formulas for the buckling coefficient are developed in terms of a non-dimensional filler stiffness factor, defined in terms of the filler properties and its thickness to width ratio. Comparison of the results with existing theory and finite element analyses show good agreement.

Keywords: Compressive buckling; tensionless Winkler foundations; clamped rectangular plates; local buckling; composite panels

1. INTRODUCTION

Composite panels are widely used in the civil engineering field. Panels which consist of an external skin sheet containing a light-weight filler are likely under compressive stress conditions resulting from mechanical or thermal loading, to exhibit skin buckling in which sections of the skin become separated (delaminated) from the core material and buckle away from it. This paper addresses the problem of determining the relationship between the properties of a wall panel and the initiation of skin buckling. Although the initiation of skin buckling may not always lead to failure, or even measurable loss of strength or stiffness, it is a significant turning point in behaviour and appearance that needs to be identified and suppressed under in-service loading.

This type of buckling problem may be modelled as a skin sheet supported by a tensionless elastic filler material, leading to a problem which is difficult to analyse due to the nonlinearities resulting from the unilateral constraint and the complexity of contact effects.

Co [1] was one of the earliest researchers on the contact buckling problem, which was extended to a plate on tensionless rigid foundation recently by Shahwan & Waas [2] and Smith et al. [3]. As practical applications, Wright [4] assumed a buckling mode function, Uy and Bradford [5] employed a finite strip model, Smith et al. [6, 7] combined theoretical methods and experimental research together in the local buckling analysis of composite steel-concrete members. Smith et al. [8] also studied the unilateral buckling problem under shear load. Chai [9] conducted analytical and experimental studies of post-local buckling response of unilaterally constrained thin plates. Ma et al. [10] studied the elasto-plastic post-buckling behaviour and the secondary buckling phenomenon of unilaterally constrained plates. Most of the existing literature has confined itself to the case of a plate on rigid constraints.

However, in practical applications, the assumption of rigid constraints may sometimes be questionable. For example, to minimise self-weight, light filler materials are largely used in composite members, reducing the level of support available to the skin sheets. The reduction in buckling stresses may be overlooked if the filler is still regarded as a rigid constraint. We seek to establish the required stiffness of the filler in order to ensure sufficient support to enable the skin to efficiently carry compressive stress. Therefore, it is necessary to consider the elastic deformation of the filler when simulating the mechanical behaviour of light-weight composite members. Chai et al. [11] studied one-dimensional delamination buckling problems through a beam-column model, considering the support deformation at the beam ends. Based on potential energy theory, Shahwan & Waas [12] presented an infinite plate model with only two unknowns, which was capable of considering elastic deformation of the foundation. In the literature, the governing equations for plates with simply supported edges and clamped-free edges are given. As part of a new approach, Holanda & Goncalves [13] and Shen & Li [14] simulated a numerical elastic contact post-buckling model for simply supported plates on tensionless foundations through perturbation and iteration techniques. Ma et al. [15] established an analytical model for compressive buckling of plates in unilateral contact. In general, numerical difficulties arise in the solution of nonlinear equations when the contact area is being determined, especially for a system with a large number of degrees of freedom (DOF).

In this paper, for practical use and to consider the effect of deformation of filler in the contact area, the skin sheets in composite panels are considered as infinitely long thin plates with immovable ends and two clamped lateral edges resting on tensionless Winkler foundations. With an assumed buckling mode function related to lateral coordinates, a one-dimensional mathematical model is deduced on the basis of Von Karman's equations. After solving the governing buckling equations of the plate sections in both the contact and non-contact regions, the problem reduces to two nonlinear algebraic equations. The buckling coefficient is then obtained in terms of a non-dimensional foundation stiffness factor.

2.   BUCKLING MODE OF THE SKIN SHEET
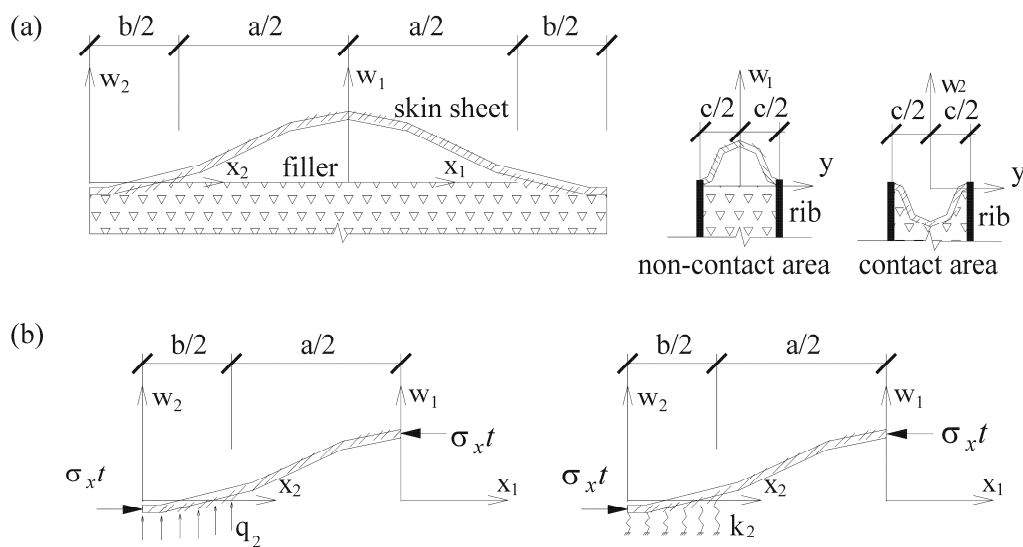
(a) Buckling Skin Sheet of One Wave Length   (b) Mechanical Model of Buckling Skin Sheet

Figure 1. Mechanical Model of Local Buckling Skin Sheet

Considering the ribs as rigid constraints and ignoring the local effect due to boundary conditions of the two loaded edges, the buckling problem of a long skin sheet is reduced to a laterally clamped infinite plate model with periodically repeating buckles. Considering a single wave length plate section, we get the mechanical model of the skin sheet as shown in Figure 1a, where the length ($a+b$) is one local buckle wave-length in the x direction; a and b are the non-contact length and the contact length between the skin sheet and the filler; and c is the single local buckle wave-length in the y direction. For practical analysis, the elastic filler may be simplified as a Winkler foundations (Figure 1b) with the foundation stiffness coefficient k_2 to be determined from the geometric and material properties of the filler.

For steel plates, the governing equation is

$$w_{i,x_ix_ix_ix_i} + 2w_{i,x_ix_iyy} + w_{i,yyyy} + \frac{\sigma_x t}{D^s}w_{i,x_ix_i} = \frac{q_i}{D^s} \qquad |x_1| \le a/2, |x_2| \le b/2 \quad i=1,2 \tag{1}$$

$$D^s = \frac{E^s t^3}{12(1-v^{s^2})} \tag{2}$$

$$q_i = \begin{cases} 0 & |x_1| \le a/2 \quad i=1 \\ q_2(x_2,y) & |x_2| \le b/2 \quad i=2 \end{cases} \tag{3}$$

where D^s, E^s, v^s, t are the bending stiffness, elastic modulus, Poisson's ratio and thickness of the skin sheet. σ_x is the normal direct stress in x_i direction; q_i is the foundation reaction on the plate; the subscript $_i$ indicates that the parameter relates to the plate section i (i=1 for non-contact plate section, i=2 for contact plate section); the subscripts $_{,x_i(,y)}$ indicate partial differentiation $\partial/\partial x_i (\partial/\partial y)$, etc. The superscript 's' means the parameter is of the skin sheet. w_1, x_1 and w_2, x_2 are the vertical displacement and the local longitudinal coordinate in the non-contact and contact areas, respectively.

Assume $w_i(x_i,y) = f_i(x_i)g(y)$, and consider the filler material as a Winkler foundation, which means

$$q_i(x_i,y) = -k_i f_i(x_i)g(y) \tag{4}$$

Eq. 1 may be rewritten as

$$f_i''''g + 2f_i''g'' + f_ig'''' + \frac{\sigma_x t}{D^s}f_i''g = -\frac{k_i}{D^s}f_ig \qquad i=1,2 \tag{5}$$

where f_i, g are the longitudinal buckling mode function and the lateral buckling mode function; $k_1(=0)$ and k_2 denote the stiffness factors of the Winkler foundation. The superscript $'$ denotes differentiation with respect to x or y.

The boundary condition of the problem is

$$g(\pm c/2) = g'(\pm c/2) = 0 \tag{6}$$

The continuity condition between f_1, f_2 is

$$f_1(-a/2) = f_2(b/2) \tag{7a}$$
$$f_1'(-a/2) = f_2'(b/2) \tag{7b}$$
$$f_1''(-a/2) = f_2''(b/2) \tag{7c}$$
$$f_1'''(-a/2) = f_2'''(b/2) \tag{7d}$$

To satisfy the boundary condition of Eq. 6, the lateral (buckling) mode function $g(y)$ of a clamped plate may be assumed as (Ma et al. [15])

$$g(y) = \left[1/4 - (y/c)^2\right]^2 \tag{8}$$

Taking the integral of Eq. 5 after multiplying both sides by function $g(y)$, and assuming

$$f_i(x_i) = \widetilde{f}_i(\xi_i), \xi_1 = x_1/a, \phi_1 = a/c, \xi_2 = x_2/b, \phi_2 = b/c, \ \widetilde{K} = \frac{c^2 \sigma_x t}{\pi^2 D^s} \ \text{ we get}$$

$$\widetilde{f}_i''''(\xi_i) - \phi_i^2 (24 - \pi^2 \widetilde{K}) \widetilde{f}_i''(\xi_i) + 504 \phi_i^4 (1 + \widetilde{k}_i) \widetilde{f}_i(\xi_i) = 0 \qquad |\xi_i| \le 1/2 \quad i = 1,2 \tag{9}$$

where ξ_i is the non-dimensional longitudinal coordinate variable; $\widetilde{f}_i$ is the longitudinal buckling mode function in terms of the non-dimensional variable ξ_i; ϕ_i is the aspect ratio of the plate section; $\widetilde{K}$ is the load coefficient; $\widetilde{k}_1 = 0$; $\widetilde{k}_2 = k_r = \frac{c^4 k_2}{504 D^s}$ is the relative Winkler spring coefficient, which may be obtained based on the geometric and material properties of the filler.

The symmetric solution of Eq. 9 may be written as

$$\widetilde{f}_i(\xi_i) = A_{1i} f_{1i} + A_{2i} f_{2i} \tag{10}$$

where A_{1i}, A_{2i} are coefficients to be determined; the functions f_{1i}, f_{2i} may be obtained based on the following three cases

<u>Case 1</u> $\quad \Delta_i = \left(\frac{\pi^2 \widetilde{K}}{8} - 3\right)^2 - 31.5(1 + \widetilde{k}_i) > 0$

$$f_{1i}(\xi_i) = \cos(\alpha_i \xi_i) \tag{11a}$$

$$f_{2i}(\xi_i) = \cos(\beta_i \xi_i) \tag{11b}$$

$$\alpha_i, \beta_i = 2\phi_i \left[\frac{\pi^2 \widetilde{K}}{8} - 3 \pm \sqrt{\Delta_i}\right]^{1/2} \tag{11c}$$

<u>Case 2</u> $\quad \Delta_i = \left(\frac{\pi^2 \widetilde{K}}{8} - 3\right)^2 - 31.5(1 + \widetilde{k}_i) = 0$

$$f_{1i}(\xi_i) = \cos(\alpha_i\xi_i) \tag{12a}$$

$$f_{2i}(\xi_i) = \xi_i \sin(\alpha_i\xi_i) \tag{12b}$$

$$\alpha_i = 2\phi_i \left[\frac{\pi^2\widetilde{K}}{8} - 3 \right]^{1/2} \tag{12c}$$

Case 3 $\Delta_i = \left(\dfrac{\pi^2\widetilde{K}}{8} - 3 \right)^2 - 31.5(1 + \widetilde{k}_i) < 0$

$$f_{1i}(\xi_i) = \left(e^{\alpha_i\xi_i} + e^{-\alpha_i\xi_i} \right)\cos(\beta_i\xi_i) \tag{13a}$$

$$f_{2i}(\xi_i) = \left(e^{\alpha_i\xi_i} - e^{-\alpha_i\xi_i} \right)\sin(\beta_i\xi_i) \tag{13b}$$

$$\alpha_i, \beta_i = 2\phi_i \left[\sqrt{\left(\frac{\pi^2\widetilde{K}}{8} - 3 \right)^2 - \Delta_i} \mp \left(\frac{\pi^2\widetilde{K}}{8} - 3 \right) \right]^{1/2} \tag{13c}$$

The continuity condition of Eq. 7 may be rewritten as

$$\widetilde{f}_1(-1/2) = \widetilde{f}_2(1/2) \tag{14a}$$

$$\widetilde{f}_1'(-1/2)/a = \widetilde{f}_2'(1/2)/b \tag{14b}$$

$$\widetilde{f}_1''(-1/2)/a^2 = \widetilde{f}_2''(1/2)/b^2 \tag{14c}$$

$$\widetilde{f}_1'''(-1/2)/a^3 = \widetilde{f}_2'''(1/2)/b^3 \tag{14d}$$

Eq. 14 may be expressed in matrix form as

$$\begin{bmatrix} f_{11}(-1/2) & f_{21}(-1/2) & -f_{12}(1/2) & -f_{22}(1/2) \\ f_{11}'(-1/2)/a & f_{21}'(-1/2)/a & -f_{12}'(1/2)/b & -f_{22}'(1/2)/b \\ f_{11}''(-1/2)/a^2 & f_{21}''(-1/2)/a^2 & -f_{12}''(1/2)/b^2 & -f_{22}''(1/2)/b^2 \\ f_{11}'''(-1/2)/a^3 & f_{21}'''(-1/2)/a^3 & -f_{12}'''(1/2)/b^3 & -f_{22}'''(1/2)/b^3 \end{bmatrix} \begin{bmatrix} A_{11} \\ A_{21} \\ A_{12} \\ A_{22} \end{bmatrix} = \begin{bmatrix} 0 \\ 0 \\ 0 \\ 0 \end{bmatrix} \tag{15}$$

For a non-trivial solution of Eq. 15, we require that the determinant of the coefficient matrix should vanish,

$$\begin{vmatrix} f_{11}(-1/2) & f_{21}(-1/2) & -f_{12}(1/2) & -f_{22}(1/2) \\ f_{11}'(-1/2)/a & f_{21}'(-1/2)/a & -f_{12}'(1/2)/b & -f_{22}'(1/2)/b \\ f_{11}''(-1/2)/a^2 & f_{21}''(-1/2)/a^2 & -f_{12}''(1/2)/b^2 & -f_{22}''(1/2)/b^2 \\ f_{11}'''(-1/2)/a^3 & f_{21}'''(-1/2)/a^3 & -f_{12}'''(1/2)/b^3 & -f_{22}'''(1/2)/b^3 \end{vmatrix} = 0 \tag{16a}$$

Considering that the displacement on the borderline separating contact and non-contact areas must be zero, leads to an additional equation which must be satisfied

$$\widetilde{f_1}(-1/2) = A_{11}f_{11}(-1/2) + A_{21}f_{21}(-1/2) = 0 \qquad (16b)$$

Solving Eq. 16, we obtain values of $\widetilde{K}$, ϕ_2 for different ϕ_1. The true value of ϕ_1 is that which minimizes $\widetilde{K}$. The minimum $\widetilde{K}$ is the buckling coefficient K_{cr}, which may be simulated by the numerically fitted formula

$$K_{cr} = \begin{cases} 6.97 & k_r < 0.001 \\ 0.0825(\log k_r)^3 + 0.614(\log k_r)^2 + 1.509(\log k_r) + 8.202 & 0.001 \le k_r < 1 \\ 0.0671(\log k_r)^3 - 0.608(\log k_r)^2 + 1.813(\log k_r) + 8.202 & 1 \le k_r < 1000 \\ 9.98 & 1000 \le k_r \end{cases} \qquad (17a)$$

and the corresponding compressive stress is the critical stress

$$\sigma_{cr} = \frac{\pi^2 K_{cr} D^s}{c^2 t} = \frac{\pi^2 K_{cr} E^s}{12(1-v^{s^2})}\left(\frac{t}{c}\right)^2 \qquad (17b)$$

The analytical results (Eq. 16), fitted results (Eq. 17a) of K_{cr} related to k_r and the corresponding ϕ_1, ϕ_2 are shown in Figure 2. To verify the method in the paper, the K_{cr} results are compared with ABAQUS results in Figure 2a, where the ABAQUS models are assumed to be partly constrained plates (Figure 1b) with the same constrained and non-constrained lengths as the analytical results of ϕ_1, ϕ_2 in Figure 2b.

To verify the solutions above, consider two extreme conditions: when k_r is very small, the skin sheet is similar to a non-contact long plate with two immovable ends and the other two edges built-in (plate 1); when k_r is very large, the skin sheet is similar to a plate buckling in one half-wave-length, with four edges built-in (plate 2). The comparison between the results of the method in this paper and existing theory (Bloom & Coffin [16]; Uy & Bradford [5]) are shown in Table 1:
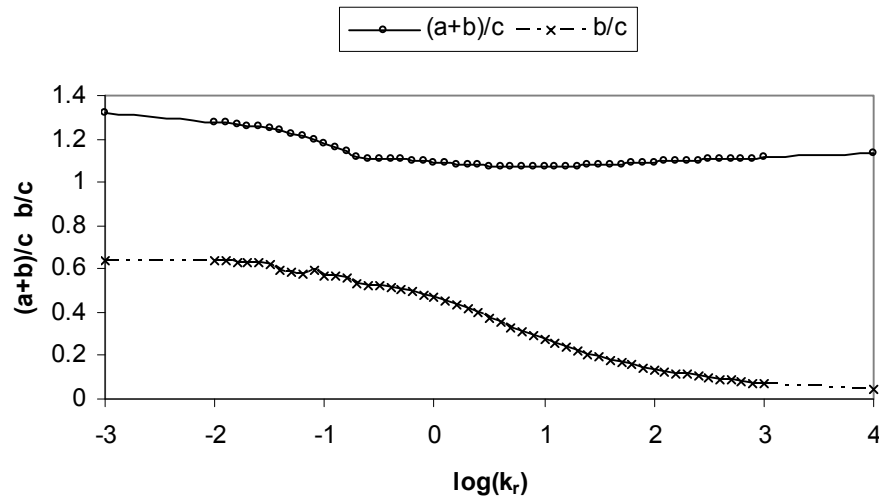
(a)
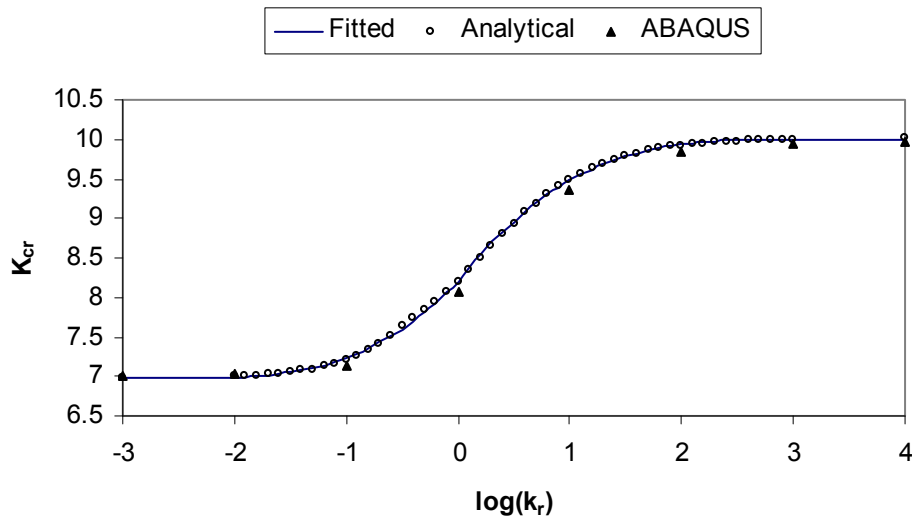
(b)

(a) Relationship between K_{cr} and $\log k_r$ (b) Relationship between ϕ_1, ϕ_2 and $\log k_r$

Figure 2. Numerical Results for Analytical Models

Table 1. Comparative Results

Method in the paper					Existing theory		
k_r	K_{cr}	$(a+b)/c$	b/c		K_{cr}	$(a+b)/c$	b/c
10^{-3}	6.98 (Eq. 16) 6.97(Eq.17a)	1.32	0.64	plate 1	6.97(Bloom)	1.32	0.66
10^6	10.01(Eq.16) 9.98(Eq.17a)	1.14	0.01	plate 2	9.80(Bloom) 10.3(Uy)	1.20(Bloom) 1.0 (Uy)	0

For finite plates resting on tensionless foundations, ABAQUS allows unilateral contact buckling analysis. The buckling coefficients of clamped plates with different aspect ratios (2, 4) are compared with the results of an infinite plate model in Figure 3, showing that the infinite plate model is applicable to plates with aspect ratios greater than about 4.
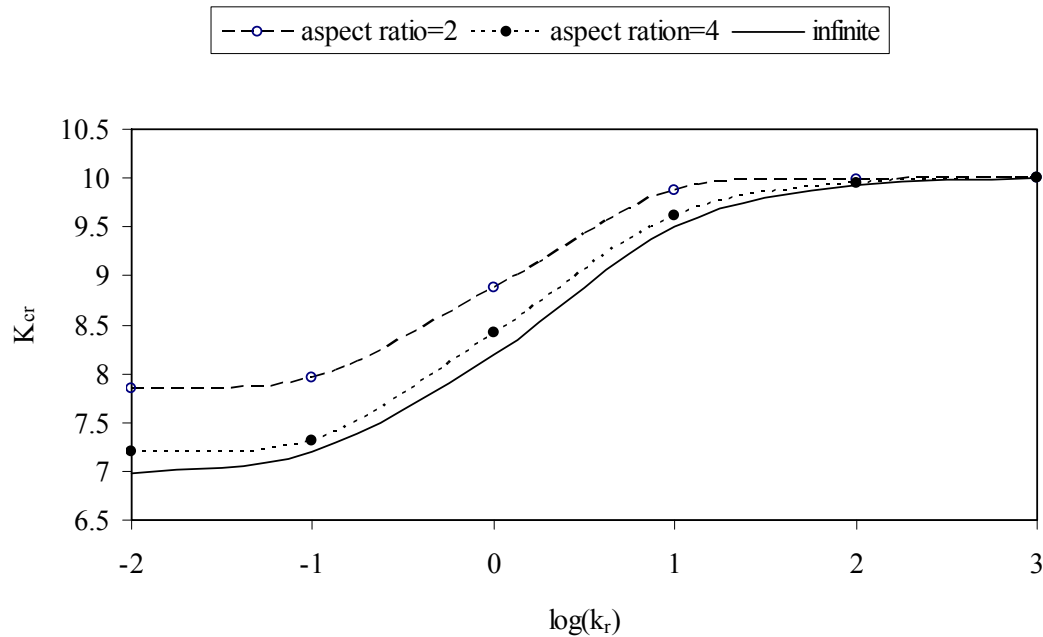

Figure 3. Buckling Coefficients of Plates with Varying Foundation Stiffness Coefficients and Different Aspect Ratios

3.   MECHANICAL MODEL FOR FILLER MATERIAL

In the simplified buckling model of the skin sheet, the 3-d continuum filler was represented by tensionless Winkler springs. The objective of this section is to deduce an appropriate stiffness coefficient for the Winkler spring based on the geometric and elastic properties of the filler.
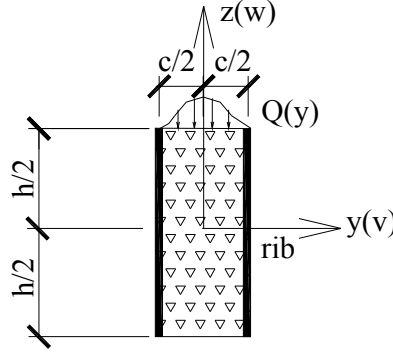

Figure 4. Mechanical Model of the Filler

Assuming the cross section of the filler at the position x_2 is in a state of plane strain (Figure 4), the boundary condition of the filler may be expressed as

$$w^f = w^f_{,y} = 0 \qquad y = \pm c/2 \tag{18}$$

$$v^f = 0 \quad y = \pm c/2 \tag{19}$$

$$\int_{-\frac{c}{2}}^{\frac{c}{2}} v^f dy = 0 \tag{20}$$

where v^f, w^f are the displacement functions of the filler material in the y, z directions respectively. The superscript 'f' means the parameter is of the filler.

Considering the boundary conditions above, the displacement functions of the filler may be assumed as

$$v^f = \sum_{m=1}^{M^f_v} \sum_{k=0}^{K^f_v} A^f_{mk} g^f_{vm}(y)(z/h)^k \tag{21}$$

$$w^f = g^f(y) \sum_{k=0}^{K^f_w} B^f_k (z/h)^k \tag{22}$$

$$g^f_{vm}(y) = \sin(2m\pi y/c) \tag{23}$$

where A^f_{mk}, B^f_k are displacement coefficients to be determined.

Considering the contact condition between the skin sheet and the surface of the filler, both vertical displacements must have the same function, which means

$$g^f(y) = g(y) = \left[1/4 - (y/c)^2\right]^2 \tag{24}$$

The potential energy of the filler material may be expressed as,

$$\Pi^f = \iint_A \Lambda^f(v^f, w^f)dA - \int_{z=h/2} Q(y)w_0^f(y)dy \tag{25}$$

$$\Lambda^f = \frac{E^f}{2(1+v^f)}\left[v_{,y}^{f\,2} + w_{,z}^{f\,2} + \frac{1}{1-2v^f}(v_{,y}^f + w_{,z}^f)^2 + \frac{1}{2}(v_{,z}^f + w_{,y}^f)^2\right] \tag{26}$$

$$w_0^f = g^f(y)\sum_{k=0}^{K_w^f} B_k^f\left(1/2\right)^k \tag{27}$$

$$Q(y) = -q_2(x_2, y) = k_2 f_2(x_2)g(y) \tag{28}$$

where Λ^f is the potential energy density function; E^f, v^f denote the elastic modulus and Poisson's ratio of the filler material, w_0^f is the vertical displacement at the surface of the filler, $Q(y)$ is the reaction of $q_2(x_2, y)$.

The solution of the problem must minimise the potential energy, which means

$$\Pi^f_{,A_{mk}^f} = 0 \quad m = 1, \cdots M_v^f; k = 0,1, \cdots, K_v^f \tag{29}$$

$$\Pi^f_{,B_k^f} = 0 \quad k = 0,1, \cdots, K_w^f \tag{30}$$

Eqs. 29, 30 may be expressed in the following matrix form

$$\begin{bmatrix} K^{A^f A^f} & K^{A^f B^f} \\ K^{B^f A^f} & K^{B^f B^f} \end{bmatrix}\begin{bmatrix} A^f \\ B^f \end{bmatrix} - \begin{bmatrix} 0 \\ F_c^f \end{bmatrix} = 0 \tag{31}$$

where $K^{A^f A^f} = \left[\Pi^f_{,A_{mk}^f A_{ij}^f}\right]$, $K^{B^f B^f} = \left[\Pi^f_{,B_k^f B_i^f}\right]$, $K^{A^f B^f} = K^{B^f A^f} = \left[\Pi^f_{,A_{mk}^f B_i^f}\right]$, $A^f = \left[A_{mk}^f\right]$,

$B^f = \left[B_k^f\right]$, $F_c^f = \left[(1/2)^k \int_{|y| \le c/2} Q(y)g^f(y)dy\right]$

Expanding Eq. 31, we obtain

$$B^f = \left[\hat{K}^{B^f B^f}\right]^{-1} F_c^f \tag{32}$$

$$\hat{K}^{B^f B^f} = K^{B^f B^f} - K^{B^f A^f}\left[K^{A^f A^f}\right]^{-1}K^{A^f B^f} \tag{33}$$

Thus Eq. 27 may be rewritten as

$$w_0^f(x_2, y) = \frac{ck_2}{E^f} d_0^f f_2(x_2) g^f(y) \tag{34}$$

where non-dimensional factor d_0^f may be expressed as

$$d_0^f = \frac{E^f \left[(1/2)^k\right]^T \left[\hat{K}^{B^f B^f}\right]^{-1} \left[(1/2)^k\right]}{630} \tag{35}$$

Considering that both the plate and the filler surface in the contact area have the same vertical displacement,

$$w_0^f(x_2, y) = w_2(x_2, y) = f_2(x_2) g(y) \tag{36}$$

Comparing Eqs. 24, 34, 36 and 9, we get

$$k_2 = \frac{E^f}{c \cdot d_0^f} \tag{37}$$

$$\tilde{k}_2 = k_r = \frac{1 - v^{s^2}}{42 d_0^f} \frac{E^f}{E^s} \left(\frac{c}{t}\right)^3 \tag{38}$$

Non-dimensional factor d_0^f related to h/c and v^f is shown in Table 2.

To verify the potential energy method (PEM) above , the displacement of an example case is compared with ABAQUS results in Figure 5, where $c=1$, $E^f = 1$, $v^f = 0$, $Q(y) = g(y)$.
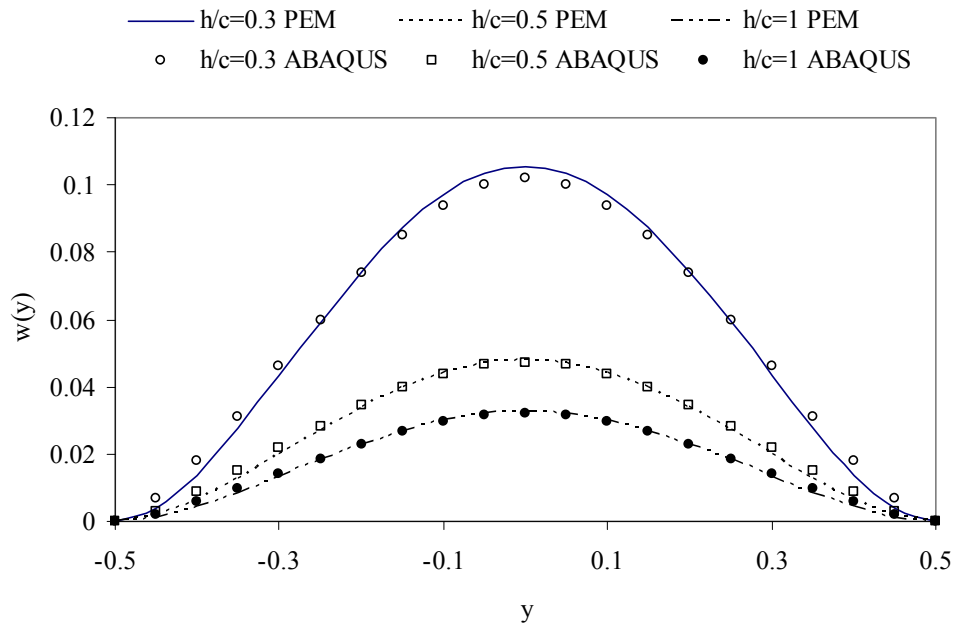

Figure 5. Comparison of Filler Displacement Profiles from PEM and ABAQUS Analyses

Table 2. Non-dimensional Factor d_0^f

h/c	0.3	0.4	0.5	0.6	0.7	0.8	0.9	1.0
$v^f = 0.0$	1.69	1.03	0.77	0.65	0.59	0.55	0.53	0.52
$v^f = 0.1$	1.73	1.06	0.80	0.67	0.61	0.57	0.55	0.54
$v^f = 0.2$	1.72	1.07	0.81	0.68	0.61	0.57	0.55	0.53
$v^f = 0.3$	1.62	1.03	0.79	0.65	0.59	0.54	0.52	0.50
$v^f = 0.4$	1.40	0.93	0.71	0.59	0.52	0.47	0.44	0.42

4.   PRACTICAL DESIGN PROCEDURE AND EXAMPLE

For practical design, the effective width is often employed to determine the compressive loading capacity of postbuckling thin plates. According to the Australian/New Zealand Standard "Cold-formed steel structures" (AS/NZS 4600:1996 [17]), the effective width factor may be expressed as

$$\rho = \begin{cases} 1 & \lambda \le 0.673 \\ (1 - 0.22 / \lambda) / \lambda & \lambda > 0.673 \end{cases} \tag{39}$$

where ρ is the effective width factor; $\lambda = \sqrt{f_y / \sigma_{cr}}$; f_y is the yield stress of skin material.

To illustrate the practical application of the simplified design procedure presented above, consider an example of a skin sheet with t/c=1/200, $E^s = 2.05 \times 10^5 MPa$, $v^s = 0.3$, f_y=300 MPa and a filler with parameters of h/c=0.5, $v^f = 0.2$, $E^f / E^s = 0.0005$.
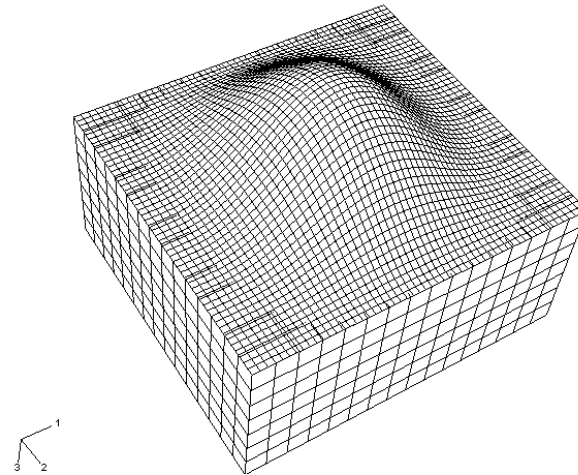

Figure 6. Buckling Mode of Skin Sheet Partly Constrained by Elastic Foundations
(an ABAQUS Model)

According to Table 2 and Eq. 37, $d_0^f = 0.81$, $k_r = 106.9$. Based on Eq. 17a, the resulting buckling coefficient $K_{cr} = 9.92$. Thus, based on Eqs. 17b and 39, the critical compressive stress $\sigma_{cr} = 45.95 MPa$ and the effective width factor ρ =0.358. The critical compressive stress agrees well with the ABAQUS result $\sigma_{cr} = 45.11 MPa$, where the ABAQUS model is assumed to be a partly constrained skin sheet with the same aspect ratio and contact length as the analytical model, i.e. $a+b$=1.10c and b=0.136c (according to Figure 2b). The buckling mode of the skin sheet resting on solid foundations is shown in Figure 6.

5.   CONCLUSIONS

A simplified contact model has been presented to consider local buckling behaviour of skin sheets unilaterally constrained by elastic filler in composite panels. After the governing differential equations for the plate sections in the contact and non-contact regions have been solved, the buckling coefficient is obtained in terms of a non-dimensional Winkler foundation stiffness factor, defined in terms of the filler properties and its thickness to width ratio. Good agreement with existing solutions and ABAQUS results has been demonstrated. Finally, numerically fitted formulas for buckling coefficient and design tables for Winkler foundation stiffness factor have been established for practical use.

ACKNOWLEDGMENTS

REFERENCES

[1]   Co, C., "Bifurcation Theory for Elastic Plates Subjected to Unilateral Conditions", Journal of Mathematical Analysis and Applications, 1977, Vol. 60, No. 2, pp. 435-448.

[2]   Shahwan, K.W. and Waas, A.M., "A Mechanical Model for the Buckling of Unilaterally Constrained Rectangular Plates", International Journal of Solids and Structures, 1994, Vol. 31, No. 1, pp. 75-87.

[3]   Smith, S.T., Bradford M.A. and Oehlers, D.J., "Numerical Convergence of Simple and Orthogonal Polynomials for the Unilateral Plate Buckling Problem Using the Rayleigh-Ritz Method", International Journal for Numerical Methods in Engineering, 1999, Vol. 44, No. 11, pp. 1685-1707.

[4]   Wright, H.D., "Local Stability of Filled and Encased Steel Section", Journal of Structural Engineering, ASCE, 1995, Vol. 12, No. 1, pp. 1382-1388.

[5]   Uy, B. and Bradford M.A., "Elastic Local Buckling of Steel Plates in Composite Steel-Concrete Members", Engineering Structures, 1996, Vol. 18, No. 3, pp.193-200.

[6]   Smith, S.T., Bradford M.A. and Oehlers, D.J., "Local Buckling of Side-plated Reinforced-Concrete Beams I: Theoretical Study", Journal of Structural Engineering, ASCE, 1999, Vol. 125, No. 6, pp. 625-634.

[7]   Smith, S.T., Bradford M.A. and Oehlers, D.J., "Local Buckling of Side-plated Reinforced-Concrete Beams II: Experimental Study", Journal of Structural Engineering, ASCE, 1999, Vol. 125, No. 6, pp. 635-643.

[8]   Smith, S. T., Bradford M. A. and Oehlers, D.J., "Elastic Buckling of Unilaterally Constrained Rectangular Plates in Pure Shear", Engineering Structures, 1999, Vol. 21, No.5, pp. 443-453.

[9]   Chai, H., "Contact Buckling and Postbuckling of Thin Rectangular Plates", Journal of Mechanics and Physics of Solids, 2001, Vol. 49, No. 2, pp.209-230.

[10]   Ma, X., Butterworth, J.W. and Clifton, G.C., "Elasto-plastic Postbuckling Analysis of Plates Resting on Tensionless Foundations", Proceedings of 19th Australasian Conference on the Mechanics of Structures and Materials, Christchurch, New Zealand, 2006, pp. 103-108.

[11]   Chai, H., Babcock, C.D. and Knauss, W.G., "One Dimensional Modeling of Failure in Laminated Plates by Delamination Buckling", International Journal of Solids and Structures, 1981, Vol. 17, No. 11, pp. 1069-1083.

[12]   Shahwan, K.W. and Waas, A.M., "Buckling on Unilaterally Constrained Infinite Plates", Journal of Engineering Mechanics, ASCE, 1998, Vol. 124, No. 2, pp. 127-136.

[13] Holanda, A.S. de, Goncalves, P.B., "Postbuckling Analysis of Plates Resting on a Tensionless Elastic Foundation", Journal of Engineering Mechanics, ASCE, 2003, Vol. 129, No. 4, pp. 438-448.

[14] Shen, H. and Li, Q.S., "Postbuckling of Shear Deformable Laminated Plates Resting on a Tensionless Elastic Foundation Subjected to Mechanical or Thermal Loading", International Journal of Solids and Structures, 2004, Vol. 41, No.16-17, pp. 4769-4785.

[15] Ma, X., Butterworth, J.W. and Clifton, G.C., "Compressive Buckling Analysis of Plates in Unilateral Contact", International Journal of Solids and Structures, 2007, Vol. 44, No. 9, pp. 2852-2862.

[16] Bloom, F. and Coffin, D., "Handbook of Thin Plate Buckling and Postbuckling", Chapman & Hall/CRC, 2001.

[17] AS/NZS 4600:1996. Australian/New Zealand Standard, "Cold-formed Steel Structures", Standards New Zealand and Standards Australia.

243

EFFECT OF END CONNECTION RESTRAINTS ON THE STABILITY OF STEEL BEAMS IN BENDING

S. Amara [1,*], D.E. Kerdal [2] and J.P. Jaspart [3]

[1] *Department of Civil Engineering, Civil Engineering Laboratory, Laghouat University, Algeria*
[2] *Professor, Department of Civil Engineering, LM2SC Laboratory, U.S.T.Oran, Algeria*
[3] *Professor, ArGEnCo Department, Liège University, 1 Chemin des Chevreuils, Liège, Belgium*
[*](*Corresponding author: tel:+213 776 13 05 51; fax:+213 29 93 26 98; email : slhamara@yahoo.com*)

ABSTRACT: The influence of the end restraint conditions on the lateral-torsional buckling of beams is investigated in detail using finite element method. The paper focuses on the limitation of Eurocode 3 regarding the lateral bending and torsional restraint coefficients k_z and k_θ of the end supports. Theoretical expressions of the coefficients k_z and k_θ taking into account the minor axis flexural restraint at the support and the end torsional restraint respectively are presented. The introduction of new coefficients k_z and k_θ representing the actual support conditions in the expression of the elastic critical moment is suggested. A comparison between the elastic critical moments for various beam cross-sections, lengths and various end restraints, obtained from the finite-element method, and those derived from EC3 ENV method, in which the proposed coefficients k_z and k_θ are introduced, confirms the reliability of these coefficients that model the end support conditions.

Keywords: Elastic lateral-torsional buckling; End restraints; Elastic critical moment; Out-of plane bending; Uniform torsion; Warping

1.   INTRODUCTION

A slender beam under the action of bending loads in the plane of maximum flexural rigidity can buckle by combined twist and lateral bending of the cross-section, unless it has continuous lateral support. This phenomenon, which was first investigated theoretically and experimentally during the nineteenth century, is known as lateral buckling. Slender beams manufactured from narrow rectangular sections or I-sections with narrow flanges, lack both lateral flexural rigidity and torsional rigidity, and if left unsupported, or supported intermittently only, they may buckle under bending stresses considerably lower than the yield or proof stress of the material. The low torsional rigidity is an important factor, so thin-walled open section beams such as channels or zeds are also susceptible to this form of instability. Box beams on the other hand, which are torsionally stiff and have similar flexural properties about the two principal axes of inertia, are very resistant to lateral buckling. The elastic buckling stress is also influenced by the conditions of support at the ends of the beam, and by the type and position of the applied loads that cause bending. In thin-walled open sections the point of application of the load with respect to the shear centre is important, and for all types of sections initial imperfections can influence the behaviour, particularly of members of intermediate length.

Research developments on lateral torsional buckling of steel members have been accompanied by the realization of updated design codes and standards. Modern steel codes for structures, such as AISC LRFD [1, 2], BS 5950-1 [3] and EC3 [4, 5], provide, on the basis of the limit state concept, design procedures to compute the lateral-torsional buckling resistance of beams. Primary, these procedures generally require the determination of the elastic critical buckling moment. Initial imperfections, residual stresses and inelastic buckling are taken into account through the use of buckling curves [6].

The elastic critical moment is directly dependent on the following factors [7]: material properties such as the modulus of elasticity and shear modulus; geometric properties of the cross-section such as the torsion constant, warping constant, and moment of inertia about the minor axis; properties of the beam such as length, and lateral bending and warping conditions at supports; and finally loading, since lateral-torsional buckling is greatly dependent on moment diagram and loading position with respect to the section shear centre. The bending moment diagram is taken into account by means of the equivalent uniform moment factor C_1. The elastic critical moment of a simply supported beam with uniform moment is multiplied by the equivalent uniform moment factor C_1 to obtain the elastic critical moment for any bending moment diagram.

Lateral bending and torsional restraints provided by beam end supports have a significant effect on the lateral torsional buckling of beams. The degrees of lateral bending and torsional restraints developed by the supports depend on the type of the connection used. Many simple connections met in practice have only partial lateral bending restraint and are generally assumed to provide full torsional restraint. However, some connections such as long fin-plate connections provide both partial lateral bending and torsional restraints. Therefore, the beams connected with fin-plates are prone to undergo some twisting about the longitudinal axis at the supports, in addition to lateral bending. EC3 ENV[*] takes into account the effect of the lateral bending restraint of the end support in the evaluation of the elastic critical moment M_{cr} by means of a coefficient k_z. However, it is assumed that full torsional restraint is provided by the connection.

For any particular end connection, the influence of the degree of lateral bending and torsional restraints can be expressed in terms of reduction of the lateral torsional bending moment M_{cr}. The scope of this work is to study the effects of lateral and torsional end restraints on the lateral torsional buckling moment of the beam. An analytical model has been developed in order to evaluate the lateral bending and the torsional restraints coefficients k_z and k_θ. The model also allows to evaluate the percentage of reduction of the lateral torsional bending moment M_{cr} against M_{0cr} for full restraint. On the basis of the value of the percentage reduction of M_{cr} for a particular connection, its classification as simple, partial restraint or full restraint can be made. Therefore, it is possible using the analytical model developed to determine the required lateral bending and torsional restraints of the connection to ensure full lateral restraint.

Theoretical expressions of the coefficients k_z and k_θ, taking into account the support minor axis bending and the torsional restraints respectively are proposed. A variety of connections with different end restraints are investigated using the finite element software LTBeam [8] in order to determine their influence on the lateral torsional buckling critical moment. It should be noted that this research work is of theoretical nature. It is done for three simple load cases. A uniform distributed load, acting on the beam in the vertical direction at the shear centre, a constant moment along the beam and a concentrated load at mid-span acting at the shear centre. A comparison between the elastic critical moments for various beam lengths and various end restraints, obtained from LTBeam, and those derived from the EC3 ENV formula in which the coefficients k_z and k_θ computed from the proposed formulae are introduced, confirms the reliability of these coefficients that model end support conditions.

---

[*] Reference is made to EC3 ENV [5] and not to EC3 EN [4] as the formulae for M_{cr} have been removed from [4] in the so-called "conversion period"

Given the type of loading, Eurocode 3 [5] provides the values of the equivalent uniform moment factor C_1 only for limited end restraints conditions for $k_z = 1$ and $k_z = 0,5$. In the cases of the lateral bending coefficients k_z being different from 1,00 and 0,5 the corresponding values of C_1 have been obtained by linear interpolation.

2.   LATERAL TORSIONAL BUCKLING AND ELASTIC CRITICAL MOMENT

Under increasing loading (see Figure 1), the beam first bends strictly in the plane of loading and w is the deflection in that plane. Once the moment reaches a certain magnitude M_{cr}, called elastic critical moment, the beam may deflect suddenly out of the plane of bending. This instability phenomenon is known as lateral torsional buckling. Lateral torsional buckling is said to occur by bifurcation of equilibrium. The beam simultaneously exhibits lateral displacements v in the y direction (bending about the minor axis of the cross-section) and twist rotation θ about its longitudinal axis x.

It is clear that lateral-torsional buckling is resisted by a combination of lateral bending resistance $EI_z d^2v / dx^2$ and torsional resistances $GI_t\, d^2\theta / dx^2$ and $EI_w\, d^3\theta / dx^3$. Thus, a member is especially prone to lateral torsional buckling when it has low lateral flexural stiffness EI_z and its torsional stiffness GI_t and warping stiffness EI_w / L^2 are low compared to its stiffness in the plane of loading. With the nomenclature used in Eurocode 3 [4], where (x-x) is the axis along the member, (y-y) is the major axis of cross-section and (z-z) is the minor axis of the cross-section, the governing differential equation for the lateral torsional buckling is [7]:

$$EI_w \frac{d^4\phi}{dx^4} - GI_t \frac{d^2\phi}{dx^2} - \frac{1}{EI_z} M_y^2 \phi + \frac{1}{EI_z} M_y M_z = 0 \tag{1}$$

with

$$\frac{dM_y}{dx} = V_z \quad ; \quad \frac{dV_z}{dx} = -q_z \quad ; \quad \frac{dM_z}{dx} = -V_y \quad ; \quad \frac{dV_y}{dx} = 0 \tag{2}$$

where q_z is the distributed load acting on the beam, V_y and V_z are the shear forces, M_y and M_z are the bending moments, and ϕ is the torsion deformation. In order to be able to impose appropriate boundary conditions at supports, the internal shear forces and the bending moment components in Eqs. (1) and (2) are referred to the axis in the undeformed configuration.

Exact solutions for Eq. 1 are obtained for a doubly symmetrical beam with simply supported conditions, free warping and subjected to a uniform moment diagram. The elastic critical moment for this basic case is:

$$M_{cr} = \frac{\pi^2 EI_z}{L^2} \sqrt{\frac{I_w}{I_z} + \frac{L^2 GI_t}{\pi^2 EI_z}} \tag{3}$$

The elastic critical moment obtained for the basic situation by formula (3), is multiplied by the equivalent uniform moment factor C_1 which takes into account the actual bending moment diagram. Thus, the value of M_{cr} may be computed by the expression:

$$M_{cr} = C_1 \frac{\pi^2 EI_z}{(k_z L)^2} \sqrt{(\frac{k_z}{k_w})^2 \frac{I_w}{I_z} + \frac{(k_z L)^2 GI_t}{\pi^2 EI_z}} \qquad\qquad (4)$$

where the lateral bending coefficient k_z and the warping coefficient k_w are introduced in order to take into account support conditions other than simply supported. These coefficients are equal to 1,00 for free lateral bending and free warping and 0,5 for prevented lateral bending and warping.

2.1   Eurocode 3 (ENV) Approach and Its Limitations

The assessment of the stability behaviour of steel beams based on simplified calculations, as described in the standards of most countries, is not always a realistic evaluation. The assumption that member end connections behave as either pinned or completely rigid is a highly simplified approach because experimental investigations show that true joint behaviour has characteristics between these two simplified extremes. In order to simplify the calculation of structural elements, beams or girders and columns are treated in isolation in most steel design codes, and the effect of the connections is estimated using simple factors which take account of the warping and bending restraint conditions.

The design proposals for the buckling of beams assume that the end supports should completely prevent end twisting. If the supports have only limited elastic torsional restraint stiffness, the beam will buckle at a lower load than that estimated from the idealised case (Figure 1).
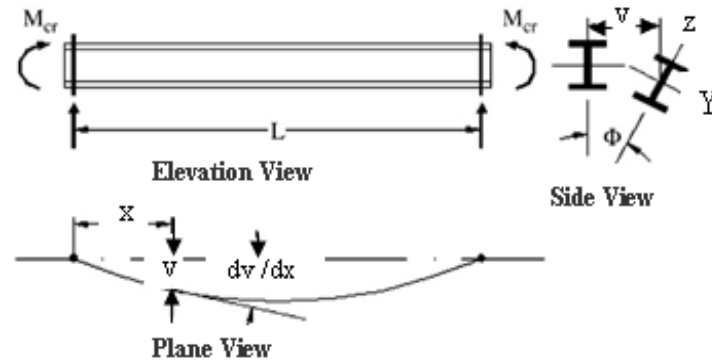

Figure 1.   Buckling of a Simply Supported I-beam

One of the most commonly employed general formulae to estimate elastic critical moment M_{cr} is the so-called 3-factor formula, which was included in the ENV version of EC3 [5]. The recently completed EN version of this design standard [4] provides no information concerning the determination of M_{cr}. In theory, this formula should be applicable to beams subjected to major axis bending having doubly or singly symmetrical cross-sections and arbitrary support and loading conditions. However, some particular cases are currently not covered, most notably the case of beams with partial end restraint against minor axis bending, and partial end restraint against twisting, which are in practice partially free to deflect laterally and twist   at the supports.

The moment gradient along the beam is considered by the use of the coefficient C_1 which is also affected by the lateral bending conditions at end supports. Eq. 4 gives the elastic critical moment as a function of C_1, k_z and k_w. It can be seen from the M_{cr} expression Eq. 4, that the effect of the end twisting at the supports of the beam which is supposed to be introduced by a coefficient k_θ has not been taken into account. This means that the beam is assumed to be completely prevented

from twisting about the longitudinal axis at the end supports. However, many real situations met in practice are not in compliance with these standard conditions. For these practical situations (such as those with simple connections with long fin-plates which possess partial torsional restraint), the beam is prone to undergo some twisting about the longitudinal axis at the end supports causing a deduction in elastic critical moment M_{cr}. Therefore the effect of the partial end torsional restraint should be considered by introducing a coefficient k_θ in the expression of M_{cr}.

This paper attempts to fill in two of the insufficiencies identified in the above expression of M_{cr} used by the Eurocode 3, by (i) proposing a formula for computing the value of the lateral bending restraint coefficient k_z which depends on both the connection end restraint and the beam flexural stiffness about the minor axis and (ii) proposing a formula for computing the value of the torsional restraint coefficient k_θ of the end support (Figure 2) which depends on both the torsional stiffness of the support K_Θ and of the torsional rigidity of the beam GI_t/L.

In the EC3 ENV [5], it is suggested to take k_w=1,00 unless special provision for warping fixity is made. Therefore, in this paper, the warping coefficient k_w is set to be equal to 1,00.
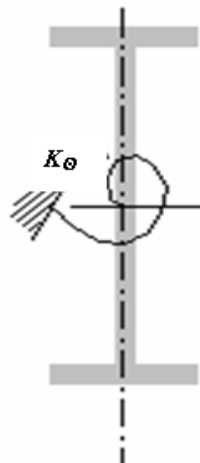

Figure 2. Torsional End Restraint

2.2   Theoretical Background on Torsional Restraints at Supports

Flint [9] presented an analysis for a member with end connections providing only limited torsional stiffness. For a beam under single point load or two symmetrical point loads, Flint derived the following relationship between the critical load and the support torsional restraint stiffness.

$$m = 1 - \frac{4}{3} R_T \tag{5}$$

In Eq. 5 m is the ratio between buckling loads for beams with finite and infinite support torsional stiffness. R_T is the ratio of the torsional stiffness of the beam to its supports and is given by $\dfrac{GJ/L}{T/\theta}$ where θ is the rotation of a support.

A theoretical study was carried out by Schmidt [10] to determine the effect of elastic end torsional restraint on the critical load of a beam. It shows that the beam is incapable of supporting any load if the end supports offer no resistance to end twisting. It further shows that the critical load increases

little as the end torsional restraint stiffness parameter e increases beyond 20. The parameter e is defined as $e = 1/R_T$. According to Flint's equation (5), Bose [11] found that the critical load for $e = 20$ will be 93% of the load for rigid torsional end support.

Bennetts et al [12] and Grundy et al [13] have attempted to investigate the value of the torsional stiffness K of an end restraint and in particular, the torsional stiffness K_s of the connection component. They investigated the behaviour of fin-plates and noted that the torsional stiffness varied almost continuously with the applied moment.

Bennetts et al stated that the end torsional stiffness is a function of the beam web thickness, the depth of the beam and the depth of the connection component. They felt that the interaction between these components is quite complex and attempts to produce a theoretical model for the overall behaviour would probably prove unsuccessful. They also found that the experimental results were sensitive to the method of testing and results differed in subsequent loading cycles. However, it is worth noting that the test rig used produced only a torsional moment in the fin-plate connection. This method of testing removed any possibility of beneficial restraining effects afforded by the supported beam upon the connection.

3.   PARAMETRICAL STUDY ON BEAM ELASTIC STABILITY

As seen before, the elastic critical moment M_{cr} is a function of C_1, k_z and k_w. It should be noted that the design proposals for the buckling of beams EC3 does not consider the possibility of k_z being different from 1,00 or 0,5 which represent the two extreme cases, free lateral bending and prevented lateral bending. In practice, the coefficient k_z may take any value between 1,00 and 0,5 depending on the degree of lateral restraint provided by the end supports of the beam. It should also be mentioned that EC3 ENV does not take into account the possibility of the end restraint being partially prevented from twisting about the longitudinal axis of the beam. The elastic critical moment expression considers the beam as completely prevented from twisting at the end supports. If the supports have only limited elastic torsional restraint stiffness, as it is the case of some practical connections such as fin-plates, the beam will buckle at a lower load than that estimated from the idealised case. Therefore, the aim of this work is to derive analytical expressions for the lateral bending restraint at the support k_z and the torsional end restraint k_θ to be introduced in the expression of the elastic critical moment M_{cr}.

3.1   Proposed Expressions of Lateral and Torsional Restraint Coefficients at Supports

The behaviour of beams is dependent on their end support conditions and possibly on their intermediate supports. These conditions depend not only on major axis bending (primary bending) but also on minor axis bending, uniform torsion and warping torsion. The latter three types of support conditions influence deeply the *LTB* resistance. In the existing codes, the support conditions are accounted for by means of so-called effective length factors k_z and end warping factor k_w. Each of these two factors varies from 0,5 for full fixity to 1,00 for no fixity at all, and takes the value of about 0,7 for one end fixed and one end free. In the EC3 ENV [5], it is suggested to take $k_w = 1,0$ unless special provision for warping fixity is made. The values of the C_1 factor involved in the analytical expression of the elastic critical *LTB* moment is significantly influenced by the k_z values; however, in EC3 ENV, only 2 or 3 values of k_z are suggested. In order to be

able to evaluate satisfactorily the values of k_z, it is probably acceptable to calculate the C_1 factor by means of linear interpolation.

Different expressions for computing lateral bending restraint coefficient k_z and torsional restraint k_θ of the end support have been considered, and the following ones Eq. 6 and Eq. 7 are finally selected, even though further research might provide a more exact formulation.

$$k_z = \frac{EI_z / L + 0,25K_{v'}}{EI_z / L + 0,5K_{v'}} \tag{6}$$

$$k_\theta = \sqrt{1 + 5\frac{GI_t / L}{K_\Theta}} \tag{7}$$

where: I_z is the minor axis moment of inertia of the beam, E is the modulus of elasticity, L is the unbraced length, $K_{v'}$ is the lateral flexural restraint of the support, G is the shear modulus, I_t is the torsional constant and K_Θ is the torsional restraint of the support .

It can be seen from Eq. 6 that for $K_{v'}$ varying from zero to infinity, the value of k_z ranges from 1,00 (no fixity) to 0,5 (full fixity). Eq. 7 shows that if no torsional restraint is provided by the support ($K_\Theta = 0$), then the torsional restraint coefficient k_θ is infinity, and for full torsional restraint of the support (K_Θ =infinity), the torsional restraint coefficient k_θ is 1,00.

For doubly symmetrical cross-section and for end moment loading or transverse loads applied at the shear centre, the elastic critical moment to be considered as the critical value of the maximum moment in the beam may be assessed by the new proposed formula:

$$M_{cr} = C_1 \frac{\pi^2 EI_z}{(k_\theta k_z L)^2} \sqrt{(\frac{k_\theta k_z}{k_w})^2 \frac{I_w}{I_z} + \frac{(k_\theta k_z L)^2 GI_t}{\pi^2 EI_z}} \tag{8}$$

where k_z is the lateral bending restraint coefficient, ranging from 0,5 (for full fixity) to 1,00 (for free lateral bending at the support), which can be evaluated from Eq. 6, k_θ is the torsional restraint coefficient which varies from 1,00 (for support prevented from twisting about longitudinal axis) to infinity (for free twisting of the support about longitudinal axis).
Eq. 8 may be written in its simplified form as:

$$M_{cr} = C_1 \frac{\pi^2 EI_z}{k_\theta (k_z L)^2} \sqrt{(\frac{k_z}{k_w})^2 \frac{I_w}{I_z} + \frac{(k_z L)^2 GI_t}{\pi^2 EI_z}} \tag{9}$$

It can be seen that Eq. 9 is the same as the one given by EC3 ENV [5], only for a beam fully prevented from twist rotation at the supports ($k_\theta = 1$). It can also be seen from Eq. 9 that for a support connection providing no torsional restraint (k_θ = infinity), the elastic critical moment M_{cr} tends towards zero and therefore the beam will be in the state of instability.

Finally Eq. 9 can be expressed as:

$$M_{cr} = \frac{1}{k_\theta} M_{0cr}$$

(10)

It can be seen from Eq. 10, that the critical moment M_{cr} can be obtained by multiplying the critical moment M_{0cr} obtained for a beam with full torsional restraint at supports ($k_\theta = 1$) by $\frac{1}{k_\theta}$.

4.   ANALYTICAL EVALUATION OF THE ELASTIC STABILITY

4.1   Influence of Lateral Bending Restraint

In this section the variation of the lateral bending restraint coefficient k_z is examined for various sizes of IPE profiles (IPE300, IPE360, IPE400 and IPE500) of varying lengths (L=4m, 6m, 10m, and 12m), subjected to three load cases, equal end moments, uniformly distributed vertical loads applied to the shear centre and a concentrated vertical load at mid-span applied to the shear centre.

In order to perform a comparative study, numerical analysis was conducted using the LTBEAM software which was developed by CTICM [8] within the framework of a European project and based on the finite element method. In this analysis the end supports of the beam are assumed to be fixed for out of plane deflection, $v = 0$ and twist rotation, $\theta = 0$ ($k_\theta = 1$), but not restrained against warping, ($k_w = 1$). The lateral flexural restraint of the support is modelled by a spring of lateral restraint value $K_{v'}$. It is taken as zero (for no lateral restraint) or infinity (for full lateral restraint). To evaluate M_{cr} using the FEM, it is necessary to determine the value of the lateral bending restraint of the connection $K_{v'}$. Therefore, for any lateral bending restraint coefficient k_z, the corresponding value of $K_{v'}$ can be evaluated using Eq. 6.

Figure 3 shows the numerical and analytical results of the variation of elastic critical moment against variation of lateral bending restraint coefficient k_z for equal end moments. It can be seen from Figure 3 that the results obtained from EC3 ENV formula for k_z varying from 0,5 to 1,00 are in very good agreement with those computed from FEM, except for the case of full lateral restraint. For k_z =0,5, the values of M_{cr} obtained from EC3 ENV formula are lower than those derived from FEM.

The reason is that the EC3 ENV formula assumes that coefficient C_1 does not vary with end support conditions for equal end moments. However, using finite differences approach, Miguel A. Serna [7] shows that for the case of equal end moments, the values of C_1 for beams with prevented lateral bending at supports (k_z =0.5) are higher than those for simply supported beams, which confirms the difference found in this study between the numerical and analytical results of M_{cr} for the case of restrained end supports against lateral bending (k_z =0,5). Following the difference between the FEM results and those obtained analytically by EC3 ENV formula, for k_z =0,5 it is recommended that the value of C_1 be taken as 1,05 which is the value suggested in [14].
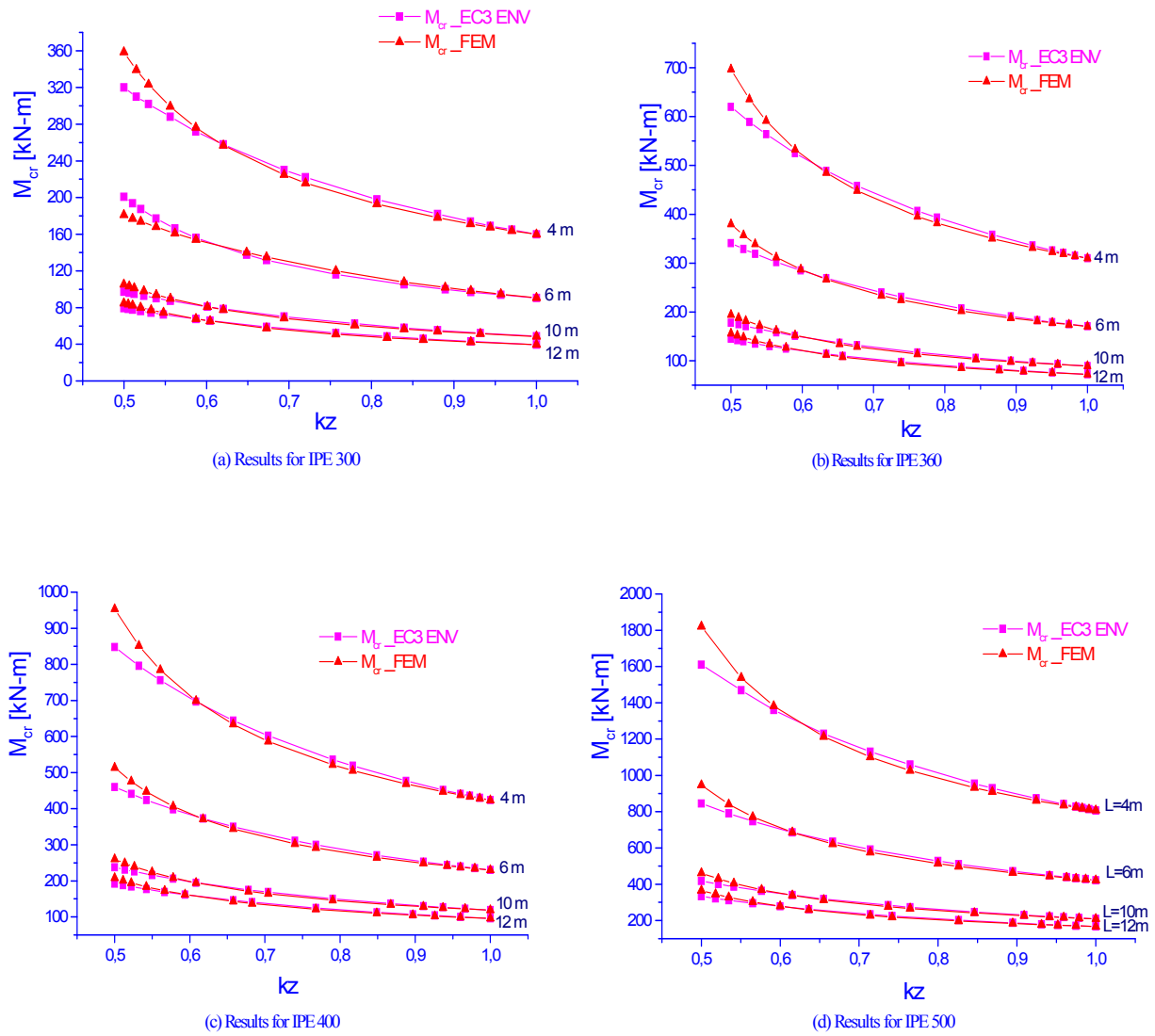
Figure 3. Numerical and Analytical Elastic Critical Moments Versus
Lateral Bending Coefficient k_z for Equal End Moments

For the case of uniformly distributed vertical loads, the numerical and analytical results of the variation of elastic critical moment M_{cr} as a function of lateral bending restraint coefficient k_z are given in Figure 4.
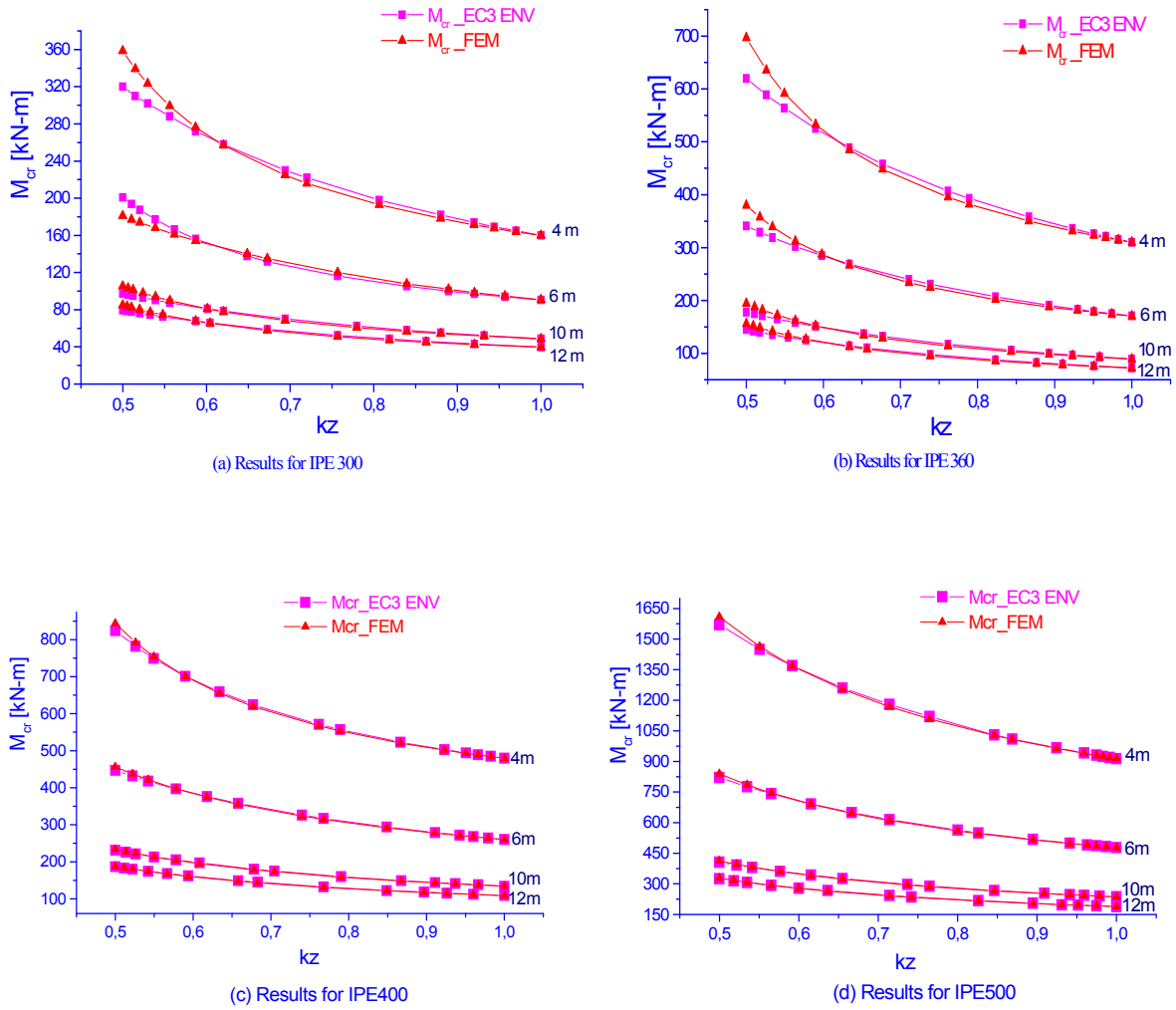
Figure 4. Numerical and Analytical Elastic Critical Moments Versus
Lateral Bending Coefficient k_z for Uniformly Distributed Loads

It can be seen that for all IPE profiles and beam lengths considered in this study, there is quite good agreement between the values given by the EC3 ENV formula and the numerical results obtained using the finite elements approach.

Finally, Figure 5 shows the results of the variation of elastic critical moment M_{cr} against lateral bending restraint coefficient k_z for the case of concentrated load acting at the mid span. As can be seen from Figure 5, the graphs of the elastic critical moments M_{cr} obtained analytically for various IPE profiles and lengths are very close to those computed numerically by the finite element method. Therefore the proposed new formula (6) provides very good approximation of k_z for all cases considered in this study.
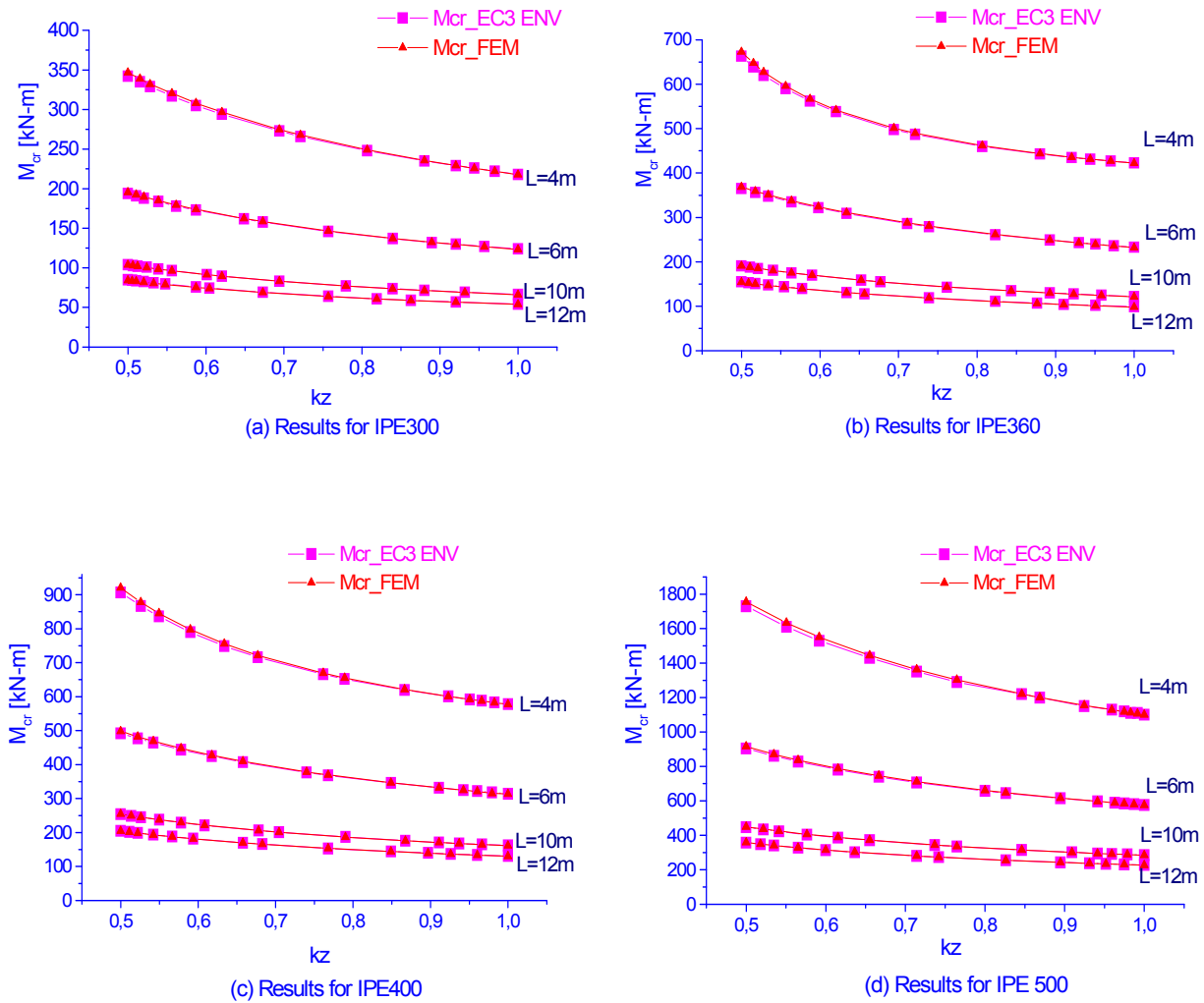
Figure 5. Numerical and Analytical Elastic Critical Moments Versus Lateral
Bending Coefficient k_z for a Concentrated Load at the Mid Span

4.2 Influence of End Torsional Restraint

In this study, the effect of the variation of support torsional restraint k_θ on the elastic critical moment M_{cr} is investigated numerically using finite element approach and analytically with the application of the EC3 ENV formulation. As mentioned previously, the elastic critical moment M_{cr} for a beam determined according to EC3 ENV formula, assumes that the end supports of the beam are fully prevented from twisting, thus full torsional restraint is provided. However, some types of supports met in practice such as fin-plates, provide only partial torsional restraint. Therefore it is recommended that the effect of torsional restraint provided by end supports of the beam should be taken into account in the EC3 ENV formula by means of a coefficient k_θ. The values of k_θ may be obtained using the proposed formula (7).

The lateral-torsional buckling of four IPE profiles (IPE 300, IPE 360, IPE 400 and IPE 500) with three different lengths (L=6m, L=10m and L=12m) have been studied for two load cases, uniformly distributed vertical loads applied to the shear centre and a concentrated vertical load at mid-span

applied to the shear centre. In this analysis the end supports of the beam are assumed to be fixed for out of plane deflection ($v = 0$) and for lateral bending rotation ($k_z = 1$) but not restrained against warping ($k_w = 1$). The torsional restraint of the support is modelled by a spring of torsional restraint value K_Θ. If no torsional restraint is provided by the support ($K_\Theta = 0$) then $\dfrac{1}{k_\theta} = 0$ and for full torsional restraint of the support ($K_\Theta =$ infinity) then $\dfrac{1}{k_\theta} = 1$. For partial torsional restraints of the end supports, which correspond to the values of $\dfrac{1}{k_\theta}$ varying from 0 to 1,00, the corresponding values of the spring torsional restraints K_Θ can be calculated from Eq. 7.

Figure 6 shows the numerical and analytical results of the variation of M_{cr}/M_{0cr} against variation of $\dfrac{1}{k_\theta}$ for the case of uniformly distributed vertical loads. According to Eq. 10, the graphs of M_{cr}/M_{0cr} versus $\dfrac{1}{k_\theta}$ for all IPE cross-sections and lengths obtained from the analytical expression through the application of the new proposed formula are represented by a single straight line. It can be seen from Figure 6 that the numerical results of M_{cr}/M_{0cr} against $\dfrac{1}{k_\theta}$ obtained through LTBEAM software in which the values of the spring torsional restraints K_Θ are computed from the proposed analytical formula (7), are represented by curved lines.

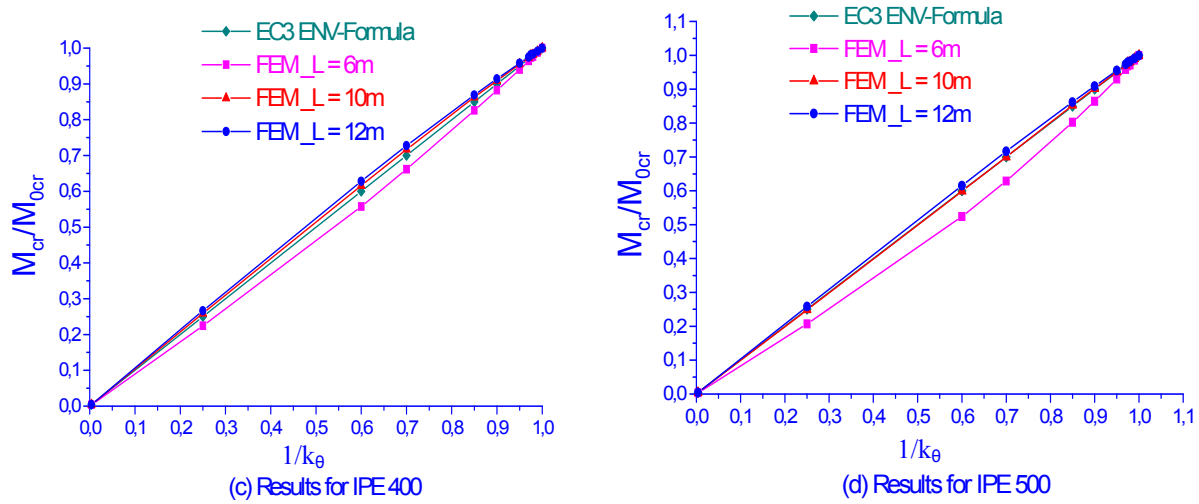(a) Results for IPE 300   (b) Results for IPE 360
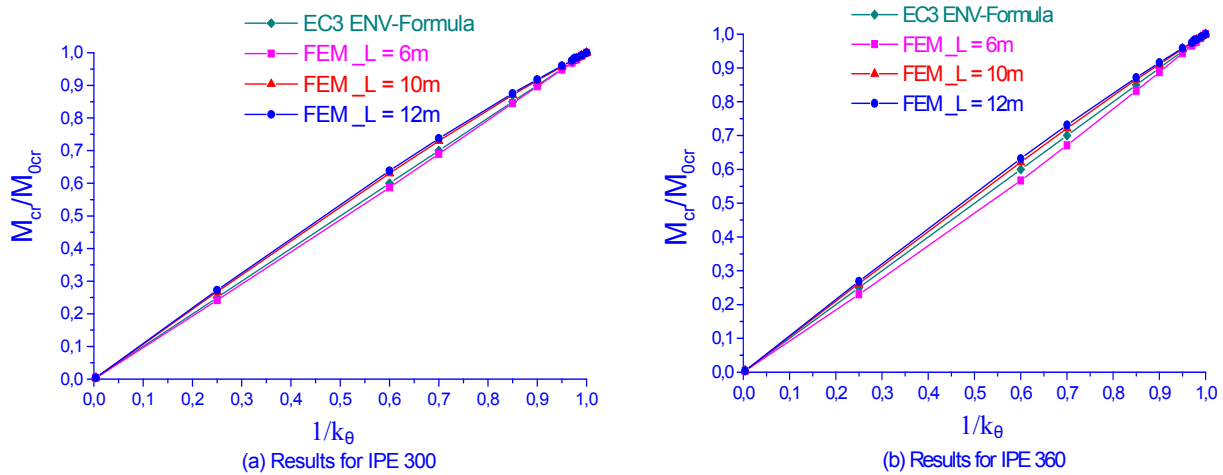
Figure 6. Results from FEM and Eq. 10 for uniformly distributed loads

Figure 7 shows the numerical and analytical results of the variation of M_{cr}/M_{0cr} against variation of $\dfrac{1}{k_\theta}$ for the case of a concentrated vertical load at the mid-span acting at the shear centre. Again it also shows that the numerical results of M_{cr}/M_{0cr} against $\dfrac{1}{k_\theta}$ obtained through LTBEAM software in which the values of the spring torsional restraints k_Θ are computed from the proposed analytical formula (7) are represented by curved lines.
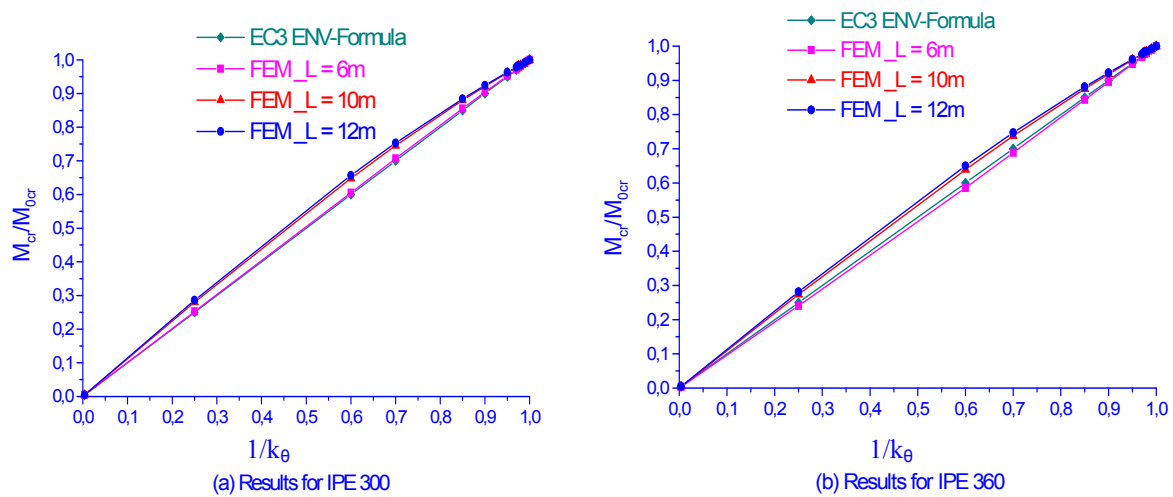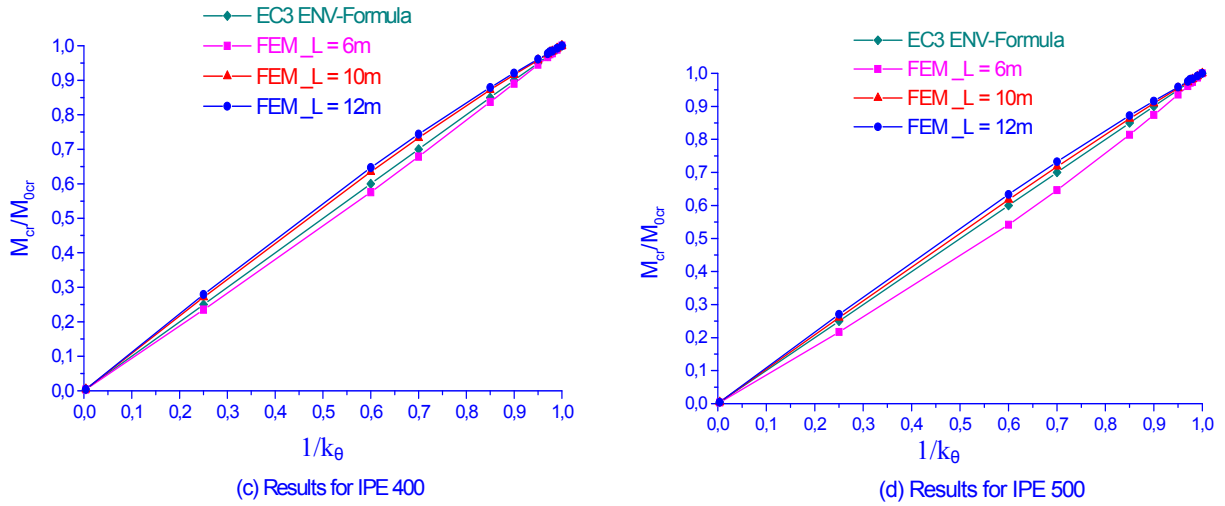
Figure 7. Results from FEM and Eq. 10 for a Concentrated Load at Mid-span

It is worth noting from Figure 6 and Figure 7 that, the closer the M_{cr}/M_{0cr} graphs to the straight line, the more accurate the formula (7). Therefore it can be seen from the figures that, for both load cases and for all IPE cross-sections and lengths considered in this study, the graphs of M_{cr}/M_{0cr} obtained from FEM analysis are particularly close to the ones obtained from the proposed analytical expression Eq. 10, in which the torsional restraint coefficient k_θ has been introduced. In other words, comparison of the cases performed in this analysis revealed that an acceptable small difference exists between analytical and numerical results (errors are within about 10%). Therefore, there is quite good agreement between the results given by the proposed analytical formula and the numerical results of the FEM approaches.

5.   REQUIRED CONNECTION TO ENSURE SUFFICIENT RESTRAINT LEVEL

Depending on the degree of lateral bending and torsional restraints developed, a connection can be classified as simple, partial or full restraint connection. Using the analytical model developed in section 3.1, it is now possible to evaluate the lateral bending and torsional restraints for any beam end connection, therefore its classification can be made.

If a lateral bending restraint of a connection results in a reduction of less than 10% of M_{cr} from M_{0cr} for full restraint, then it can be assumed as full lateral bending restraint connection. However, if it results in more than 10% drop of M_{cr} from M_{0cr}, then it is considered as partial bending restraint connection. Similarly, if a connection torsional restraint results in less than 10% drop of M_{cr} from M_{0cr}, then full torsional restraint connection can be assumed, otherwise, it is considered as partial tortional restraint connection.

The interaction between the effects of k_z and k_θ on the elastic critical moment has not been included in this study. Therefore, in order to classify a connection, it is clear that the effects of lateral bending and torsional restraints have been considered independently in the analysis. Thus, when varying the values of k_z, the torsional restraint has been considered as full torsional restraint (k_θ=1). When varying the values of k_θ, the lateral bending restraint has been considered as simple restraint (k_z=1).

Finite elements analyses have been performed to verify the accuracy of Eqs. 6 and 7. For beams with IPE profiles subjected to equal end moments, uniformly distributed loads or, a concentrated point load at the mid span acting at the shear centre, the results show that Eq. 6 can be reasonably applied to evaluate the lateral bending restraint coefficient k_z.

The analyses also show that for beams with IPE profiles subjected to uniformly distributed loads or, a concentrated point load at the mid span acting at the shear centre and for $k_z=1$, Eq. 7 can be satisfactory applied to simulate the effect of the torsional restraint of the end support k_θ.

It can be seen from Figure 3, that for the case of beams subjected to equal end moments, 10% drop in the value of the elastic critical moment M_{cr} against M_{0cr} for full restraint, is obtained for a value of $k_z=0,53$. For the case of uniformly distributed loads, Figure 4, shows that 10% reduction in the value of M_{cr} from M_{0cr} for full restraint, corresponds to $k_z=0,56$. Figure 5 shows that for a beam subjected to a concentrated point load at the mid-span and for $k_z=0,577$, the corresponding value of the elastic critical moment M_{cr} is reduced by 10% compared to M_{0cr} for full restraint. It can also be seen that, for the same percentage reduction in M_{cr}, the corresponding values of k_z are strongly dependent on the loading type.

According to the results obtained from the proposed expressions of k_z and k_θ given in section 3.1, it is recommended that if the percentage drop in the value of the elastic critical moment M_{cr} against M_{cr} for full restraint remains within 10%, then full restraint may be assumed. Therefore, for lateral bending restraint coefficients k_z ranging from 0,5 to 0,53 (for equal end moments), from 0,5 to 0,56 (for uniformly distributed loads) and from 0,5 to 0,577 (for a concentrated point load at mid-span), the end lateral bending restraint may be assumed as full lateral bending restraint ($k_z=0,5$). For each load case, the minimum lateral flexural stiffness value of the end support $k_{v'}$ required to assume full lateral restraint of the support, can be obtained from Eq. 6.

Figure 6 and Figure 7 show the values of $\dfrac{1}{k_\theta}$ for percentage drops in the value of the elastic critical moment M_{cr}, against M_{0cr} for full torsional restraint. When examining Figure 6. and Figure 7, it can be revealed from analytical and FEM results that for $\dfrac{1}{k_\theta}=0,9$, the corresponding value of M_{cr}/M_{0cr} is 0,9. Therefore, for all IPE cross-sections, beam lengths and load cases performed in this analysis, 10% reduction in the value of $\dfrac{1}{k_\theta}$, results in 10% drop in the value of M_{cr} against M_{0cr} for full torsional restraint.

According to results in section 3.1, for IPE cross-sections under uniformly distributed loads or a concentrated point load at mid span acting at the shear centre, Eq. 7 provides values of end torsional restraint coefficients k_θ that are in very good agreement with the FEM results.

It can be seen from Figure 6, Figure 7 and Eq. 7 that for 10% drop in the value of the elastic critical moment M_{cr} against M_{0cr} for full torsional restraint, it results in a value of $\frac{1}{k_\theta}$ =0,9, which corresponds to a value of the torsional stiffness of the support K_Θ =21,3 GI_t / L . Thus, for $\frac{K_\Theta}{GI_t / L}$ =21,3 (ratio of the torsional stiffness of the supports to its beam), the value of the elastic critical moment is $M_{cr} = 0,9 M_{0cr}$.

From these results, it is recommended to assume that the torsional stiffness of the connection is acceptable and may be considered as full torsional restraint, if it results in no more than 10% drop in the value of M_{cr} for full restraint. Therefore, if it is proved that the ratio of the torsional stiffness of a connection K_Θ to its beam GI_t / L is at least equal to 21,3, then it is recommended to assume full restraint connection, as M_{cr} will be 90% of M_{0cr} for rigid torsional end support.

6. CONCLUSIONS

When dealing with lateral torsional buckling, modern design standards require the computation of the elastic critical moment, which mainly depends on the moment distribution along the beam and on the end supports restraints. One of the most commonly used general formulae to estimate elastic critical moments in steel beams prone to LTB is the so-called 3-factor formula, which is included in the ENV version of Eurocode 3 [5].

This paper presents a review of EC3 ENV approach and its limitations with regards to lateral bending and torsional restraints of the end supports. Based on these limitations, the paper has presented new expressions for estimating the actual degree of lateral bending restraint k_z and torsional restraint k_θ of the end supports. The values of the coefficients k_z and k_θ obtained from the proposed expressions, are introduced in the general formulae that estimates the elastic critical moment. The influence of the lateral bending and torsional restraint on the lateral-torsional buckling of IPE beams with various cross-sections, different loading conditions and lengths has been investigated using analytical and FEM approach. Comparison between these two approaches allows to show the accuracy of the proposed k_z and k_θ expressions.

For beams subjected to uniformly distributed loads or a concentrated load at mid-span applied at the shear centre, the results of the variation of M_{cr} against k_z , obtained from EC3 (ENV) formula for k_z varying from 0,5 to 1,0 are in very good agreement with those computed from FEM. The results of variation of M_{cr} / M_{0cr} versus $\frac{1}{k_\theta}$ computed from FEM are quite close to those obtained from EC3 (ENV) formula. Finally the following can be concluded from this study:

(i)   Eq. 6 and Eq. 7 can be reasonably applied to evaluate lateral bending and torsional restraints of end supports.
(ii)   For beams subjected to equal end moments with k_z =0,5, it is recommended that the value of coefficient C_1 be taken as 1,05, instead of 1,00.

(iii)   Full lateral and torsional restraint of end supports may be assumed if it results in less than a 10% drop in the value of elastic critical moment M_{cr} against full torsional restraint moment M_{0cr}.

(iv)   Full lateral bending restraint at supports may be assumed for beams subjected to equal end moments, if $k_z \leq 0,53$, for uniformly distributed loads if $k_z \leq 0,56$ and for a concentrated point load at mid span if $k_z \leq 0,577$.

(v)   To assume full torsional restraint of end supports, it is necessary that the ratio between the torsional stiffness of the supports and of the beam $\dfrac{K_\Theta}{GI_t / L}$ be at least 21,3.

ACKNOWLEDGMENT

REFERENCES

[1]   AISC LRFD 1986. American Institute of Steel Construction (AISC). Load and resistance factor design. Chicago: AISC; 1986.

[2]   AISC LRFD 1994. American Institute of Steel Construction (AISC). Load and resistance factor design. Chicago: AISC; 1994.

[3]   BS 5950-1. Structural use of steelwork in buildings. Code of practice for design. Rolled and welded sections. British Standards Institution; 2000.

[4]   EC3 2005. European Committee for Standardization. Eurocode 3: Design of steel structures, Part 1-1: General rules and rules for buildings (EN 1993-1-1). Brussels; May 2005.

[5]   EC3 1992. European Committee for Standardization. Eurocode 3: Design of steel structures, Part 1-1: General rules and rules for buildings. (ENV 1993-1-1). Brussels; 1992.

[6]   Trahair, N.S., "Multiple Design Curves for Beam Lateral Buckling", Stability and Ductility of Steel Structures, T. Usami and Y. Itoh (Eds.), Pergamon, 1998.

[7]   Serna, M.A., Lopez, A., Puente, I. and Yong, D.J., "Equivalent Uniform Moment Factors for Lateral-torsional Buckling of Steel Members", Journal of Constructional Steel Research, Vol. 62, pp. 566-580, 2006.

[8]   Galéa, Y., "Moment Critique de Déversement élastique de Poutres Fléchies", Presentation du logiciel LTBEAM. Revue de la Construction Métallique. Vol. 2, CTICM 2003.

[9]   Flint, A.R., "The Influence of Restraints on the Stability of Beams", The Structural Engineer, Vol. 29, pp. 235-246, September 1951.

[10]   Schmidt, L.C., "Restraints Against Elastic Lateral Buckling", J. of Eng. Mech. Div., ASCE, Vol. 91, No. EM6, pp. 1-10, December 1965.

[11]   Bose, B., 'The Influence of Torsional Restraint Stiffness at Supports on the Buckling Strength of Beams", The Structural Engineer, pp. 69-74, December 1982.

[12]   Bennetts, I.D., Thomas, I.R. and Grundy, P., "Torsional Stiffness of Shear Connections", Preprints, Metal Structures Conference, Institution of Engineers, pp.-102, Australia, 1981.

[13]   Grundy, P., Murray, A.W. and Bennetts, I.D., "Torsional Rigidity of Standard Beam-to-Column Connections", Preprints, Metal Structures Conference, Institution of Engineers, Australia, pp.-164, 1983.

[14]   ECCS Technical Committee 8- Stability, 2006. European Convention for Constructional Steelwork, Rules for Member Stability in EN 1993-1-1. Background documentation and design guidelines, No. 119, 2006.